This is to certify that the
dissertation entitled

EFFECT OF FINITE CAVITY WIDTH ON THE SELF-SUSTAINED OSCILLATION IN A LOW-MACH-NUMBER CAVITY FLOW

presented by

Ke Zhang

has been accepted towards fulfillment
of the requirements for the

Ph.D. degree in Mechanical Engineering

Major Professor's Signature

10/21/09

Date

EFFECT OF FINITE CAVITY WIDTH ON THE SELF-SUSTAINED OSCILLATION IN A LOW-MACH-NUMBER CAVITY FLOW

By

Ke Zhang

A DISSERTATION

Submitted to
Michigan State University
in partial fulfillment of the requirements
for the degree of

DOCTOR OF PHILOSOPHY

MECHANICAL ENGINEERING

2009

ABSTRACT

EFFECT OF FINITE CAVITY WIDTH ON THE SELF-SUSTAINED OSCILLATION IN A LOW-MACH-NUMBER CAVITY FLOW

By

Ke Zhang

Cavity flow is known to be associated with high-level-noise generation, strong vibration and substantial increase in the drag force on the object containing the cavity. Most of the studies of the cavity flow are based on a two-dimensionality assumption. The three-dimensional features of cavity unsteadiness/oscillation are rarely investigated. The current study is focused on examining the effect of the cavity width and side walls on the self-sustained oscillation in a low-Mach-number cavity flow with a turbulent boundary layer at separation.

An axisymmetric cavity geometry is employed in the present research. The axisymmetric configuration provides a distinct advantage in studying the side-wall effects in that the configuration provides a reference condition that is free from any side-wall influence; yet, the cavity could be partially filled to form a finite-width geometry. Unsteady surface pressure, on the cavity floor along the streamwise direction and on the downstream wall along the azimuthal direction, is acquired using microphone arrays. The pressure data are recorded over a range of flow and geometrical parameters. In particular, the Reynolds number based on cavity depth and free-stream velocity is changed from Re = 4067 to 12200, and cavity length-to-depth ratio L/D from 2.6 to 4.1 for both the axisymmetric geometry and finite-width cavities with width-to-depth ratio W/D in the range 2.5 to 7.4. Based on the outcome of the analysis of the unsteady surface-pressure

field, velocity measurements using a two-component Laser Doppler Anemometer (LDA) system are performed simultaneously with array measurements in different azimuthal planes for a cavity with $L/D = 3.3$ and $W/D = 7.4$ at $Re = 12200$ to explore the effect of the side wall on the mechanism driving the cavity oscillation. Evolution of coherent structures generating the pressure oscillation on the downstream wall of the cavity is evaluated using linear stochastic estimation (LSE) of the velocity field based on the wall-pressure signature.

The results show that while no prominent oscillation is found in axisymmetric cavities without side walls, strong harmonic pressure oscillation different from any of the known modes in the literature is observed in finite-width cavities at an azimuthal location of about one cavity depth away from the side wall. Analysis of the mean three-dimensional flow inside the cavity and the stochastic estimation results lead to the hypothesis that the flow structures in the symmetry plane of the finite-width cavities, although have a weak pressure signature, they interact with the flow near the side wall, providing the driving mechanism for the establishment of the oscillation near the side wall.

DEDICATION

To my parents and husband
for their love, support and encouragement

ACKNOWLEDGEMENTS

I would like to express my heartfelt gratitude to my advisor, Dr. Ahmed Naguib for giving me the opportunity to work on this project and for his guidance and mentorship during my four-years study at MSU. He is always there with patience.

I would also like to thank my committee members Dr. Changyi Wang, Dr. Mei Zhuang and Dr. Manoochehr Koochesfahani for their helpful comments and discussion throughout my Ph.D. study.

I really appreciate all the help from my colleagues and friends at MSU. I would like to thank Barry and Tony for their help in getting me oriented around the Flow Physics and Control Laboratory FPaCL at the beginning of my research work. I appreciate all the help from Alan, Doug, Jason, Shahram, Rohit, Vibhav and Elliot throughout my study at MSU. Special appreciations are given to Michael Mclean and Roy Bailiff for their help with the experimental setups. Thanks for your friendship, Jing.

Finally, none of this would have been possible without the love and support from my husband Min Tang. I could not imagine going through these years in the US without his love and encouragement.

This study was supported by the National Science Foundation under grant number CTS-0425374, monitored by Dr. William Schultz. Any opinions, findings and conclusions or recommendations expressed in this material are those of the authors and do not necessarily reflect the views of the National Science Foundation.

TABLE OF CONTENTS

LIST OF TABLES

LIST OF FIGURES

(Images in this dissertation are presented in color)

NOMENCLATURE

Symbol	Definition
C_p	mean-pressure coefficient $= (p_s\text{-}p_r)/ (1/2\rho U_\infty{}^2)$
$C_{p_1'p_2'}$	coherence between fluctuating pressures p_1' and p_2'
D	cavity depth
d_x	LDA measurement volume size in the streamwise direction
d_y	LDA measurement volume size in the wall-normal direction
d_z	LDA measurement volume size in the spanwise direction
E	corrected output voltage of the hot wire
E_r	raw output voltage of the hot wire
f	frequency in Hz
f_b	frequency of the incident laser beam
f_D	Doppler frequency
f_r	frequency of the scattered laser light
H	shape factor of the boundary layer $= \delta^*/\theta$
L	cavity length
M	Mach number
m	an integer Rossiter mode number
p'	surface pressure fluctuation

p'_{rms}	root mean square value of p'
p_r	reference pressure taken as the static pressure in the free stream
p_s	mean pressure on the surface of the model
q	velocity magnitude in x-y plane $= \sqrt{u^2 + v^2}$
Re	Reynolds number based on cavity depth = $U_\infty D/\nu$
$R_{u'p'}$	normalized cross-correlation between the streamwise velocity and pressure fluctuation
$R_{v'p'}$	normalized cross-correlation between the wall-normal velocity and pressure fluctuation
$r_{u'p'}$	cross-correlation between the streamwise velocity and pressure fluctuation
$r_{v'p'}$	cross-correlation between the wall-normal velocity and pressure fluctuation
r	coordinate along the radius of the model
Δr	LDA measurement grid spacing in the radial direction
T_w	hot-wire temperature
T_{cal}	flow temperature when the hot-wire calibration is performed
T_r	flow temperature during hot-wire data acquisition
t_i	transit time of particle crossing the LDA measuring volume
Δt	time offset
U^+	mean velocity normalized by wall units = U/u_τ

U_∞	free-stream velocity
u	streamwise velocity
$\overline{u}$	mean streamwise velocity
$\overline{u}_\phi$	mean velocity along the azimuthal direction
$\overline{u}_r$	mean velocity along the radial direction
$\overline{u}_x$	mean velocity along the streamwise direction
$\widetilde{u}'$	estimated velocity fluctuation
u'_{rms}	rms of the streamwise velocity
u_τ	friction velocity = $(\tau_w/\rho)^{1/2}$
$\overline{u'v'}$	Reynolds shear stress
v	wall-normal velocity
$\overline{v}$	mean wall-normal velocity
v'_{rms}	rms of the wall-normal velocity
$\overline{v}_p$	seed particle velocity vector
W	cavity width
x	streamwise coordinate
Δx	grid spacing in the streamwise direction
y	wall-normal coordinate

Δy	grid spacing in the wall-normal direction
y^+	wall-normal coordinate normalized by wall units = yu_τ/v
z	spanwise coordinate
α	angle between the two incident LDA beams
δ^*	boundary layer displacement thickness
$\phi_{p'p'}$	frequency spectrum of p'
ϕ	azimuthal angle relative to the top of the model
ϕ_c	azimuthal location of the cavity's symmetry plane relative to the top of the model
$\Delta\phi$	azimuthal location relative to the symmetry plane of the cavity = $\phi - \phi_c$
$\delta\phi$	LDA measurement grid spacing in the azimuthal location
λ_a	wavelength of one-dimenaional acoustic planar waves propagating in the plane wave tube
λ_b	wavelength of the incident laser beam
υ	kinematic viscosity of air
$\vec{\omega}$	vorticity vector
ω_z	out-of-plane vorticity in an x-y plane
$\tilde{\omega}'_z$	estimated out-of-plane vorticity in an x-y plane
ρ	density of air

τ_w	mean wall shear stress of the separating boundary layer
θ	momentum thickness of the separating boundary layer
θ_{eff}	effective momentum thickness of the separating boundary layer

1. INTRODUCTION

1.1 Background

A cavity in a surface above which fluid flows (see Figure 1.1 for definition of geometry and coordinate system) can cause large-amplitude unsteadiness in the flow field that can result in the generation of high-level noise, strong vibration and, in the extreme case, fatigue of the underlying surface. Moreover, the flow can also be associated with substantial increase in the drag force on the object containing the cavity. Cavity flow has drawn the attention of many researchers because of its significance to various engineering applications. Examples include open automobile windows and sunroofs, dump combustors, and airplane wheel wells. The importance of cavity flows is also reflected in the number of recent studies aimed at attenuation of the flow unsteadiness through various control methods. Recent reviews of these efforts may be found in Cattafesta *et al.*[1] and Rowley and Williams[2]. However, in order to properly implement/optimize the control techniques, understanding of the mechanisms responsible for the cavity oscillations is necessary.

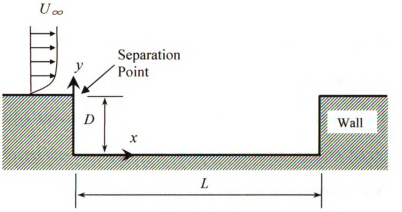

Figure 1.1 Illustration of the cavity geometry and coordinate system

A general description of cavity flow is given in the review by Rockwell and Naudascher[3]. The behavior of the flow was found to be dramatically different depending on the parameters of the cavity geometry (cavity length L and depth D: see Figure 1.1) in addition to the condition of the boundary layer at separation. Sarohia[4] defined a rough boundary between *deep* and *shallow* cavities as $L/D=1$. Cavities with $L/D<1$ were considered as *deep* cavities, while those with $L/D>1$ were taken as *shallow*. Deep cavities act as Helmholtz resonators, and the shear layer above the cavity provides the forcing mechanism. East[5] experimentally studied deep cavities and validated that the resonance frequencies corresponded to the acoustic depth modes of the cavity. Ma *et al.*[6] studied flow-induced Helmholtz resonance experimentally and theoretically. They proposed a model which successfully predicted the frequency and magnitude of the resonance based on the momentum balance for a control volume surrounding the resonator's opening. In the numerical investigations by Tam[7], he found that the acoustic depth modes were strongly damped due to acoustic radiation for shallow cavities with $L/D>1$. Acoustic depth modes could not be sustained in shallow cavities at low Mach number. The present work is focused on studying shallow cavities only.

Shallow cavities are further classified into *open* or *closed* as defined by Charwat *et al.*[8]. A cavity is said to closed if the shear layer reattaches on the bottom wall and separates again ahead of the downstream edge; otherwise, the cavity is considered open. In their study of a supersonic cavity flow with a turbulent separating boundary layer, Charwat *et al.* found the transition from open to closed cavity flow takes place when the aspect ratio *L/D* exceeded 11. On the other hand, in the investigation of a subsonic cavity flow with a laminar separation by Sarohia[4], the transition occurred at *L/D* = 7 - 8. Only open cavities are studied here.

Rossiter [9] identified the basic mechanism leading to strong, self-sustained oscillations in open cavities at relatively high Mach number. Specifically, small disturbances in the shear layer separating at the upstream edge of the cavity are amplified, forming periodic vortex structures that travel downstream and interact with the aft edge of the cavity, generating strong pressure fluctuations. These fluctuations propagate ("feedback") to the upstream edge acoustically and re-excite the shear layer at the separation point. This forms strong, self-excited, self-sustained flow oscillations, or "Rossiter" modes. Based on the idea that for self-sustained oscillation to occur, the time duration for the travel of a disturbance from the upstream lip to the downstream edge of the cavity and back must equal an integer multiple of the period of the oscillation, Rossiter proposed the following formula for identifying the frequencies (*f*) of oscillation:

$$\frac{fL}{U_\infty} = \frac{m - \gamma}{M + 1/k} \qquad \textbf{1.1}$$

where, L is the cavity length, U_∞ is the freestream velocity, M is the Mach number, m is an integer mode number (1, 2, ...), k is the ratio of the convection speed of the vortex

structures (U_c) to the free-stream velocity, and γ is a parameter representing the time delay between the interaction of the vortex structure with the downstream lip and subsequent generation of sound. γ and k are treated as empirical parameters that are adjusted to fit the observed frequencies of self-sustained oscillation in a particular experiment. Rossiter employed values of 0.25 and 0.57, respectively, for these parameters. The "Rossiter mechanism" and equation 1.1 have been validated in many of the experimental and numerical studies of open cavity flow, especially at relatively high Mach number (for instance, see Ahuja and Mendoza[10], Rowley *et al.*[11] and Murray and Ukeiley[12]).

For open cavities, a notable deviation from the Rossiter mechanism that has been reported at low Mach number, but generally received lesser attention, is the case where the oscillations of the flow may not involve periodic vortex shedding from the upstream edge, and the vortex-edge interaction is inefficient in producing significant acoustic disturbances to excite the shear layer at separation. In this situation, self-sustained oscillations can still exist, but they are driven by convective waves which cause large lateral motion (or "flapping") of the shear layer near the downstream lip of the cavity (e.g. Sarohia[4] and Chatellier *et al.*[13]); and the observed frequencies of oscillation deviate from those predicted from Rossiter's equation. Unlike the Rossiter modes, it is believed that the self-sustained oscillations in this case are driven by the fluctuation of the fluid volume trapped inside the cavity by the shear layer. Martin *et al.*[14] and Rockwell[15] predicted the frequency of the oscillation tones by invoking a π phase angle between the entrapped-volume fluctuation and the lateral displacement of the shear layer at separation.

The flow dynamics of cavities is further complicated by the possible existence of a completely different mode of oscillation. Gharib and Roshko[16] investigated the flow over an axisymmetric cavity with a laminar boundary layer at separation and showed that above a certain value of L/D, the flow field became unstable on a large scale, comparable to the depth of the cavity. The resulting flow structures resembled those found in a bluff-body wake. This behavior was referred to as 'wake mode'. Gharib and Roshko observed an abrupt, large increase in the drag force on the cavity associated with the wake mode due to the large difference in pressure acting on the downstream and upstream cavity wall. The wake mode was also found later in the numerical simulation by Najm and Ghoniem[17]. Although not referred to as the wake mode, these authors observed that for $L/D > 2$, the cavity flow switched from being driven by shear-layer instability to being dominated by shedding of larger-scale, lower-frequency vortices from the recirculation zone inside the cavity. More recently, Rowley *et al.*[11] showed that the transition of the flow from shear-layer (Rossiter) to wake mode of oscillation took place when the length of the cavity became large compared to the upstream-boundary-layer thickness, or as the Mach or Reynolds numbers were raised. Rowley *et al.* suggested that the wake mode was sustained by an absolute instability of the flow.

1.2 Motivation

Even though there is a large body of literature on cavity flows, most of them are based on the assumption that the flow is two-dimensional. However, in reality several sources of three-dimensionality can be identified. Of these, the most prominent are: (1) the effect of the side walls of the cavity; and (2) the instabilities arising from the recirculation flow within the cavity. Very few studies exist of the three-dimensional effects resulting from these influences and if/how these effects alter the self-sustained cavity oscillations

In the experiments of Maull and East[18], the flow in the cavity was found to have cellular structures along the span. The number, configuration and distribution of the cells were affected by the width-to-length ratio (W/L), depth-to-length ratio (D/L) and the shape of the cavity. No quantitative measurements of the cavity unsteadiness were reported. Rockwell and Knisely [19] utilized hydrogen bubble to visualize the three-dimensional nature of the unsteady flow past a cavity. They found secondary, spanwise-periodic, streamwise vortices to form and distort the primary spanwise vortex structures. Although they could not elaborate on the mechanism that led to the formation of the streamwise vortices, they suggested that the recirculation flow inside the cavity had an influence on the formation process. More recently, three-dimensional-instability analysis of a cavity flow that is *two-dimensional* in the mean was done by Bres and Colonius[20]. They found that the most amplified three-dimensional mode had a spanwise wavelength that scaled with the cavity depth, and a typical frequency that was an order of magnitude smaller than the frequency of the self-sustained cavity oscillations. Bres and Colonius

related this mode to the centrifugal instability of the primary recirculation flow inside the cavity.

None of the above studies reported how the cavity width and the side walls affect the self-sustained oscillations. In experiments, the influence from the cavity side walls is typically minimized by simply using a large cavity width-to-depth ratio and focusing only on the symmetry plane along the span. Real cavities, however, have finite width; but present understanding of the self-sustained oscillations in flows over cavities ignores this fact. This implicitly assumes that the cavity width is immaterial for the establishment of cavity oscillations.

Plumbee *et al.*[21] observed that a factor of 2 change in the cavity width had no effect on the frequency of the first two Rossiter modes at $M = 2$. The effect of the cavity width on the amplitude of the oscillation was not reported. Studies on the radiated noise from cavities by Block[22] showed that the cavity width appeared to determine whether the cavity acts as a narrowband or broadband source at a given velocity. She observed that for cavities with $L/D \approx 1$ and 2, the radiated noise from the narrower cavity had a sharper-shape spectrum and higher amplitude than that from the wider cavity even though the spectra peaked at the same frequency. In contrast, data from Ahuja and Mendoza[10] on the far-field acoustic radiation from the cavity flow indicated trends opposite to that reported by Block. Ahuja and Mendoza noted that the flow was two-dimensional if $W/L > 1$, while three-dimensional effects became notable for $W/L < 1$. Far-field acoustic measurement showed that the three-dimensional cavity flow ($W/L < 1$) produced lower levels of cavity feedback tones as well as broadband noise compared to the two-dimensional cavity flow ($W/L > 1$). They attributed the reduction of sound pressure level to the loss of coherence

of the shear layer across the cavity width. However no evidence was provided regarding the coherence of the shear layer along the span and how the coherence was related to the mechanism driving the oscillation. Moreover, there were no measurements demonstrating that the oscillations inside the cavity had the same characteristics as the radiated noise in the far field. Both Block[22] and Ahuja and Mendoza[10]'s studies also focused only on the high-frequency far-field noise radiated from the cavity. The effect of cavity width/side walls on the oscillations and three-dimensional flow structures within the cavity were never studied in detail.

Larcheveque *et al.*[23] numerically studied a three-dimensional cavity flow with L/D of 5 and W/L of 0.2 at M = 0.85. They reported that the turbulent kinetic energy distribution in the mixing layer was less two-dimensional at low frequency, especially near the aft wall. They claimed that the strong streamwise vortices ejected near the corners induced strong *low-frequency three-dimensionality*. There was, however, no detailed discussion of this low-frequency, the three-dimensionality and the vortices near the corners since the pressure fluctuations on the floor of the cavity in their case were dominated by Rossiter modes which were homogeneous in the spanwise direction.

1.3 Objectives

The current study is focused on examining the unsteady flow and surface-pressure in a low-Mach-number cavity flow with a turbulent boundary layer at separation. The primary concern is to investigate the effect of the cavity width and side walls on the flow. In particular, answers to the following questions are sought: what is the effect of the cavity width and side walls on the unsteady-flow behavior? If two-dimensional self-sustained oscillations exist, does the cavity width/side wall alter the strength, frequency, or mode shape of these oscillations? If so, what is the physical mechanism through which this alteration takes place?

For the purpose of the investigation, an axisymmetric cavity geometry is employed. The axisymmetric configuration has a distinct advantage in studying the cavity-width/side-wall effects. In particular, the geometry is free from any side-wall influence, as seen in Figure 1.2 (a), but could be partially filled to form finite-width cavities, as depicted in Figure 1.2 (b). It is significant to contrast the present work to the study of Block[22], Ahuja and Mendoza[10] and Larcheveque *et al.*[23]. These studies employed rectangular cavity geometry that had to be terminated with end walls (even for the widest cavity). One of the unique features of the present study is the "reference" condition established by the axisymmetric cavity that is free of any side-wall influences and the comparison of that condition with cavities with different widths. The handful experimental studies involving axisymmetric cavity flows in the literature (Sarohia[4] and Gharib and Roshko[16]) did not include any examination of the effect of the cavity width. Moreover these experimental studies only considered the laminar boundary layer case. Another unique aspect of the present work is the extensive space-time unsteady wall

pressure information collected along the streamwise direction on the cavity floor and the azimuthal direction on the downstream wall simultaneously with flow velocity measurements.

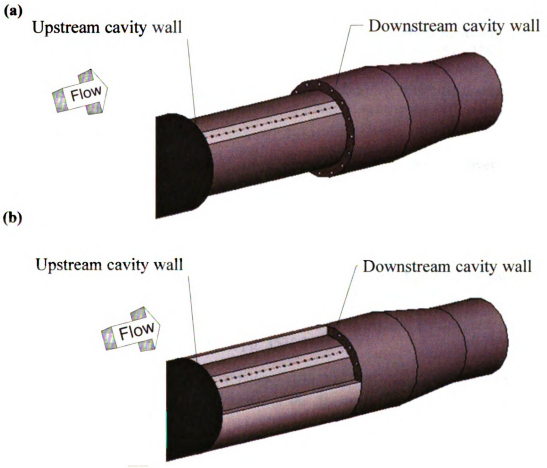

Figure 1.2 Cavity model: (a) axisymmetric cavity (b) finite-width cavity

1.4 References

[1] Cattafesta, L., Williams, D., Rowley, C., and Alvi, F., "Review of Active Control of Flow-Induced Cavity Resonance." *AIAA Paper* 2003-3567 (2003)

[2] Rowley, C.W. and Williams, D.R., "Dynamics and Control of High-Reynolds-Number Flow over Open Cavities," *Annual Review of Fluid Mechanics* **38**, pp. 251-276 (2006)

[3] Rockwell, D. and Naudascher, E., "Review – self-sustaining oscillations of flow past cavities," Transactions of the ASME: *Journal of Fluids Engineering* **100**, pp. 152 – 165 (1978)

[4] Sarohia, V., "Experimental Investigation of Oscillations in Flows Over Shallow Cavities," *AIAA Journal* **15** (7), pp. 984-991 (1977)

[5] East, L.F., "Aerodynamic Induced Resonance in Rectangular Cavities," *Journal of Sound and Vibrations* **3**, pp. 277-287 (1966)

[6] Ma, R., Slaboch, P. and Morris, S.C., " Fluid Mechanics of the Flow-Excited Helmholz Resonator," *Journal of Fluid Mechanics* **623**, pp. 1-26 (2009)

[7] Tam, C.K.W., "The Acoustic Modes of a Two-Dimensional Rectangular Cavity," *Journal of Sound and Vibrations* **49** (3), pp. 353-364 (1976)

[8] Charwat, A.F., Roos, J.N., Dewey, F.C. and Hitz, J.A., "An Investigation of Separated Flows. Part 1. The Pressure Field," *Journal of the Aerospace Sciences* **28**, pp. 457-470 (1961)

[9] Rossiter, J.E., "Wind-tunnel Experiments on the Flow over Rectangular Cavities at Subsonic and Transonic Speeds," *Technical Report 3438, Aeronautical Research Council Reports and Memoranda* (1964)

[10] Ahuja, K.K and Mendoza, J. "Effects of Cavity Dimensions, Boundary Layer, and Temperature on Cavity Noise with Emphasis on Benchmark Data to Validate Computational Aeroacoustic Codes", *Contractor Report 4653, National Aeronautics and Space Administration* (1995)

[11] Rowley, C.W., Colonius, T. and Basu, A.J., "On Self-sustained Oscillations in Two-dimensional Compressible Flow over Rectanguler Cavities", *Journal of Fluid Mechanics* **455**, pp. 315-346 (2002)

[12] Murray, N. and Ukeiley, L., "Estimationof the flowfield from surface pressure measurements in an open cavity," *AIAA Journal,* **41** (5), pp. 969-972 (2003)

[13] Chatellier, L., Laumonier, J., and Gervais, Y., " Theoretical and Experimental Investigations of Low Mach Number Turbulent Vavity Flows," *Experiments in Fluids* **36**, pp. 728 - 740 (2004)

[14] Martin, W.W., Naudascher, E.,and Padmanabhan, M., "Fluid-dynamic Excitation Involving Flow Instability," *Journal of the Hydraulics Division, ASCE* **101** (HY6), pp. 681 - 698 (1975)

[15] Rockwell, D., "Prediction of Oscillation Frequencies for Unstable Flow Past Cavities," *Journal of Fluids Engineering* **99**, pp. 294 - 300 (1977)

[16] Gharib, M., Roshko, A.F., "The Effect of Flow Oscillations on Cavity Drag," *Journal of Fluid Mechanics* **177**, pp. 501 - 530 (1987)

[17] Najm, H.N., Ghoniem, A.F., "Numerical simulation of the convective instability in a dump combustor," *AIAA Journal,* **29** (6), pp. 911 - 919 (1991)

[18] Maull, D.J., and East, L.F., "Three-dimensional Flow in Cavities," *Journal of Fluid Mechanics* **16**, pp. 620 - 632 (1963)

[19] Rockwell, D., and Knisely, C., "Observations of the Three-dimensional Nature of Unstable Flow Past a Cavity," *Physics of Fluids* **23** (3), pp. 425 - 431 (1980)

[20] Bres, G.A., and Colonius, T., "Three-dimensional Instability in Compressible Flow over Open Cavities," *Journal of Fluid Mechanics* **599**, pp. 309-339, (2008)

[21] Plumbee, H.E., Gibson, J.S. and Lassiter, L.W., "A Theoretical and Experimental Investigation of the Acoustic Response of Cavities in an Aerodynamic Flow", *Technical Report WADD-TR-61-75, US Air Force* (1962)

[22] Block, P.J.W., "Noise Response of Cavities of Varying Dimensions at Subsonic Speeds", *Technical Notes D-8351, National Aeronautics and Space Administration* (1976)

[23] Larcheveque, L., Sagaut, P., Le, T. and Comte, P., "Large-eddy Simulation of a Compressible Flow in a Three-dimensional Open Cavity at High Reynolds Number", *Journal of Fluid Mechanics* **516**, pp. 265 - 301 (2004)

2. EXPERIMENTAL SETUP AND MEASUREMENT TECHNIQUES

2.1 Wind Tunnel Facility and Cavity Model

The present experiment is conducted in an open-circuit wind tunnel in the Flow Physics and Control Laboratory (FPaCL) at MSU. A schematic drawing of the wind tunnel is shown in Figure 2.1. The tunnel has a 1.829 m-long test section downstream of a contraction with a 6.25:1 area ratio and a 1.549 m-wide by 1.549 m-high inlet cross section. An aluminum honeycomb followed by three stainless steel mesh screens and a non-woven fiberglass filter are mounted ahead of the contraction inlet to reduce the turbulence intensity within the test section to less than 0.5% based on the streamwise velocity component. A false ceiling with an adjustable angle is used to maintain zero pressure gradient in the test section along the streamwise direction starting from a cross section area of 0.610 m- by 0.610 m at the upstream end. Two slots with a width of 0.0127 m along the centerline of the test section's false and main ceiling allow for the insertion of probes. The air flow exiting the test section is slowed down through a combination of a pre-diffuser and a diffuser. The bottom wall of the pre-diffuser has an angle of 6 degrees with respect to the horizontal direction; while the top wall is hinged on the downstream end and is set to a typically very small angle to accommodate the position of the test-section's movable ceiling at the exit of the latter. The diffuser has a divergence angle of 5.9 degrees. A gap filled with rubber is left between the pre-diffuser and the diffuser to minimize the transmission of vibration from the fan to the test section.

Acrylic windows in the side walls and bottom of the test section, as well as in the pre-diffuser enable optical access to the tunnel. A Pitot tube with an outside diameter of 3 mm and an Omega (DP-25-TH) thermistor are inserted in the wind tunnel to monitor the free-stream velocity and temperature respectively. The pressure differential produced by the Pitot tube is monitored used 10 torr Baratron (model 223BD) pressure transducer with 0.0075 V/Pa sensitivity. On the other hand, the sensitivity of the temperature sensor is 0.1 V/°C.

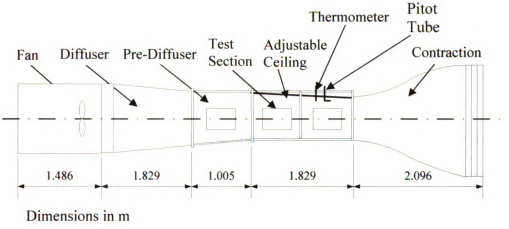

Figure 2.1 Schematic diagram of the wind tunnel

The model used to establish the cavity flow is based on the axisymmetric backward-facing-step model employed in different earlier studies at the FPaCL (Li[1], Hudy[2], Trosin[3] and Aditjandra[4]). The dimensions of the back-step model are shown in Figure 2.2. A spherical nose is used at the leading edge of the model. Because it is desired to establish a turbulent boundary layer at the separation point of the back step, any disturbances caused by the curvature discontinuity between the nose and the stationary section immediately downstream benefit the quicker development of the boundary to a turbulent state. In addition, sandpaper is used at the upstream end of the model to hasten the boundary-layer transition. Cavities with different lengths and widths

are formed on the model by assembling a movable 'Downstream Cavity Wall' and 'Inserts for *W/D* Control' on the model downstream of the back step, as seen in Figure 2.3. Both parts are made from two halves which could be assembled around the central shaft inside the cavity. The downstream cavity wall is movable along the model's axis in order to enable variation of the aspect, or *L/D*, ratio of the cavity. The inserts for *W/D* control are employed to fill a portion of the cavity along the azimuthal direction in order to create finite-width cavities with different width-to-depth (*W/D*) ratios. By varying the length and azimuthal extent of the inserts it is possible to vary *L/D* and *W/D*. Note that *W* is defined here as the azimuthal arc length at a height of *D*/2 above the cavity floor (*D* = 12.2 mm).

The downstream cavity wall is composed of a 152 mm-long cylindrical shell upstream of a 50.8 mm-long conical shell. The latter is employed to eliminate any possible influence of disturbances from the flow past the downstream step of the cylindrical shell on the flow structure in the cavity. Preliminary tests show that when the cylindrical shell's length is larger than approximately 100 mm, the pressure signature on the cavity floor remains independent of the shell's length. A 12.2 mm-long segment at the upstream end of the cylindrical shell is detachable (labeled "Detachable Sensor Ring" in Figure 2.3) and is employed to house an azimuthal microphone array for measuring the unsteady pressure on the downstream cavity wall. Details of this array are described in section 2.2.3.

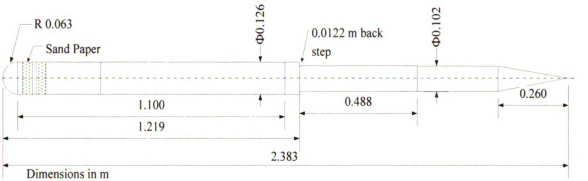

Figure 2.2 A schematic drawing of the axisymmetric test model

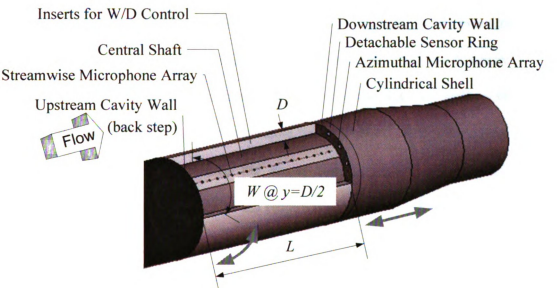

Figure 2.3 Three-dimensional drawing of the cavity model (note *W* is measured at height of *D/2* above the cavity bottom)

2.2 Measurement Techniques

The measurement techniques employed in this study include hot wires, "static-pressure taps", microphones and Laser Doppler Anemometry (LDA). A single hot wire is used to measure the boundary-layer streamwise-velocity profile at the separation point to characterize the state of the boundary layer. 56 static pressure taps and 32 microphones are embedded in the model downstream of the backward-facing step. The pressure taps are used to align the model in the wind tunnel. The 32 microphones form a "streamwise microphone array", which is employed to measure the unsteady wall pressure on the cavity bottom. In addition, arrays of microphones are integrated into the downstream wall of the cavity to characterize the azimuthal distribution of the unsteady wall pressure. The streamwise (u) and wall-normal (v) components (in the x and y directions respectively) of the velocity field inside and above the cavity are measured using Laser Doppler Anemometry. Further details of each of the employed methods are given below.

2.2.1 Hot-wire Measurements

A single hot wire is employed to measure the velocity profile of the boundary layer at the separation point. The hot wire is made from tungsten with a diameter of 3.75 μm and a sensing length of about 0.8 mm. This corresponds to a wire length-to-diameter ratio of more than 200 and a typical electrical resistance of 5 Ω. A Constant Temperature Anemometer (CTA), Dantec Mini CTA 54T30, is used to operate the hot wire, with the overheat ratio set to 1.62. The hot wire probe is mounted on a 15" Velmex A2515C-S2.5 screw-drive Unislide traverse with 40 turns per inch of movement. The traverse is driven by a TMG 5618S-01 hybrid stepper motor which has an angular resolution of 800 steps

per revolution. The traverse system is employed to move the hot wire along the y direction with a resolution of 0.823 μm per step (based on calibration of the movement).

The velocity-profile measurement is conducted at 5 mm upstream of the separation point, starting from about 0.3 mm above the wall. The probe is traversed in the y direction with an increment that varies from 0.08 mm closest to the wall to 5 mm in the free stream. To determine the initial position of the hot wire above the wall, the probe is imaged using a standard-video Sony CCD camera (XC-75), which is connected to a National Instruments IMAQ PC-board PCI-1411 frame grabber. The imaging is achieved using a Nikkor 500 mm lens and an illumination source consisting of a high-intensity white light (a Stocker & Yale, Inc, Lite Mite Series Model 13 Plus). Figure 2.4 shows an image exemplifying those used to determine the wire height above the wall. The height is determined by the number of pixels in the image between the wire (i.e. end of the probe prongs) and the surface of the model with known image scale (typically 0.03 mm/pixel) that is calibrated by determining the average number of pixels by which the wire is traversed in the image when it is moved 1 mm upwards in the y direction.

Because of the directional ambiguity of the hot wire, measurement in the boundary layer yields the velocity magnitude q ($q = \sqrt{u^2 + v^2}$ where u and v are the streamwise and wall-normal velocity components respectively). Since the wall-normal velocity component is much less than the streamwise velocity in the boundary layer, the measurement could be interpreted as the streamwise velocity u.

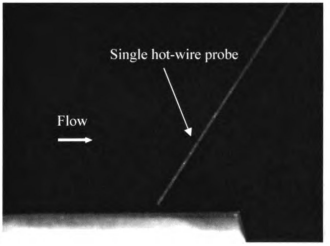

Figure 2.4 An image of the single hot wire above the axisymmetric model surface

The hot wire is calibrated in the free stream in the wind tunnel against the Pitot tube, shown in Figure 2.1, coupled with a pressure transducer (Baratron 223 BD-000010ACU with measurement range 0-1333 Pa). The output of the hot wire, pressure transducer and thermometer at different tunnel velocities, are sampled at a frequency of 1000 Hz for 10 seconds. The variation in the average voltage (E) of the hot wire with free-stream velocity (U_∞) is curve-fitted to the "King's-law" equation:

$$E^2 = A + BU_\infty^n, \qquad \textbf{2.1}$$

where n is set to 0.45. Temperature correction to the output voltage of the hot wire is conducted using the equation

$$E = E_r \sqrt{\frac{T_w - T_{cal}}{T_w - T_r}} \qquad \textbf{2.2}$$

to eliminate the effect of any temperature variation between the calibration and data acquisition; where E_r is the raw output voltage of the hot wire, T_w is the hot-wire temperature, T_{cal} is the flow temperature when the calibration is performed, and T_r is the

flow temperature during acquisition. Figure 2.5 shows an example of the hot-wire calibration data and King's law curve fit. For all measurements reported here, the maximum error between calibrations conducted before (pre) and after (post) acquisition of data was less than 2%.

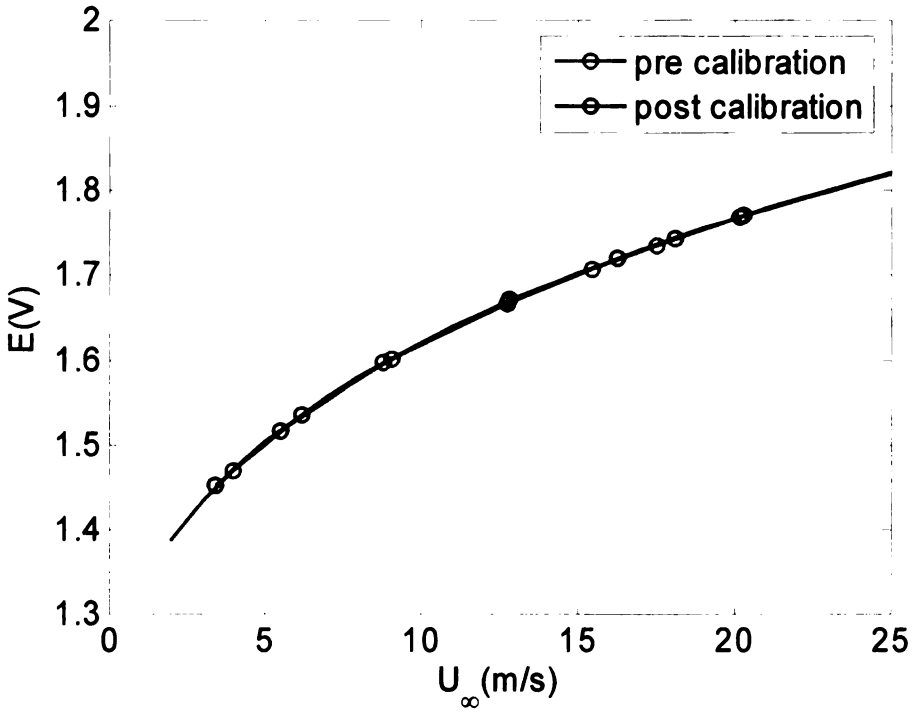

Figure 2.5 Example of a hot-wire calibration

2.2.2 Static Pressure Taps

Downstream of the step (the separation point), there are four slots cut in the model at 90° intervals around the perimeter for insertion of wall sensors. 32 pressure taps are located next to the streamwise-array microphones in a plug fitted in the top slot. The microphones, which are deployed along the centerline of the model, are offset from the pressure taps by 3.2 mm center-to-center in the azimuthal direction. The taps have an inside diameter of 1 mm and are spaced 4.75 mm apart in the streamwise direction,

starting from 5.3 mm downstream of the step. The remaining 24 pressure taps are embedded in plugs inserted into two side and one bottom slots of the model; i.e. eight taps per plug. These taps are spaced 9.5 mm apart in x starting at 19.55 mm downstream of the step. All of the taps are connected using Urethane tubes to a Scanivalve pressure scanner system. The output port of the Scanivalve is connected to the positive input of a pressure transducer (Setra model 239 with measurement range 0-0.5 inch H_2O). The negative input of the transducer is the reference pressure and is connected to the static-pressure port of the free-stream Pitot tube. Stepping of the Scanivalve is controlled using a digital-to-analog converter of a general purpose National Instruments data acquisition PC board. The board is controlled using a LabView program running on a PC computer. The static pressures are acquired for 10 seconds with a sampling frequency of 100 Hz. One second time delay is used between measurements from consecutive ports to eliminate transient effect associated with switching pressure ports. More details of the pressure taps and the Scanivalve system can be found in section 2.3 of Hudy[2].

2.2.3 Microphone Arrays

An array consisting of 32 Knowles Electronics FG-23629-P16 microphones are mounted along the centerline of the top slot in the model; labeled 'Streamwise Microphone Array' in Figure 2.3. The sensors, which have an outside diameter of 2.54 mm and sensing diameter of 0.75 mm, are spaced 4.75 mm apart in the streamwise direction, starting from 5.3 mm downstream of the upstream cavity edge. Additional information about the streamwise microphone array including the circuitry can be found in section 8.4 of Hudy[2].

Another wall-pressure-sensor array, labeled 'Azimuthal Microphone Array' in Figure 2.3, is integrated into the downstream wall of the cavity at a height equal to half the cavity depth (i.e. 6.1 mm) above the cavity floor. This array is embedded in the 12.2 mm-long Detachable Sensor Ring (shown in Figure 2.3), which could be replaced so that arrays with different configurations could be employed along the azimuthal direction. Two such arrays are used in this study. One consisting of 14 Knowles Electronics FG-23629-P16 microphones, deployed over only a portion of the perimeter, is used for the study of cavities with finite width; another array with 16 Panasonic WM-61-A microphones covering the whole circumference of the model is used to characterize the azimuthal variation of the unsteady pressure in the axisymmetric cavities.

The Knowles Electronics microphones have the same dimensions as the ones in the streamwise array. The arrangement of these microphones in the azimuthal array is shown in Figure 2.6. They extend over an azimuthal angle, ϕ (see definition of ϕ in Figure 2.6), range of -40° to +20° with an inter-sensor spacing of 4° except near -40° where a coarser spacing of 8° is used. This array is used for measurements in cavities with azimuthal extent varying between 30° and 90°. In contrast, the Panasonic microphones have an outside diameter of 6 mm and sensing diameter of 2 mm with a uniform azimuthal spacing of 22.5°. 32-AWG wires are used to connect the microphones with the operating circuits (see Appendix 6.1 for detailed description of the construction of the microphone arrays). The wires are threaded to the outside of the test section through the gap between the cylindrical shell and the model's surface.

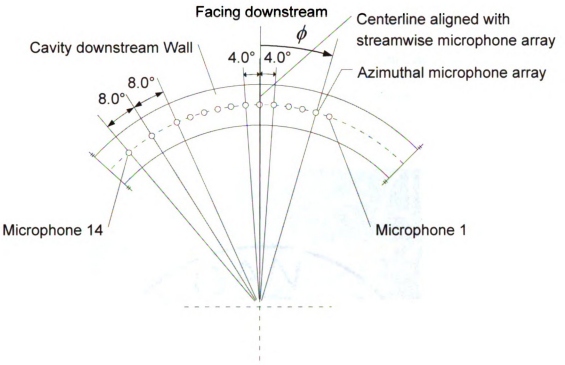

Figure 2.6 Configuration of the azimuthal Knowles Electronics microphone array

The streamwise-array's microphones are calibrated individually in-situ against a B&K 4938-A-011 1/4" microphone with a manufacturer-supplied response. The calibration is performed by subjecting the Knowles and B&K microphones to sound waves in a custom made plane wave tube (PWT) that could be clamped on the model (see Figure 2.7) in the wind tunnel. The tube is driven by a speaker located upstream of the entrance of the wind tunnel. The PWT produces plane sound waves that travel parallel to the axis of the tube. Such one-dimensional planar waves with wavelength λ_a are achievable in a square duct with rigid walls and side length 2a when λ_a>4a, or f<c/4a (where f is the sound frequency and c is the speed of sound); see Kinsler *et al*[5]. The width of the PWT in this study is 18.3 mm, which gives an upper frequency limit of 9.6 kHz for a speed of sound of 350 m/s.

To conduct the calibration, the PWT is clamped on the model as depicted in Figure 2.7 with the centerline of the tube aligned with the center of the microphone holes. The B&K microphone is mounted on the centerline of the moveable upper wall of the PWT. By sliding the upper wall it is possible to align the B&K microphone with each Emkay microphone in the sensor array to perform the calibration.

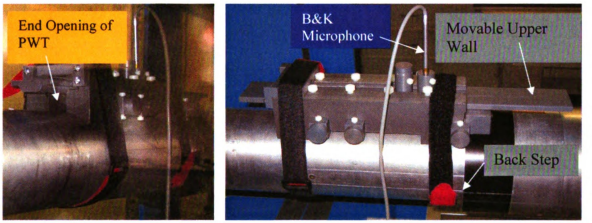

Figure 2.7 Photographic views of the PWT for calibration of the streamwise-array's microphones

To verify the planar-sound-wave nature of the sound traveling within the PWT, measurements were conducted using two B&K microphones mounted at the same cross section of the tube. This was done at three different cross sections, including those corresponding to the beginning and end of the tube. The data were used to calculate the ratio of sound amplitude measured by each of the B&K microphones and the phase shift between the two measurements. Figure 2.8 provides the average of the results for the three cross sections. The results in Figure 2.8 are shown for the frequency range extending up to 1000 Hz only, which is well beyond the highest frequency of wall-pressure fluctuations found in the cavity flow. As seen from the figure, the results indicate uniform sound amplitude and phase across a given cross section of the PWT; i.e.,

corresponding to planar sound waves, up to the end of the frequency range of interest. For reference, the individual sensitivity values for the upstream most 24 microphones used in this experiment are plotted in Figure 2.9. The phase-angle calibration shows a maximum 12 μs time delay between any pair of Emkay microphones over all frequencies, which is less than 0.4% of the shortest time scale of interest (300Hz) in the cavity flow.

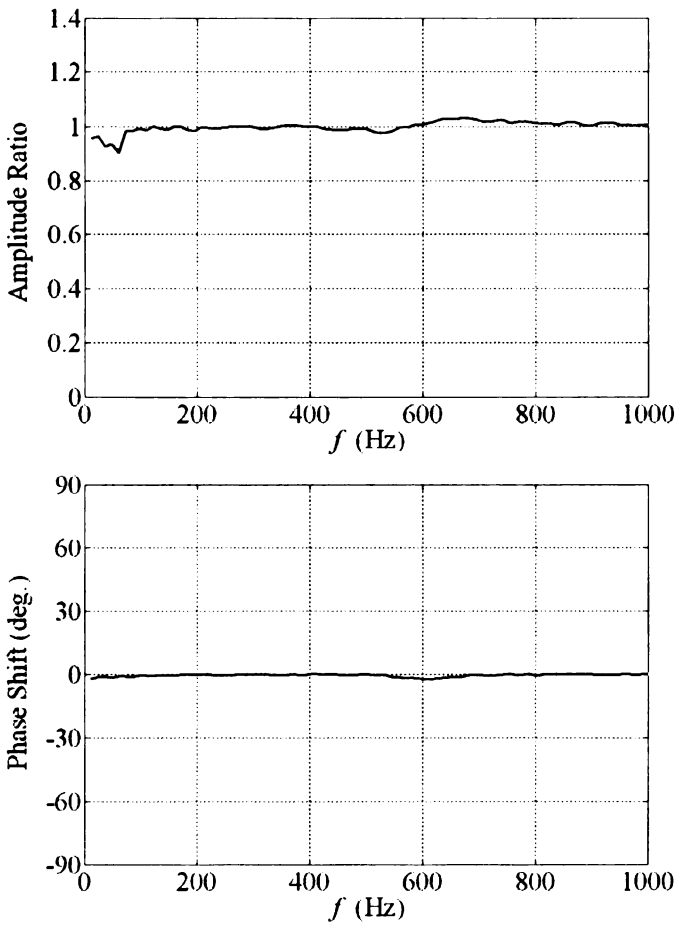

Figure 2.8 Calibration of the PWT: amplitude ratio (top) and phase shift (bottom)

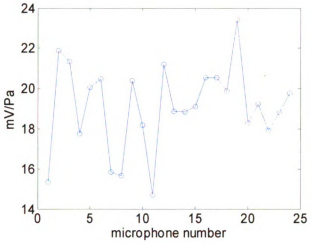

Figure 2.9 Sensitivity of the streamwise-array's microphones

The azimuthal-array's microphones were also calibrated individually, *after insertion into the cavity's end wall*, against a B&K 4938-A-011 1/4" microphone in a custom made PWT outside the wind tunnel, as shown in Figure 2.10. The PWT was clamped on a metal plate which has a circular cut-out in the middle to accommodate the ring into which the azimuthal-array's microphones are fitted. The PWT is driven by a speaker located at one of the tube's ends.

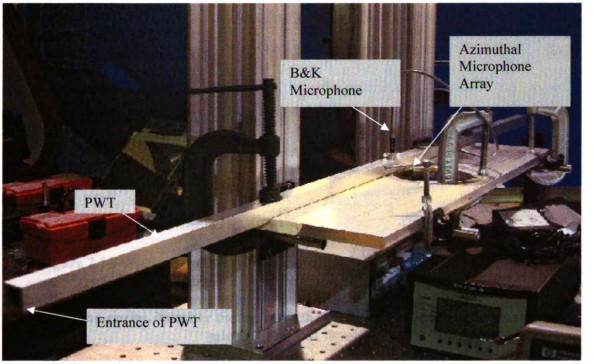

Figure 2.10 Setup for calibration of the azimuthal-array's microphones

For reference, the individual sensitivity values for the azimuthal-array's microphones are given in Figure 2.11. Also, the calibration results show that the time delay between any pair of microphones is less than 15.8 μs and 10 μs within the frequency range of interest for the Knowles and Panasonic microphones respectively. This is less than 0.5% of the shortest time scale of interest (300Hz) in the cavity flow.

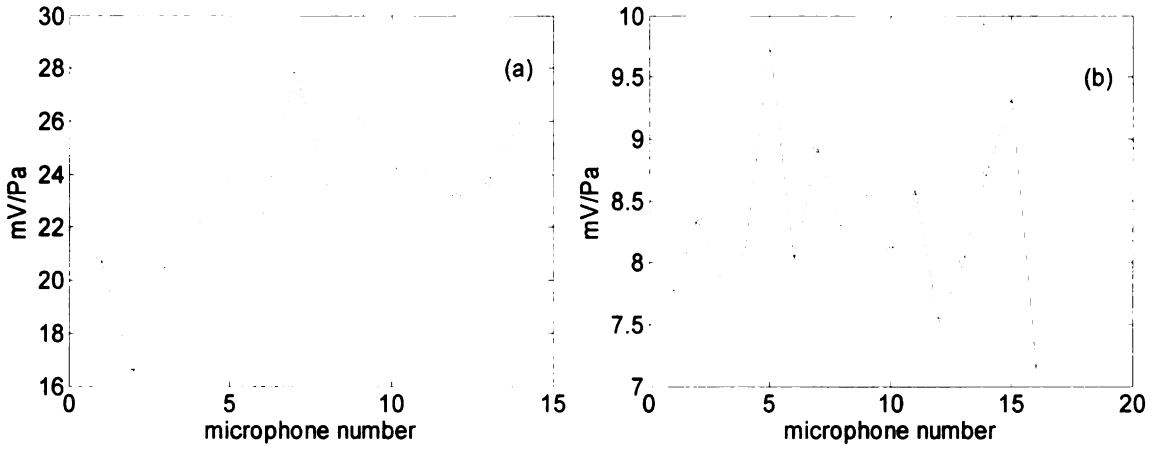

Figure 2.11 Sensitivity of the azimuthal-array's microphones: (a) Knowles microphones (see Figure 2.6 for microphone numbers) and (b) Panasonic microphones (microphone numbers are based on viewing the cavity's end wall from inside the cavity. Number increases in the clockwise direction starting with microphone 1 at the top)

2.2.4 Data Acquisition Hardware

The microphone array data are acquired using two National Instruments A/D PC-based boards (NI-6024E and AT-MIO-16E-10), each of which has 16 single-ended, analog-input channels. The number of streamwise-array's microphones used depends on the length of cavities. Only the most upstream 12 microphones are used in most of this study. In addition, data from a microphone under the downstream wall of the cavity are acquired. These data are used to provide a reference signal for cancellation of any electrical or acoustic fan noise using the optimal filtering technique described in Naguib *et al.*[6]. The streamwise-array's microphones, as well as signals from the pitot tube and thermometer which are used to monitor the tunnel speed, are connected to the AT-MIO-16E-10 board. The board has a 100 kHz maximum sampling rate and a 10 μs inter-channel time delay. On the other hand, the azimuthal-array's sensors are connected to the NI-6024E board which has a maximum sampling rate of 200 kHz and an inter-channel

time delay of 5 μs. The inter-channel time delay between those wall-pressure sensors, when accumulated across all acquired channels, produces a maximum time lag of 110 μs , which is 3.3% of the period of the highest frequency of pressure fluctuations found for the low-Mach-number cavity flow examined here (300 Hz).

The two A/D boards are synchronized by a trigger pulse (AI Scan Start Trigger) that is sent from the AT-MIO-16E-10 board through the programmable function input port 7 (PFI 7) to PFI 0 of the NI-6024E board which is set to accept an external channel scan clock. The AI Scan Start Trigger which reflects the actual start pulse that initiates a scan of the AT-MIO-16E-10 board acts as the channel scan clock for the NI-6024E board. During operation, the NI-6024 board is started first, putting it in an idling state in which it waits for the external clock trigger. Once, the AT-MIO-16E-10 board is run, it sends out the AI Scan Start Trigger which initiates the data sampling of both boards at the same exact time and at the same sampling rate. Synchronization tests are performed by sending pure sine signals from a function generator with frequencies up to 1000Hz to different channels on the two boards; no phase delay is observed between channels on the two different boards (except that caused by the channel multiplexing; the inter-channel delay discussed above).

2.2.5 Laser Doppler Anemometry

A two-component, dual-beam Laser Doppler Anemometer (LDA) is employed to measure u and v at a number of points in the cavity. The LDA technique is based on the Doppler frequency shift of the light scattered from particles that are seeded into the flow. The frequency of the scattered light f_r is given by equation 2.2 (see Adrian[7]), when collecting the light using a stationary detector; where f_b and λ_b is the frequency and

wavelength of the incident light, $\vec{v}_p$ is the particle velocity. This process is illustrated in Figure 2.12 (a).

$$f_r = f_b + \frac{\vec{v}_p \cdot (\vec{e}_r - \vec{e}_b)}{\lambda_b}, \qquad \textbf{2.2}$$

where $\vec{e}_b$ and $\vec{e}_r$ are unit vectors indicating the direction of the incident beam and detected scattered light respectively. In the dual-beam configuration (Figure 2.12 b), the frequencies of the scattered waves from each of the two incident beams can be written as:

$$f_1 = f_b + \frac{\vec{v}_p \cdot (\vec{e}_r - \vec{e}_1)}{\lambda_b} \quad , \quad f_2 = f_b + \frac{\vec{v}_p \cdot (\vec{e}_r - \vec{e}_2)}{\lambda_b} \qquad \textbf{2.3}$$

In practice, the light detector cannot respond fast enough to sense frequencies f_1 and f_2 which are of the order of the frequency of light, and hence the detector only measures the light modulation at the frequency difference f_D (normally called the Doppler frequency):

$$f_D = f_1 - f_2 = \frac{\vec{v}_p \cdot (\vec{e}_2 - \vec{e}_1)}{\lambda_b} = \frac{2\sin(\alpha/2)}{\lambda_b} v_x ; \qquad \textbf{2.4}$$

where v_x represents the particle velocity component along the x direction in Figure 2.12 (b); i.e. the direction perpendicular to the bisector of the angle, α, between the two beams. Given that α and the wavelength of light are known parameters, the particle velocity can be derived from measurement of f_D employing equation 2.4. Note that f_D is independent of the position of the detector in the dual-beam configuration.

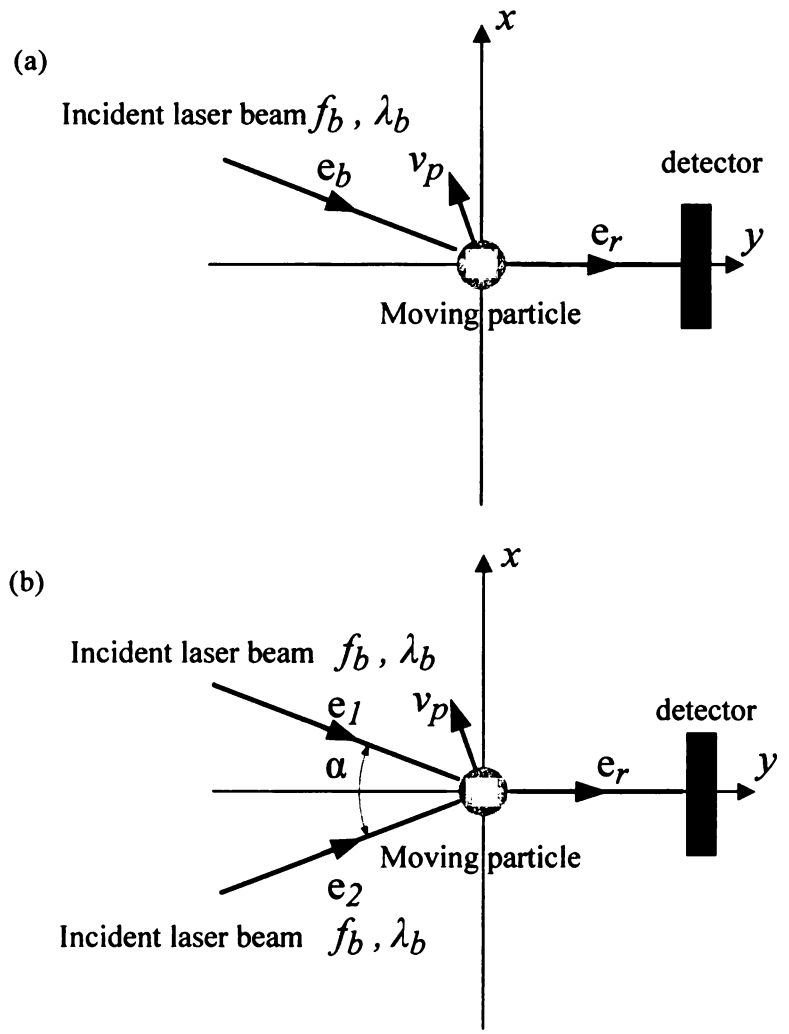

Figure 2.12 Illustration of light scattering from a moving particle: (a) Single-beam configuration (b) Dual-beam configuration

In the present study, a TSI six-jet atomizer (model 9306A) is used to generate the seeding particles from Propylene Glycol solution (one part of Propylene Glycol mixed with 5 parts of water by volume). The atomizer is driven using pressurized air from a compressor line. The density of the generated particles can be controlled by the number of jets and the input pressure. The seeding particles have a mean diameter of 0.35 μm and a maximum diameter of 4 μm based on the specifications of the atomizer. This results in a cut-off frequency of 3 kHz up to which a particle with the maximum diameter can

follow the flow (based on 3 dB cut-off: see Adrian[7]). Particles are injected into the flow at the center of the wind tunnel inlet through a 25.4 mm-diameter tube as shown in Figure 2.13. This focuses the seeding only near the surface of the axisymmetric model and inside the cavity. Measurements of the fluctuating wall-pressure measurements on the cavity floor and the boundary-layer velocity profile at separation with and without the seeding tube upstream of the tunnel entrance show that the presence of the tube upstream of the tunnel inlet does not change the characteristics of the cavity flow.

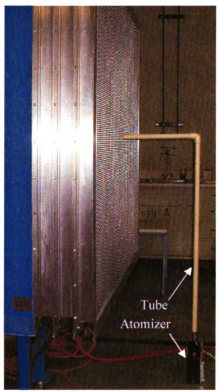

Figure 2.13 Image of the seeding system upstream of the wind tunnel inlet section

The laser beam is generated from a 300 mW argon-ion laser (model 5500A, Ion Laser Technology). This model has standard 300 mW multi-line output. The output beam could be tuned to single line beams from 457 nm to 514 nm using a prism. Beams with three different wavelengths of 514.5 nm (green), 488 nm (blue) and 476.5 nm (violet), at

single line energy of 100mW, 100 mW and 30 mW respectively, are used here. A FiberFlow transmitter from Dantec (Figure 2.14) couples the laser beam to an 85 mm-diameter 2D Dantec probe (Figure 2.15) that steers and focuses the laser beams. Inside the FiberFlow transmitter, the incident laser beam first passes through a Bragg cell, which diffracts the light splitting its power, approximately equally, between the zero- and the first-order diffracted beams and also shifts the frequency of the first-order beam by 40 MHz. The shifted and main beams are separated via a prism into three colors: green (514.5 nm), blue (488 nm) and violet (476.5 nm) for measurements of the three velocity components. Each of the resulting six beams is focused and coupled to a fiber optic cable using micro manipulators to adjust the relative position and angle of the beam and fiber. Only the green and blue beams are used in this study for measurement of u and v respectively. The fibers transmitting these two beams are coupled with the 85 mm probe which is mounted on a three-dimensional traversing system from Dantec to allow the movement of the measurement point of the LDA system (see figure 2.15). The probe contains provisions for steering each of the four beams before focusing them at the measurement point using a lens with a focal length of 500 mm. The same lens is also used to collect the light scattered from the moving particles and focus it on the receiving fiber optic cable. In turn, the latter is coupled to two photo multipliers: one responding to green and the other to blue light. The output of each of the photo multipliers (the "Doppler burst signal") is fed to and analyzed by a Dantec Burst Spectrum Analyzer (BSA 57N11) to extract the Doppler frequency (f_D) from each burst (resulting from light scatter from a single particle passing thought the measurement volume) and convert it to velocity.

Precise alignment had to be done before measurements to couple the laser beam to the transmitter, couple the beams from the transmitter to the optical fibers and locate the beams intersection at the focal point of the scattered-light receiving lens. The procedure to accomplish these tasks is given in Appendix 6.3. For the measurements reported here, the spacing of each of the green and blue beam pairs as they approach the 500 mm focusing lens is 65mm. This gives a beam crossing angle of α = 7.44 degree. The corresponding measurement volume size is d_x = 0.123 mm, d_y = 0.123 mm and d_z = 1.889 mm (in the x, y and azimuthal directions respectively) for the green beam and d_x = 0.116 mm, d_y = 0.116 mm and d_z = 1.889 mm for the blue beam.

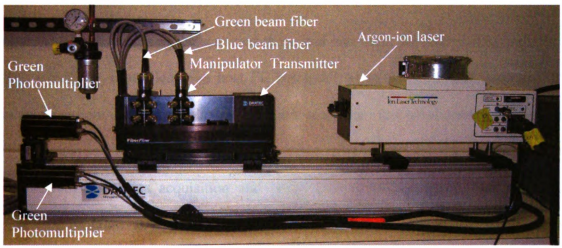

Figure 2.14 Picture of the FiberFlow optics system

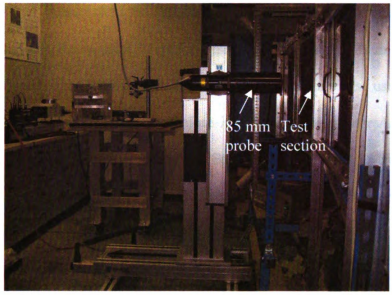

Figure 2.15 Picture of the LDA probe mounted on the three-dimensional traversing system

The burst signals of the scattered green and blue light are analyzed by individual BSAs which are controlled by a host PC computer using an IEEE 488 interface. The traversing system is also controlled by the same computer via a serial connection between the computer and the controller of the traversing systems motors. The parameters and execution of both data acquisition and probe traversing take place using a Dantec application program: BAS Flow Software version 1.2. The two BSAs are synchronized through a synchronization bus and they share the same clock, based on which the arrival times of measurement samples are assigned. Furthermore, the LDA measurement is synchronized with the A/D boards used to sample the unsteady wall pressure using two signals (Sync Reset and CLK) available from the synchronization bus of the BSA. A block diagram illustrating the synchronization with the A/D boards is shown in Figure 2.16. When the acquisition of the LDA system starts, the 'Sync Reset' trigger is sent to the master A/D board (AT-MIO-16E-10). This 'Sync Reset' works as the acquisition-

start trigger of the master A/D board. The scan clock of the master A/D board is generated by dividing down the 1 MHz CLK signal of the BSA, which guarantees the arrival time assigned to the pressure data have the same exact time base used to determine the arrival times of the LDA samples. Before it is sent to the master A/D board (AT-MIO-16E-10), the 1 MHz CLK signal of the BSA is fed to a Schmitt trigger circuit so that the CLK signal sent to the A/D board is regulated to a standard TTL signal. Detail of the Schmitt trigger circuit is described in Appendix 6.2. The slave A/D board (NI-6024E) is synchronized with the master board as described in 2.2.4.

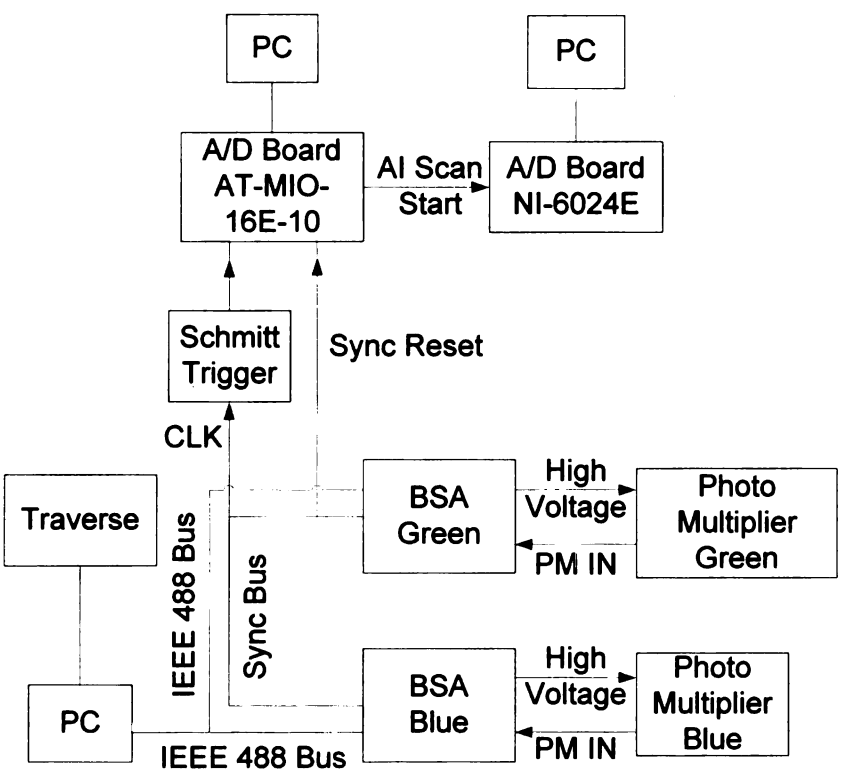

Figure 2.16 Block diagram demonstrating the synchronization of the LDA system with the A/D boards used for acquiring pressure data

The BSA processors perform a validation of the burst signals. In analyzing the spectrum of the burst signals, the BSA compares the two largest local maxima of the

spectrum. If the ratio between them is greater than 4, the spectrum is of good quality and thus the burst is validated. Only the validated data is saved. Overall, the data rate of the measurement is found to be higher in the opening of, than inside the cavity. The maximum data rate in the region of the measurement is about 200 Hz and the lowest is about 1 Hz. Because the data rate is much lower than the frequency of interest, no frequency-spectrum analysis is performed on the velocity data. Instead, to obtain time-dependent information concerning the velocity field, the cross-correlation between the velocity and surface pressure signature is calculated. In turn the conditionally-averaged velocity field associated with the dominated surface pressure signature could be extracted using stochastic estimation (as described in Chapter 4).

Coincident data of the two velocity components in an interval window of 0.01 ms are recorded. This interval window is about 0.3% of the shortest time scale of interest. The measured instantaneous value of the two velocity components, the arriving time and transient time of the particle in the measurement volume for each sample are saved in a text file.

2.3 Experimental Procedure and Parameters

Axisymmetric cavities with variable aspect ratio (L/D) of 3.3, 5, 6.6, 8, and 9.7 were first studied using the streamwise surface-pressure-sensor array. For each aspect ratio, data were acquired at four different free-stream velocities (5, 10, 15 and 20 m/s), resulting in a corresponding Reynolds number based on cavity depth ($Re = U_\infty D/\nu$) of 4067, 8133, 12200 and 16267, respectively. The mean and fluctuating pressure results suggested that for cavities with L/D>5.0, the *initial* development of the flow structure generating the wall pressure downstream of the separation point is inherently similar to the back-step flow of Hudy[2]. In the latter study, which employed the same test model used here, it was demonstrated that the wall-pressure fluctuations were dominated by a *wake mode*. In particular, unlike the traditionally held view of *spatially* growing vortex structures that "impinge" on the wall at reattachment, Hudy *et al.* showed that in the axisymmetric back step the vortex structures rolled up from the initially thin shear layer and grew to a size comparable with the step height while remaining stationary at an x location of 2 – 3 step heights (half way to reattachment). Subsequent to this formation phase, the vortex accelerated to its terminal convection velocity as it traveled downstream. In the present study, the longer cavity aspect ratios (L/D > 5) were found to be too large to interfere with the development of the naturally-existing, back-step wake mode. The inferred existence of the wake mode in longer cavities is also consistent with the observations in the studies of Gharib and Roshko[8], Najm and Ghoniem[9] and Rowley *et al.*[10]. Thus, given the similarity to the back-step flow for L/D > 5, the scope of this thesis is focused on cavities with length to depth ratio of less than five: L/D = 2.6, 3.3 and 4.1. In addition, cases corresponding to width to depth ratio W/D of 2.5, 3.7, 7.4 and "*NW*"

(no-side-wall, or axisymmetric) and four different free-stream velocities (5, 10, 15 and 20 m/s) are examined. The given W/D values correspond to cavities with an angular azimuthal extent of 30°, 45°, and 90°. Also, the Re ($Re = U_\infty D/\nu$) values corresponding to the given free-stream velocities are 4067, 8133, 12200 and 16267, respectively.

2.3.1 Model Alignment

The static pressure taps downstream of the separation point (described in 2.2.2) are used to align the axisymmetric model inside the wind tunnel. This is done prior to mounting of the downstream cavity wall in order to avoid the possibility of establishment of any three-dimensional (azimuthally-varying) mean flow inside the cavity similar to that visualized by Maull and East[11]. The alignment procedure involves utilization of traversing provisions in the model stand to adjust the yaw and pitch angles of the model and its lateral location in the test section. Starting with the model centered in the wind tunnel and its axis parallel to the test-section walls, small adjustments to the yaw and pitch angles are made until the streamwise mean pressure distributions downstream of the step measured from the top, bottom and sides of the model agree to the best possible extent.

The mean static pressure is acquired at 100 Hz for 10 seconds. Figure 2.17 shows the mean-pressure profile on the four sides of the model for Re = 12200. The mean-pressure coefficient $C_p = (p_s - p_r)/ (1/2\rho U_\infty^2)$, is plotted versus the streamwise coordinate normalized by the height of the step. p_s is the mean pressure on the surface of the model and p_r is a reference pressure taken as the static pressure measured by the Pitot tube in the free stream. The results in Figure 2.17 show that the pressure distributions from the

different sides collapse well with the biggest deviation of 4.3% of the overall pressure variation (found at around x/D= 4).

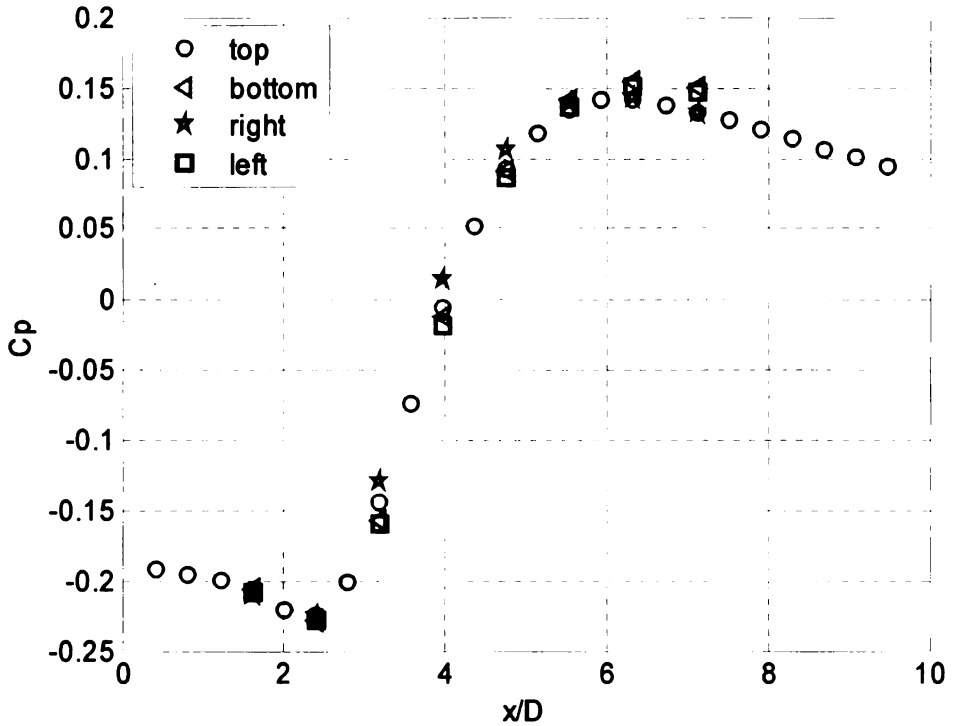

Figure 2.17 Streamwise distribution of the mean-pressure coefficient downstream of the back step at different azimuthal locations around the model (left and right indications in the legend are relative to viewing the model from upstream)

2.3.2 The Boundary Layer State at Separation

The state of the boundary layer at separation highly affects the subsequent development of the shear layer instability. For example, Morris and Foss[12] demonstrated that only the near-wall, or inner-layer, vorticity participated in the initial shear-layer instability in the case of turbulent-flow separation. They showed that "an effective momentum thickness" of $\theta_{eff} = 0.052\theta$ is the appropriate length scale characterizing turbulent separation rather than θ, which is appropriate for the laminar case but has traditionally been used for both laminar and turbulent separations. To characterize the state of the boundary layer at separation, mean streamwise velocity profiles are measured

using a single hot wire. Figure 2.18 shows the velocity profile represented by the blue circles on a semi-log plot at a free-stream velocity of 5 m/s (Figure 2.18 a) and 20 m/s (Figure 2.18 b); the corresponding Reynolds number based on momentum thickness is 1830 and 4387 respectively. The velocity and wall-normal coordinate are normalized by wall units, i.e. $U^+ = U/u_\tau$ and $y^+ = yu_\tau/\nu$, in which $u_\tau = (\tau_w/\rho)^{1/2}$, τ_w is the mean wall shear stress, and ρ and ν are the density and the kinematic viscosity, respectively, of air. The friction velocity u_τ is estimated by fitting the first ten points of the measured profile to the equation of Spalding[13]:

$$y^+ = U^+ + e^{-kB}[e^{kU^+} - 1 - kU^+ - \frac{(kU^+)^2}{2} - \frac{(kU^+)^3}{6}] \qquad \textbf{2.5}$$

The constants used here are k = 0.41 and B = 5.0. This method of estimating the wall shear stress was examined by Kendall and Koochesfahani[14]. They showed that the method has a mean error less than 2% in estimating the friction velocity using Spalding profile.

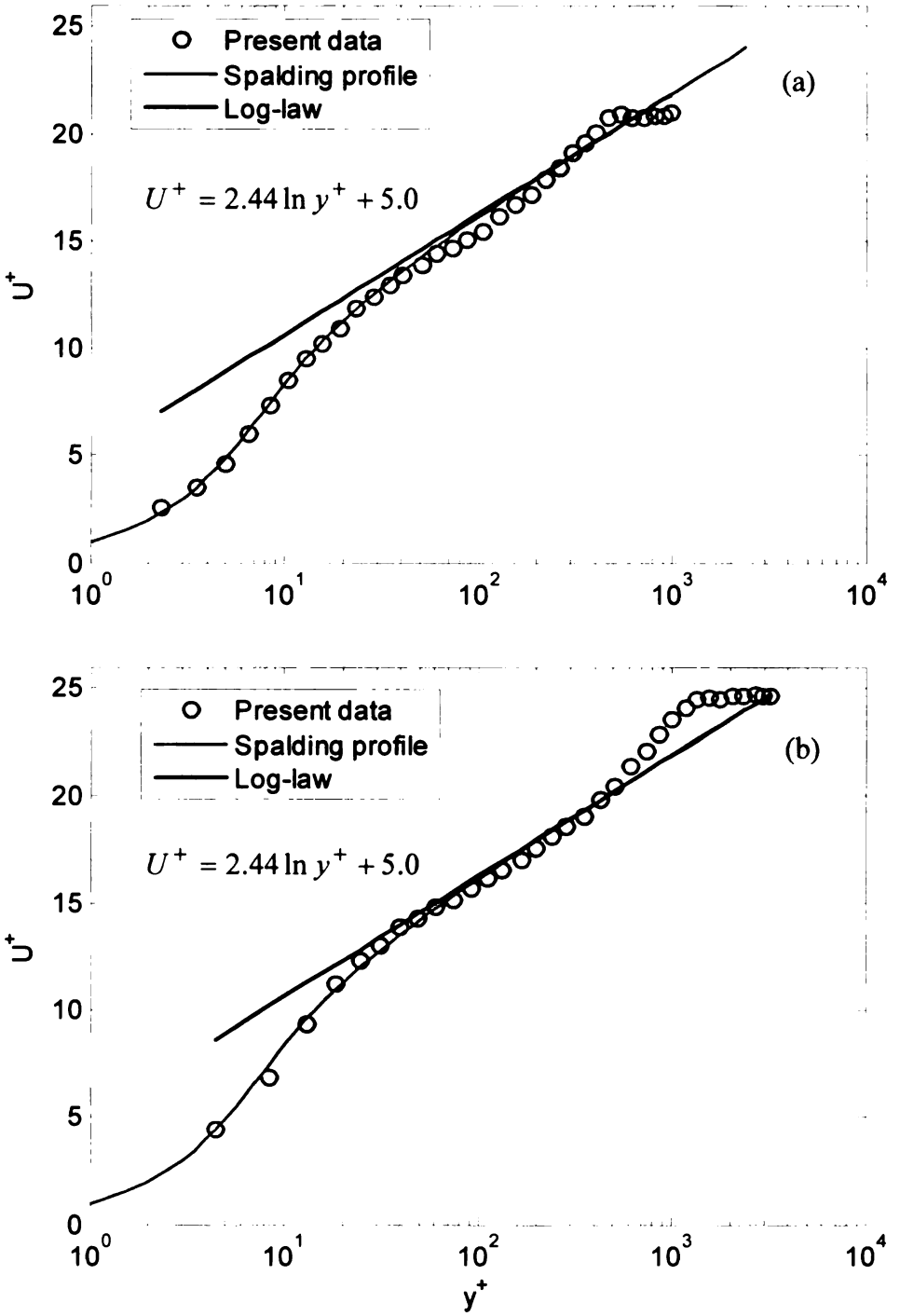

Figure 2.18 Boundary layer mean-streamwise-velocity profile for (a) U_∞ = 5 m/s and (b) U_∞ = 20 m/s

The friction velocity was determined to be 0.23 and 0.80 m/s for the free-stream velocity of 5 m/s and 20 m/s respectively. The red line in Figure 2.18 represents the

Spalding profile, and the black solid line shows the well known "log law". At the lower free-stream velocity the data undershoot the log law. This could indicate that although the boundary layer is turbulent, the Reynolds number may not be sufficiently high for the boundary layer to develop a proper log region. At the higher free-stream velocity, coincidence between the log law and the measured data is seen between $50<y^+<300$. Above $y^+ \approx 300$, the measured velocity profile overshoots the log law, consistent with the known behavior of "the wake region" in a turbulent boundary layer. Overall, the results indicate that the boundary layer at separation is turbulent at 5 m/s and 20 m/s. Similar boundary layer characteristics are also found at the other free-stream velocities (10 and 15 m/s). The corresponding momentum thickness is 5.49 mm, 4.03 mm 3.54 mm and 3.29 mm in order of increasing velocity. The shape factor of the boundary layer defined as the ratio between the displacement and momentum thickness, $H = \delta^*/\theta$ is about 1.35. For reference, the shape factor is 2.6 for a laminar zero-pressure-gradient boundary layer (Blasius profile) and is 1.3 for a zero-pressure-gradient turbulent boundary profile with momentum-thickness Reynolds number of 8000 (see Pope[15]).

2.3.3 Microphone Array Measurements

Two main explorations are performed using the microphone arrays: one to study the effect of cavity width on the self-sustained oscillation and the other to examine the characteristics of the oscillation along the azimuthal direction of the cavity. In the former, the unsteady-wall-pressure measurement beneath the central plane of the cavity is conducted for L/D = 2.6, 3.3 and 4.1, and W/D = 2.5, 3.7, 7.4 and "*NW*" (no-side-wall, or axisymmetric) using the streamwise microphone array at four different free-stream velocities (5, 10, 15 and 20 m/s), resulting in a corresponding Re = 4067, 8133, 12200

and 16267, respectively. For the second study, the unsteady wall pressure on the downstream cavity wall (at y/D = 0.5) is acquired for cavities with W/D of 2.5, 3.7, 7.4 and NW and L/D = 3.3 at a free-stream velocity of 15 m/s. All data are acquired at a sampling frequency of 2000 Hz, resulting in a Nyquist frequency of 1000 Hz, which is sufficiently higher than the highest frequency of interest (approximately 300 Hz). The absence of frequency aliasing is checked by comparing the resulting pressure spectra to those produced from acquisition at a higher sampling frequency. 262144 numbers of samples are acquired for about 131 seconds. More than 6000 cycles of the main oscillation frequency (between 50 Hz to 100 Hz) are contained in such time series.

When the unsteady wall pressure is acquired simultaneously with the LDA, longer acquisition time is required because the LDA has a substantially lower data rate. In this case, the wall-pressure sampling frequency is lowered to 1000 Hz to reduce the size of the resulting data files. The Nyquist frequency in this situation is 500 Hz, which remains higher than the highest frequency of interest.

2.3.4 LDA Measurements

Two-component velocity data are acquired over x-y planes at different azimuthal locations using the LDA system simultaneously with the unsteady wall pressure. For reasons that will become clear in Chapter 3, these measurements are conducted only for one aspect ratio of L/D = 3.3 and W/D = 7.4 over x-y planes at different azimuthal locations. To accomplish this, the LDA probe volume must be movable along the cavity perimeter. There are two drawbacks of doing so: 1) attaining a probe volume movement that is concentric with the axisymmetric model axis, though doable, is not easy; 2) measurements in azimuthal planes other than at $\phi = 0^\circ$ (see definition of in ϕ Figure 2.6)

don't benefit from the existence of the streamwise array beneath the measurements. Therefore, during the velocity measurements the focal point of the LDA is maintained within the plane on top of the model (ϕ = 0°) while the insert for *W/D* control is rotated around the central shaft (see Figure 2.3). Thus the azimuthal location of the LDA measurement plane relative to the symmetry plane of the cavity ($\Delta\phi$) can be varied.

To accomplish the above, one must ensure that the characteristics of the pressure fluctuations in a given azimuthal plane depend *only* on the offset angle relative to the cavity symmetry plane ($\Delta\phi$) *regardless* of the azimuthal location of the symmetry plane relative to the top of the model (ϕ_c): see Figure 2.19 for definition of $\Delta\phi$ and ϕ_c. That is, the wall-pressure fluctuation, and hence its generating flow structures, in a plane with a given azimuthal offset relative to the symmetry plane are not changed when the cavity is rotated around the central shaft. This is verified using pressure measurements as discussed in Appendix 6.4.

LDA measurements are performed in *x-y* planes at $\Delta\phi$ = 0° (the azimuthal symmetry plane), -24°, -28°, -32°, -36° and -40°. The latter five planes are selected in the vicinity of the azimuthal location where strong harmonic oscillations are found. Figure 2.20 shows the LDA measurement grid using red "+" symbols. The grid extends from 1.2 mm to 16.2 mm above the cavity bottom in increment of 1mm in the *y* direction, and from 2.9 mm downstream of separation to 4 mm ahead of the downstream cavity wall in increment of 2.4 mm in the streamwise direction. The blue circles in Figure 2.20 mark the locations of the microphones, the signals of which are sampled simultaneously with the LDA.

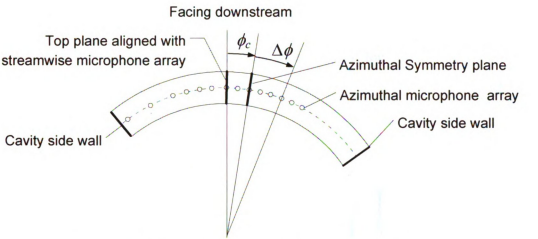

Figure 2.19 Illustration of the definition of $\Delta\phi$ and ϕ_c

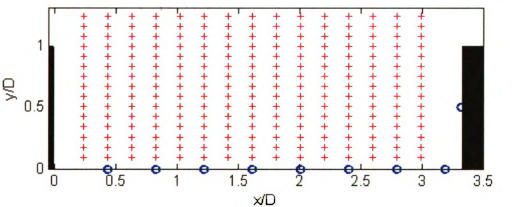

Figure 2.20 LDA measurement grid

The time of acquisition of LDA samples depends on the arrival time of seeding particles which is random. For the present measurements, the mean data rate varies between 1 Hz to 200 Hz depending on the location of the measurement. It is significant to note that in general the LDA data are not coincident in time with the pressure samples. Hence, in the data processing, the wall-pressure data, which have a substantially higher sampling frequency, are linearly interpolated using samples immediately preceding and following the arrival time of the LDA samples. This process is illustrated in Figure 2.21, in which the black squares represent the pressure samples interpolated from the raw data

(the blue circles) at the same arrival time as the velocity samples, shown by the red diamonds. The resulting simultaneous wall-pressure and velocity data allow computation of pressure-velocity correlations and stochastic estimation of the velocity field based on the unsteady wall pressure (see Chapter 4 for details).

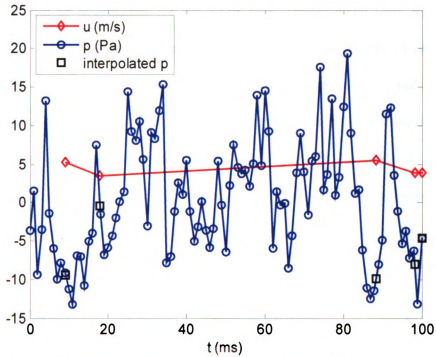

Figure 2.21 Illustration of the pressure interpolation process

LDA measurements tend to have more samples of high than of low velocity. Specifically, a larger number of particles will be swept through the measuring volume during a high velocity period. As a result, the computation of statistics based on arithmetic averaging has a bias towards higher velocity. To correct this bias, a weighting factor (see Adrian[7]) based on the transit time, t_i, of the particle in crossing the measurement volume is introduced in the calculation of the statistics. More specifically, the average of any variable, g, subjected to the weighting factor is:

$$\bar{g} = \frac{\sum_i g_i t_i}{\sum_i t_i}, \qquad \textbf{2.6}$$

where g_i is, for example, a velocity sample if calculating the mean velocity or product of two variables if computing second-order statistics.

In addition to accounting for the LDA bias, convergence tests were done for determining the number of samples and associated random uncertainty in calculating the mean and rms velocity and cross-correlation between the velocity and the pressure fluctuation. Figure 2.22 shows an example of the convergence test for the mean velocity ($\bar{u}$: plot a) and pressure-velocity correlation ($R_{u'p'}$: plot b). The abscissa displays the number of samples involved in averaging and the ordinate shows the corresponding value of the statistical quantity. Different colors represent data records acquired at different times. The black dashed lines in Figure 2.22(a) represent the region of $\pm 5\%$ deviation from the converged value and those in Figure 2.22(b) represent the region of $\pm 10\%$ deviation. Figure 2.22(a) shows that more than 400 data points are required to attain better than 5% convergence uncertainty for the mean velocity. On the other hand, Figure 2.22(b) indicates that at least 10000 points are needed for the velocity-pressure cross correlation to have an uncertainty of better than 10%. Hence, 10,000 velocity samples are acquired in all five azimuthal planes ($\Delta\phi$ = 0°, -24°, -28°, -32° and -36°). This results in uncertainty for the mean of less than 0.3% of the free stream velocity, for the rms velocity of less than 1% of the maximum value, and for the velocity-pressure correlation of less than 7% of the maximum value. In the azimuthal plane close to the cavity side wall ($\Delta\phi$ = -40°), because of the low data rate (around 1-5 Hz), only 2000 samples are

collected to guarantee the convergence of the mean velocity. No velocity-pressure correlation is obtained for this plane.

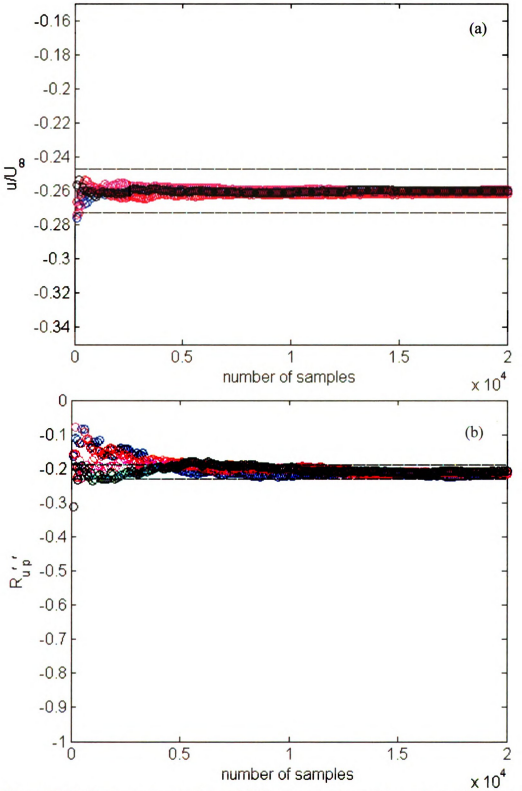

Figure 2.22 Convergence test for: (a) the mean streamwise velocity (b) cross-correlation between the velocity and the pressure fluctuations normalized by the velocity and pressure rms values

2.4. References

[1] Li, Y.X., "Investigation of the Wall-Shear-Stress Signature in a Backward-Facing-Step Flow Using Oscillation Hot-Wire Sensors," Ph.D. thesis, pp 20-32 (2004)

[2] Hudy, L.M., "Simultaneous Wall-Pressure and Velocity Measurements in the Flow Field Downstream of an Axisymmetric Backward-Facing Step," Ph.D. thesis, (2005)

[3] Trosin, B.J., "Velocity-Field Measurements of an Axisymmetric Separated Flow Subjected to Amplitude-Modulated Excitation," Master thesis, pp 12-15 (2006)

[4] Aditijandra, A.K., "Amplotude-Modulated Excitation of a Separated Flow Using an Externally Driven Helmholtz Resonator," Master thesis, pp 19-22 (2006)

[5] Kinsler, L.E., Frey, A.R., Coppen, A.R. AND Sanders, J.V., "Fundamentals of Acoustics," 3rd edition, John Wiley and Sons, New York (1982)

[6] Naguib, A.M., Gravante, S.P., and Wark, C.E., "Extraction of Turbulent Wall-pressure Time-series Using an Optimal Filtering Scheme," *Experiments in Fluids* **22** (1), pp. 14-22 (1996)

[7] Adrian, J.R., "Fluid Mechanics Measurements, Chapter 5: Laser Velocimetry," Taylor & Francis, Bristol, pp. 157-159 (1983)

[8] Gharib, M., Roshko, A.F., "The Effect of Flow Oscillations on Cavity Drag," *Journal of Fluid Mechanics* **177**, pp. 501-530 (1987)

[9] Najm, H.N., Ghoniem, A.F., "Numerical Simulation of the Convective Instability in a Dump Combustor," *AIAA Journal* **29** (6), pp. 911-919 (1991)

[10] Rowley, C.W., Colonius, T. and Basu, A.J., "On Self-sustained Oscillations in Two-dimensional Compressible Flow over Rectanguler Cavities", *Journal of Fluid Mechanisc* **455**, pp. 315-346 (2002)

[11] Maull, D.J., and East, L.F., "Three-dimensional Flow in Cavities," *Journal of Fluid Mechanics* **16**, pp. 620 - 632 (1963)

[12] Morris, S.C., and Foss, J.F., "Turbulent Boundary Layer to Single-stream Shear Layer: the Transition Region," *Journal of Fluid Mechanics* **494**, pp. 187-221, (2003)

[13] Spalding, D.B., "A single Formula for the Law of the Wall," *Journal of Applied Mechanics* **28**, pp. 455-457 (1961)

[14] Kendall, A. and Koochesfahani, M., "A Method for Estimating Wall Friction in Turbulent Wall-Bounded Flows," *Experiments in Fluids* **44**, pp. 773-780 (2008)

[15] Pope, S.B., "Turbulent Flows," Cambridge University Press, Cambridge, pp. 303 (2000)

3. WALL-PRESSURE-MEASURMENTS RESULTS

In this chapter, the unsteady pressure on the bottom and downstream wall of cavities with different aspect ratios will be discussed with an emphasis on the effect of the cavity width on the pressure signature. The discussion will focus on cavities with *L/D* = 2.6, 3.3 and 4.1 and *W/D* = 2.5, 3.7, 7.4 and "*NW*" (no-side-wall, or axisymmetric) at four different freestream velocities (5, 10, 15 and 20 m/s), corresponding to $Re = U_\infty D/\nu$ = 4067, 8133, 12200 and 16267, respectively.

3.1 Unsteady Wall Pressure in the Cavity Symmetry Plane

Most of the literature on cavity flow is based on the assumption that the flow is two dimensional. Experimental studies usually use cavities covering the whole span of the tunnel and focus only on the symmetry plane in the spanwise direction. Therefore, *as a starting point*, the exploration of the unsteady wall pressure here will be focused on comparing the wall-pressure unsteadiness in the axisymmetric cavity with that in the symmetry plane of cavities with side walls. The aim of the comparison is to explore the effect of cavity width and side walls on the unsteady wall pressure using the streamwise microphone array.

3.1.1 The Unsteady Wall Pressure in the Axisymmetric Cavity Flow

Figure 3.1 shows the streamwise distribution of the root-mean-square (rms) of the fluctuating pressure on the bottom of the axisymmetric cavity with *L/D* of 3.3 at different Reynolds numbers. The normalized rms value ($p'_{rms}/1/2\rho U_\infty^2$) is plotted as function of the streamwise distance from the cavity upstream wall normalized by the cavity length,

x/L. The rms represents the strength of the pressure fluctuations. The plot indicates that the wall-pressure unsteadiness increases along the streamwise direction of the cavity. The largest rms value is found nearest to the downstream corner and this value appears to decrease as the Reynolds number increases. Hudy[1] found a similar trend in the wall-pressure fluctuation downstream of a backward facing step. The reason for the decrease in the rms level with increasing Reynolds number is not clear.

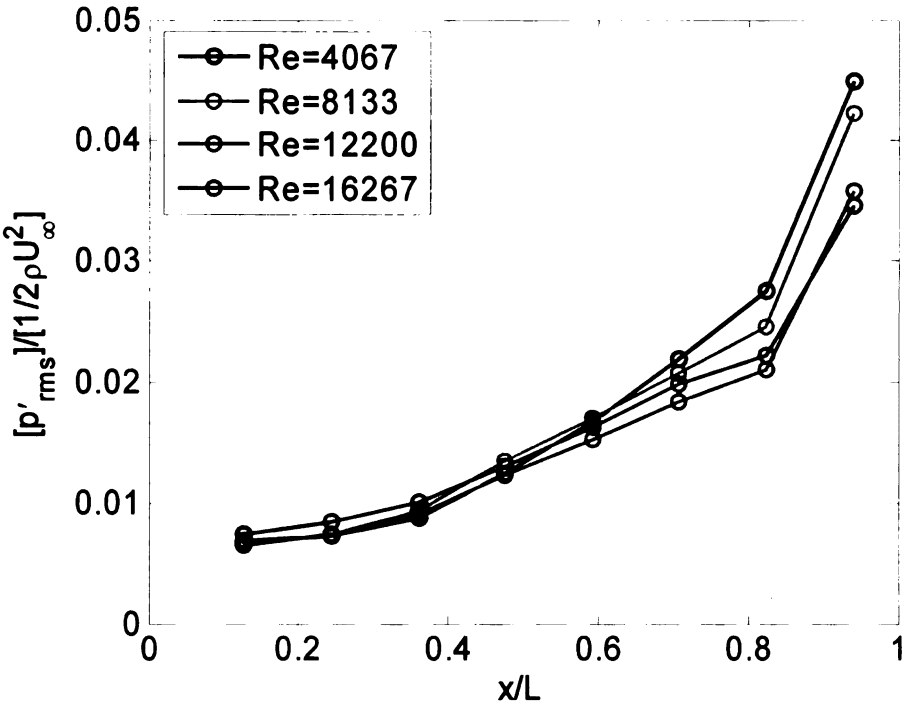

Figure 3.1 Streamwise distribution of the rms pressure acting on the bottom of the axisymmetric cavity for *L/D* = 3.3 and different Reynolds numbers

The frequency spectra $\phi_{p'p'}(f) = \langle P(f)^* \cdot P(f) \rangle$ provide information concerning the distribution of the energy of the pressure fluctuations over different frequencies *f*; where $\langle\ \rangle$ denotes the average over different records, *P(f)* is the Fourier transform of the pressure fluctuation signal *p'(t)*, and *P(f)** is the conjugate of *P(f)*. 1024

records of data with 256 samples in each record are used in calculating the spectra resulting in a frequency resolution of 7.8 Hz and random uncertainty of 3.1%. Figure 3.2 provides a plot of the frequency spectra of the unsteady wall pressure on the bottom of the axisymmetric cavity for L/D = 3.3 and Re =12200. The magnitude of the spectra normalized by the dynamic pressure of the free stream is plotted as function of the normalized frequency fL/U_∞. Lines with different colors represent different streamwise locations.

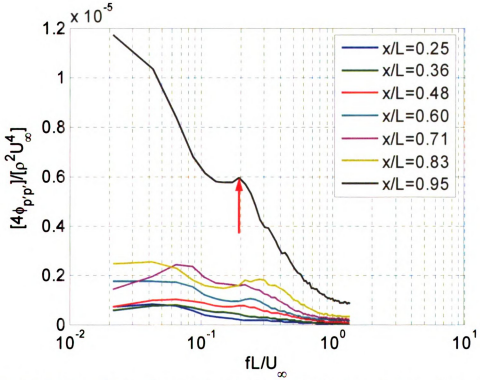

Figure 3.2 Wall-pressure frequency spectra on the bottom of the axisymmetric cavity for L/D = 3.3 and Re =12200. Lines with different colors represent different streamwise locations

Inspection of Figure 3.2 shows that no strong harmonic peaks are found in the spectra at all measurement locations. A small "bump" (pointed-to by an arrow in the figure) at $fL/U_\infty \approx 0.19$ is seen at x/L = 0.95 where the fluctuations are strongest. The lack of strong harmonic spectral peaks suggests that no strong self-sustained oscillations exist

in the present axisymmetric cavity flow. Overall, the spectra are broadband with their largest magnitude found at low frequencies. Even though disturbances at low frequencies seem dominant at $x/L = 0.95$, 80% of the fluctuation energy is contained in the frequency region of $fL/U_\infty > 0.1$.

The spectra for the same cavity geometry as above but at the lowest Reynolds number examined here ($Re = 4067$) are shown in Figure 3.3. As seen from the figure, the spectra remain broadband, although they exhibit a preferred peak at a frequency of $fL/U_\infty \approx 0.25$ at $x/L = 0.95$. Another interesting observation regarding the lower Reynolds number case, is the absence of the strong low-frequency unsteadiness found at $Re = 12200$. The dependence of the low-frequency fluctuations on the Reynolds number suggests that this unsteadiness might be related to some form of instability. This will be discussed later.

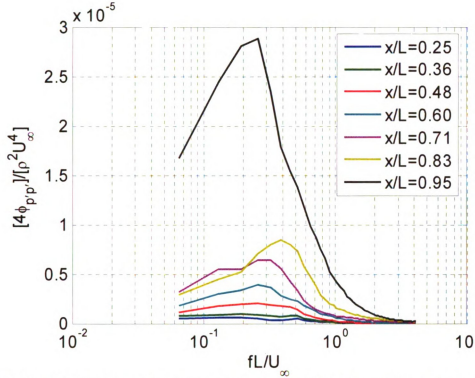

Figure 3.3 Wall-pressure frequency spectra on the bottom of the axisymmetric cavity for *L/D* = 3.3 and *Re* =4067. Lines with different colors represent different streamwise locations

Wall-pressure measurements in axisymmetric cavities with *L/D* of 2.6 and 4.1 also do not show any evidence of existence of strong self-sustained oscillations. The spectra of the unsteady wall pressure at $x/L = 0.95$ are shown in Figure 3.4 for all aspect ratios investigated. No harmonic peak is found in the spectra; although curiously all cases exhibit the non-prominent peak at $fL/U_\infty \approx 0.19$ (within ± 0.02, which is the spectrum resolution). Please note here, 80% of the fluctuation energy is contained in the frequency region of $fL/U_\infty > 0.1$ even though disturbances at the low frequency end are strong. In addition, the spectra for different *L/D* values are similar, which suggests that the pressure fluctuation is dominated by similar flow structures for all aspect ratios investigated. Also, spectra results for other Reynolds numbers show similar characteristics as found in

Figure 3.4; i.e. showing no prominent self-sustained oscillations in the axisymmetric cavities studied here.

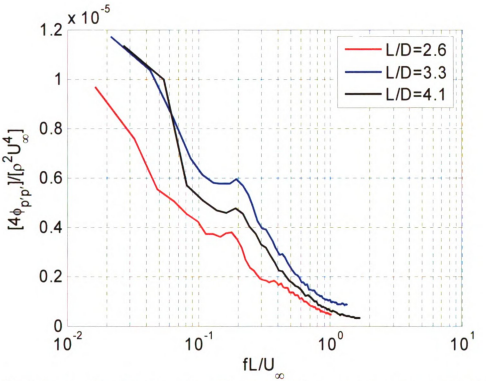

Figure 3.4 Aspect ratio effect on the wall-pressure frequency spectra on the bottom of the axisymmetric cavity at $x/L = 0.95$ and $Re = 12200$. Lines with different colors represent cavities with different L/D

It is interesting to note that the frequency of the non-prominent peak at $fL/U_\infty \approx 0.19 \pm 0.02$ when normalized by the cavity depth ($fD/U_\infty = 0.07$, 0.06 and 0.05 for $L/D =$ 2.6, 3.3 and 4.1 respectively) is close to the normalized frequency of the wake mode in Rowley *et al.*[2] ($fD/U_\infty = 0.06$ and 0.05 for $L/D = 4$ and 5 respectively). In their simulation of cavity flow with a laminar boundary layer at separation, the wake mode is found to exist for cases with $L/\theta > 75$. L/θ in this study varies between 5.6 and 15.2. However, the boundary layer at separation is turbulent. Morris and Foss[3] showed that only the near-wall, or inner-layer, vorticity participated in the initial shear layer instability in the case

of turbulent-flow separation. An "effective momentum thickness" of $\theta_{eff}/(\upsilon/u_\tau) \approx 10$ is found (based on their results: $\theta_{eff} = 0.5$mm, $U_0 = 7.1$m/s, $C_f = 2(u_\tau/U_0)^2 = 0.00295$) to be the appropriate length scale characterizing turbulent separation rather than θ. Based on this result, $128 \leq L/\theta_{eff} \leq 210$ for $Re = 12200$, which falls in the region of wake-mode oscillation found by Rowley *et al.* Therefore, it is suspected that the broad peak at $fL/U_\infty \approx 0.19 \pm 0.01$ in the axisymmetric cavity corresponds to a wake mode. The wall-pressure signature of this mode produces a spectral peak that is easily seen in the low Reynolds number case and is embedded in broadband turbulence in the high Reynolds number case. This finding is supported by the stochastic estimation results in Chapter 4.

3.1.2 Effect of Cavity Width on the Unsteady Wall Pressure in the Symmetry Plane

As discussed above, except for the possibility of a wake mode that is non-prominent at high Reynolds number, no strong self-sustained oscillations are found in the axisymmetric cavity with $L/D = 2.6$, 3.3 and 4.1 at different Reynolds numbers. To investigate if this observation depends on the cavity width, measurements are first performed for the cavity with L/D of 3.3 and different widths. The specific W/D values are 2.5, 3.7, and 7.4. For each of these cases, the unsteady pressure on the floor in the symmetry plane is investigated at $Re = 4067$ and 12200.

3.1.2.1 Frequency Spectra

Figure 3.5 shows the frequency spectra of the unsteady pressure measured in the symmetry plane near the downstream wall ($x/L = 0.95$) on the cavity floor at $Re = 12200$ for different values of W/D. There is a striking change in the nature of the cavity oscillation as the cavity becomes narrower. For the narrower cavities ($W/D = 2.5$ and 3.7),

a strong harmonic peak is observed at $fL/U_\infty \approx 0.21$, suggesting the possible establishment of self-sustained oscillations. On the other hand, there is no evidence of such oscillations in the spectra for the wider cavities ($W/D = 7.4$ and *NW*) *and* instead the strongest unsteadiness is found at low frequency.

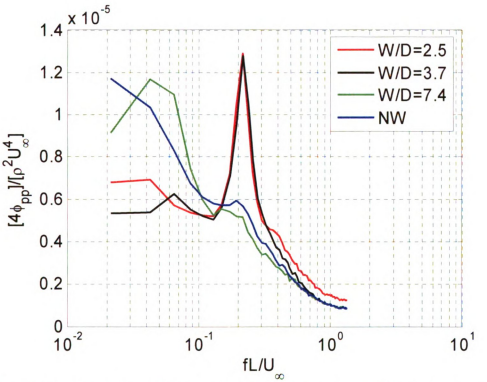

Figure 3.5 Cavity-width effect on wall-pressure spectra at $x/L = 0.95$ ($Re = 12200$). Lines with different colors represent cavities with different width

The frequency of the harmonic oscillation ($fL/U_\infty \approx 0.21$) is substantially lower than the typical value for the lowest Rossiter mode ($fL/U_\infty \approx 0.4$ to 0.5). This suggests that the self-sustained oscillation observed here is not of the Rossiter type. Interestingly, however, the harmonic peak occurs at practically the same frequency where it is believed that a non-prominent wake mode exists in the axisymmetric cavity. This could imply that the strong harmonic oscillation found in the narrow cavities maybe caused by "intensification" of the naturally existing wake mode in the wider cavities. This idea will

be explored in the following chapter, where the mechanism leading to the establishment of the harmonic oscillation is investigated using the simultaneous wall-pressure and velocity measurements.

The suppression of the self-sustained oscillation in the wider cavities is also observed for other Reynolds numbers, but the effect of the cavity width seems to decrease as the Reynolds number is reduced. This can be seen by comparing the results shown in Figures 3.6 through 3.8 for Re = 16267, 8133 and 4067 respectively. The spectra in Figure 3.6 for Re = 16267 show a distinguished difference between the narrow and wide cavities, similar to that observed in Figure 3.5 for Re = 12200. That is, a harmonic peak at $fL/U_\infty \approx 0.21$ for W/D = 2.5 and 3.7 and the attenuation of this peak accompanied by the strong low-frequency unsteadiness for W/D = 7.4 and NW. For Re = 4067, the spectra shown in Figure 3.8, the harmonic peak at $fL/U_\infty \approx 0.26$ is not as pronounced as in the higher-Reynolds-number case, but it remains discernable for the narrower cavities. The peak gets weaker with increasing cavity width, but the attenuation is not as strong as in the higher-Reynolds-number case, *and* the strongest unsteadiness never switches to low frequencies.

Also noteworthy is the effect of the Reynolds number on the wake mode prominence for the axisymmetric cavity. The results in Figures 3.5 through 3.8 clearly show how the spectral peak associated with this mode is prominent at the lowest Reynolds number, but gradually becomes less observable with increasing Reynolds number, accompanied by concurrent increase in the low-frequency broadband fluctuations.

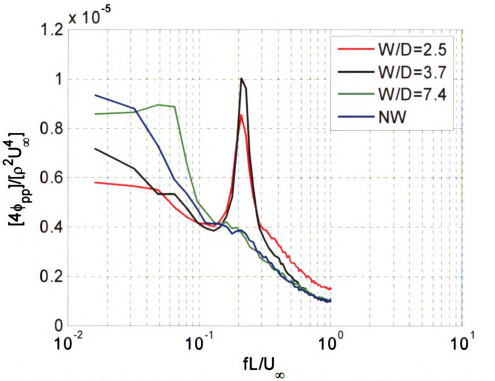

Figure 3.6 Cavity-width effect on wall-pressure spectra at $x/L = 0.95$ for $Re = 16267$. Lines with different colors represent cavities with different width

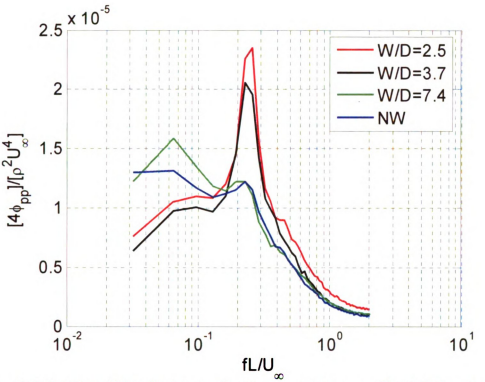

Figure 3.7 Cavity-width effect on wall-pressure spectra at x/L = 0.95 for Re = 8133. Lines with different colors represent cavities with different width

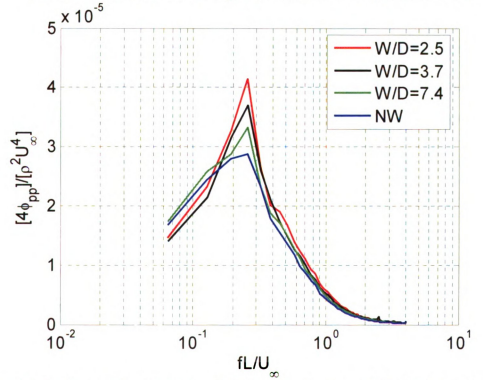

Figure 3.8 Cavity-width effect on wall-pressure spectra at x/L = 0.95 for Re = 4067. Lines with different colors represent cavities with different width

The increase in the strength of the low-frequency unsteadiness with Reynolds number leads us to believe that this unsteadiness could be related to some form of instability. As discussed in the introduction, Bres and Colonius[4] discovered that a three-dimensional centrifugal instability of the *two-dimensional* re-circulating flow inside a cavity "kicks in" above a critical Reynolds number. Furthermore, the frequency of this instability was found to be much smaller than that of the self-sustained cavity oscillations. These characteristics agree with the present observations, where the rise in the spectra at the low-frequency end for the wide cavities is only found at the higher Reynolds number and at frequencies that are substantially lower than that of the harmonic oscillations (see Figure 3.5, 3.6 and 3.7). Thus, it is possible that the low-frequency disturbances observed here are caused by the three-dimensional instability of the flow inside the cavity.

Frequency spectra similar to those shown in Figure 3.5 but for L/D values other than 3.3 in the range $L/D < 5$ show that the observed cavity-width effect is not specific to $L/D = 3.3$. Figure 3.9 gives the frequency spectra of the unsteady wall pressure near the downstream corner at $Re = 12200$ for cavities with $L/D = 2.6$ and 4.1, and $W/D = 2.4$, 3.5 and 7.1 and NW. Similar to Figure 3.5, the spectra in Figure 3.9 for narrow cavities are characterized by a clear harmonic peak which suggests the establishment of cavity oscillation. The spectral peak, however, is highly damped as the cavity becomes wider. An interesting observation is that for the cavity with $L/D = 2.6$, the harmonic oscillation is weakened for $W/D = 3.7$ and wider cavities (Figure 3.11a). In contrast, for cavities with $L/D = 3.3$ and 4.1, the oscillation can be sustained for $W/D = 3.7$. Table 3.1 compares the cavity aspect ratio L/D and W/D for oscillating (bold) and non-oscillating flow conditions in the symmetry plane. Noting that in all cases strong oscillations are observed in the

symmetry plane when *W/L* is approximately less than or equal to one, it is apparent that the ratio between the cavity width and length, *W/L*, is a significant parameter to include in setting criteria for the establishment of the observed harmonic oscillations in the symmetry plane of the cavity. This conclusion will be re-examined and refined in light of section 3.2 results.

Table 3.1 Cavity width-to-length ratio for oscillating (bold) and non-oscillating flow in the symmetry plane

	W/D=2.5	*W/D*=3.7	*W/D*=7.4	*NW*
L/D=2.6	***W/L*=0.96**	*W/L*=1.42	*W/L*=2.85	*NA*
L/D=3.3	***W/L*=0.76**	***W/L*=1.12**	*W/L*=2.24	*NA*
L/D=4.1	***W/L*=0.61**	***W/L*=0.90**	*W/L*=1.80	*NA*

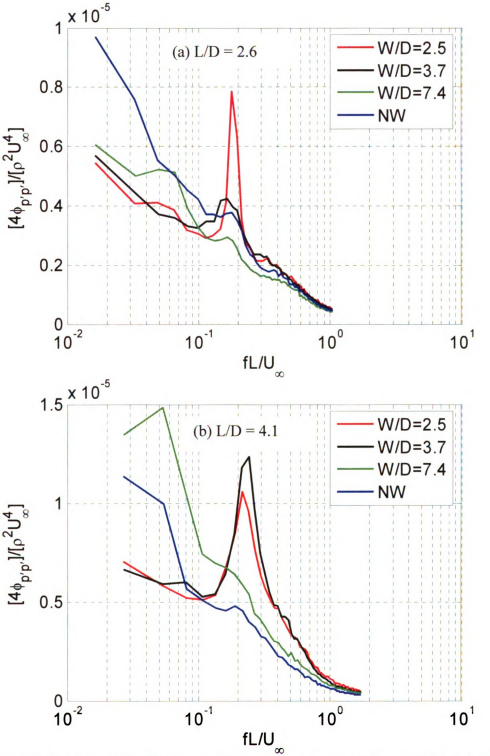

Figure 3.9 Cavity-width effect on wall-pressure spectra at *Re* = 12200: (a) *L/D* =2.6 (b) *L/D* = 4.1. Lines with different colors represent cavities with different width

Since cavities with different *L/D* exhibit the same width influences, subsequent results will be focused only on cavities with *L/D* = 3.3 in order to further explore the characteristics of the harmonic oscillation and the effect of the cavity width on the mechanism driving the oscillation.

3.1.2.2 Coherence

The harmonic oscillations found in the narrower cavities exhibit a large degree of phase locking across the entire cavity length. This can be seen from the contour plot of the coherence between the wall-pressure fluctuations measured near the cavity downstream edge and those at different locations on the cavity floor; shown in Figure 3.10 for a cavity with *L/D* = 3.3 and *W/D* = 2.5 at *Re* = 12200. The coherence, as defined by equation 3.1 below, gives a measure of the degree of phase locking between two signals at a given frequency:

$$C_{p'_1 p'_2}(f) = \frac{\left|\left\langle P_1(f)^* \cdot P_2(f) \right\rangle\right|}{\phi^{1/2}_{p'_1 p'_1}(f) \cdot \phi^{1/2}_{p'_2 p'_2}(f)} \quad , \qquad \textbf{3.1}$$

where $\langle\ \rangle$ denotes the average over different records, $P_1(f)$ and $P_2(f)$ are the Fourier transform of the signals $p'_1(t)$ and $p'_2(t)$ respectively. $P_1(f)^*$ is the conjugate of $P_1(f)$. 1024 records of data with 256 samples in each record are used in calculation resulting in a frequency resolution of 7.8 Hz and random uncertainty of 3.1%.

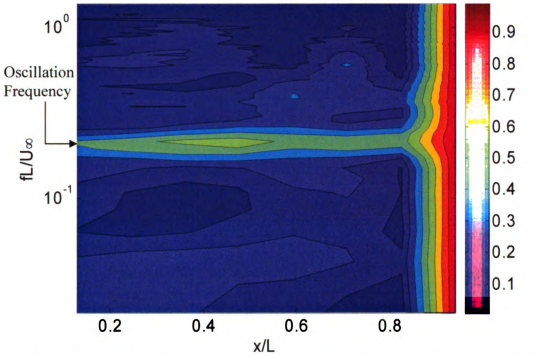

Figure 3.10 Coherence of pressure fluctuations across the cavity length relative to pressure measured at $x/L = 0.95$ for $W/D = 2.5$ at $Re = 12200$. The color bar on the right indicates the coherence value

The coherence value in Figure 3.10 is represented by the color bar displayed next to the coherence plot. As seen from the figure, substantial coherence magnitude is sustained across the length of the cavity at $fL/U_\infty \approx 0.21$. This confirms the global organization of the flow unsteadiness at this frequency and the establishment of self-sustained oscillation in the narrow cavity. On the other hand, no substantial coherence is found across the whole cavity length for the axsiymmetric case; shown in Figure 3.11.

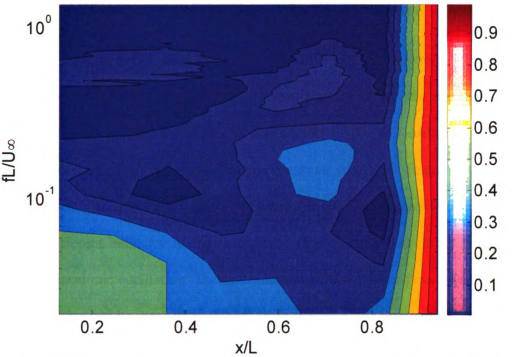

Figure 3.11 Coherence of pressure fluctuations across the cavity length relative to pressure measured at x/L = 0.95 for the axisymmetric cavity at Re = 12200. The color bar on the right indicates the coherence value

In summary, it is found here that the occurrence of strong harmonic oscillation in the symmetry plane depends on the cavity width, this width effect becomes more pronounced with increasing Reynolds number. At *high Re*, the cessation of the oscillation is accompanied by increased unsteadiness at very low frequencies. Also the observed oscillation is not of Rossiter type and it occurs at the same frequency where it is believed that a wake mode with non-prominent pressure signature exists in the axisymmetric cavity.

3.2 Azimuthal Distribution of the Unsteady Wall Pressure

Results from above show that the characteristics of the pressure signature in the symmetry plane of the wide cavity ($W/L > 1$; approximately) are the same as for the axisymmetric cavity, i.e. exhibiting strong attenuation of the self-sustained, harmonic oscillation accompanied by increased unsteadiness at very low frequencies at high Reynolds number. In contrast, narrow cavities ($W/L < 1$; approximately) exhibit dramatically different behavior in the symmetry plane, as reflected in the presence of self-sustained harmonic oscillation. To better understand the effect of cavity width on the cavity unsteadiness and its three-dimensional characteristics, the fluctuation wall pressure is measured using the azimuthal microphone array on the downstream cavity wall. All studies are done for a cavity with L/D of 3.3 and Re = 12200.

3.2.1 Cavities with Finite Width

The azimuthal microphone array, with 14 microphones covering 60° along the azimuthal direction, is used to explore the three-dimensional features of the oscillations in the finite width cavity. Figure 3.12 displays a flooded color-contour plot for the frequency spectra of the unsteady wall pressure on the downstream cavity wall at different azimuthal locations for the narrowest cavity (W/D = 2.5). The magnitude of the spectra normalized by the peak value is represented by the color bar on the right side of the figure. The spectra are plotted as a function of the frequency and the azimuthal location, z, which is defined as the arch length between the measurement location and the symmetry plane at a height of $D/2$ from the cavity bottom. Positive values of z show positions to the right of the symmetry plane when facing the cavity's end wall from upstream. The azimuthal location is normalized by the cavity depth.

The color contours in Figure 3.12 show variations along the azimuthal direction at the oscillation frequency, indicating the strength of the oscillation is not uniform along the span even for $W/D = 2.5$ (the narrowest cavity studied here). The oscillation is strong in the symmetry plane, $z/D = 0$ (indicated by the broken red line), and close to the cavity side walls (indicated by the dashed blue line for $z/D = 0.98$ near the right side wall); In between, at $z/D = 0.66$ (indicated by the dashed black line), the oscillation is suppressed. This can be seen more clearly in the line plots in Figure 3.13, which provides a comparison between the frequency spectra at these three different azimuthal locations. The results show that the observed oscillation in the narrowest cavity is three-dimensional: a finding that could not be made from examination of the streamwise array data only.

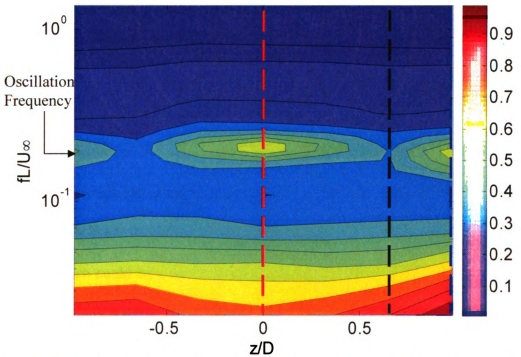

Figure 3.12 Flood color-contour map showing the azimuthal variation of the frequency spectra of the pressure acting on the end cavity wall for the cavity with $W/D = 2.5$. The Color bar on the right indicates the magnitude of the spectra normalized by the peak value

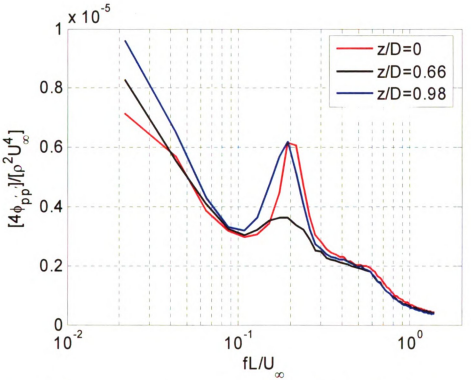

Figure 3.13 Frequency spectra at selected azimuthal locations for the cavity with W/D = 2.5. Lines with different colors represent different azimuthal locations

The spectral characteristics of the oscillation along the cavity span change when the cavity width is varied. This can be seen by comparing the spectra contour plot for W/D = 2.5 in Figure 3.12 with a similar plot for W/D = 3.7 in Figure 3.14. For this cavity width, the oscillation at $fL/U_\infty \approx 0.21$, detected earlier in the symmetry plane, shows a peak at z/D = 0.66 instead of at z/D = 0 as found in Figure 3.12 for W/D = 2.5. Moreover, disturbances at a lower frequency of $fL/U_\infty \approx 0.06$ seem to be strongest close to the cavity side walls, which could be a sub-harmonic of the oscillation at $fL/U_\infty \approx 0.21$ (to within the spectral resolution of $\Delta fL/U_\infty = 0.02$). Further details of the spectra may be seen using line plots in Figure 3.15 for the symmetry plane, and the azimuthal locations of the highest fluctuations at $fL/U_\infty \approx 0.21$ and 0.06. These locations are shown by broken lines in Figure 3.14.

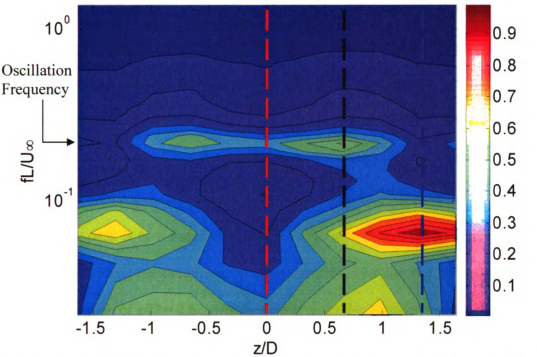

Figure 3.14 Flooded color-contour map showing the azimuthal variation of the frequency spectra of the pressure acting on the end cavity wall for the cavity with *W/D* = 3.7. The color bar on the right indicates the magnitude of the spectra normalized by the peak value

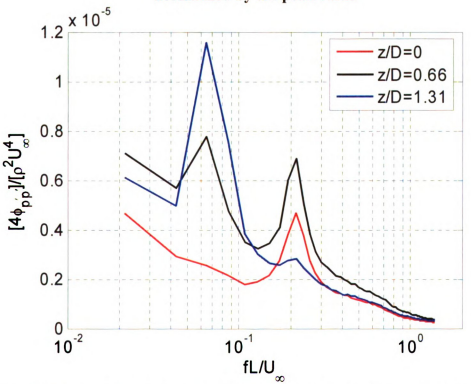

Figure 3.15 Frequency spectra at selected azimuthal locations for the cavity with *W/D* = 3.7. Lines with different colors represent different azimuthal locations

Because the contour plots in Figure 3.12 and 3.14 show that the spectra of the disturbances on opposite sides of the symmetry plane have similar features, the azimuthal microphone measurements for the wide cavity with $W/D = 7.4$ are conducted in only one half of the cavity. The spectra contour plot is shown in Figure 3.16. Given that examination of the streamwise-array results showed no harmonic oscillation at $fL/U_\infty \approx 0.21$ (Figure 3.6) in the symmetry plane of this wide cavity, it is somewhat surprising that such a harmonic peak is now found in Figure 3.16. That such a peak was not observed in the measurements using the streamwise array is caused by the fact that the peak occurs at an azimuthal location of $z/D = 2.62$, which is away from the symmetry plane. Also worth noting is that similar to what is observed for the cavity with $W/D = 3.7$, the unsteadiness at the lower frequency of $fL/U_\infty \approx 0.06$ is strong close to the side wall at $z/D = 3.28$. Figure 3.17 provides the frequency spectra of the wall-pressure fluctuations at $z/D = 0$ (symmetry plane), 2.62 (where the peak at $fL/U_\infty \approx 0.21$ is found) and 3.28 (where disturbances at $fL/U_\infty \approx 0.06$ are strong). The peak in the spectrum at $fL/U_\infty \approx 0.21$ at $z/D = 2.62$ suggests the existence of self-sustained oscillation. Note that most of the disturbances (80% of the total fluctuation energy) are contained in the frequency band $fL/U_\infty > 0.1$ even at the azimuthal locations where the magnitude of the spectra at the low-frequency end is highest.

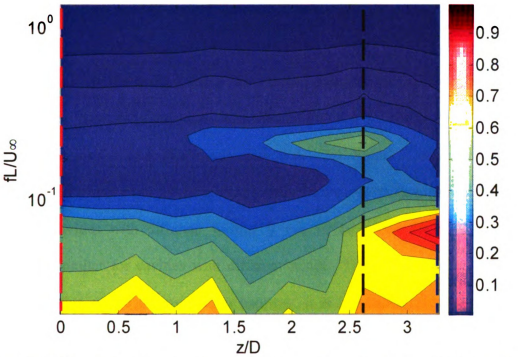

Figure 3.16 Flooded color-contour map showing the azimuthal variation of the frequency spectra of the pressure acting on the end cavity wall for the cavity with *W/D* = 7.4. The color bar on the right indicates the magnitude of the spectra normalized by the peak value

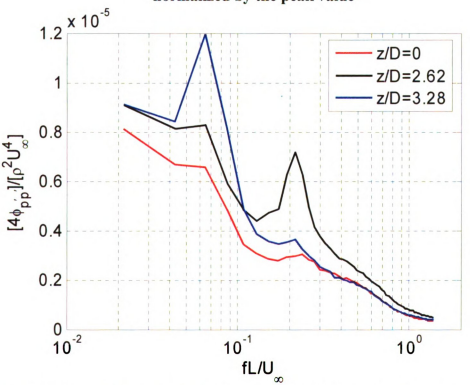

Figure 3.17 Frequency spectra at selected azimuthal locations for the cavity with *W/D* = 7.4. Lines with different colors represent different azimuthal locations

The above results indicate that there are strong harmonic pressure oscillations in all cavities having side walls; including the widest cavity with W/D = 7.4. It appears that these oscillations are generally located on the two sides of the cavity central plane. However, when the cavity becomes narrower, these two locations "merge" in the symmetry plane for the narrowest cavity with W/D =2.5. Figure 3.18 yields the wall-pressure frequency spectra at the azimuthal location where the peak in the oscillation is detected for cavities with different widths. It can be seen that the strength of the oscillations is similar for cavities with different widths. The primary difference is the azimuthal location where the oscillation happens. It is interesting to note that as the cavity width increases, the azimuthal distance between the peak-oscillation location and the cavity side wall, ΔW remains approximately invariant relative to the cavity depth: $\Delta W/D \approx$ 1.25, 1.1 and 1.1, for cavities with W/D = 2.5, 3.7 and 7.4 respectively. This, coupled with the fact that similar harmonic oscillations are absent at *all* azimuthal locations for the axisymmetric cavity (see the following section), leads us to suspect that the oscillation found here is related to the existence of the cavity side walls.

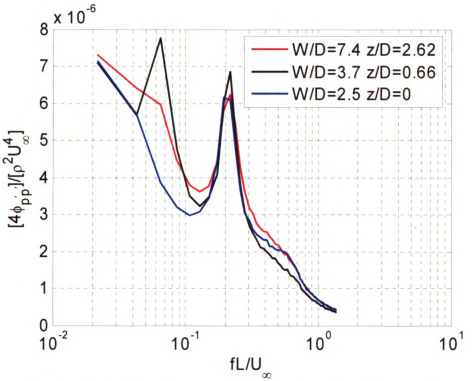

Figure 3.18 Frequency spectra at the azimuthal location of strongest harmonic oscillation for cavities with different *W/D* values. Lines with different colors represent cavities with different width

Another noteworthy feature of the harmonic oscillation can be seen from examination of the coherence between the pressure fluctuation at $fL/U_\infty \approx 0.21$ at different azimuthal locations and that at the location of peak oscillation. Figure 3.19 depicts the coherence value for the widest cavity (where the peak oscillation location is at $z/D = 2.62$). The figure indicates that even though high coherence is maintained over a relatively narrow zone around $z/D = 2.62$, non-zero coherence (approximately 20%) is found with disturbances at $fL/U_\infty \approx 0.21$ in the symmetry plane (corresponding to the small "bump" in the spectra in Figure 3.17). This suggests the flow structures near the side wall and the flow in the middle of the cavity are correlated.

Finally, it is noted here that even though the harmonic oscillation shows three-dimensional characteristics, it doesn't posses the azimuthally-periodic behavior of the centrifugal instability observed by Bres and Colonius[4]. This provides additional evidence that the observed oscillation is not caused by the 3-D instability of the re-circulating flow in the cavity.

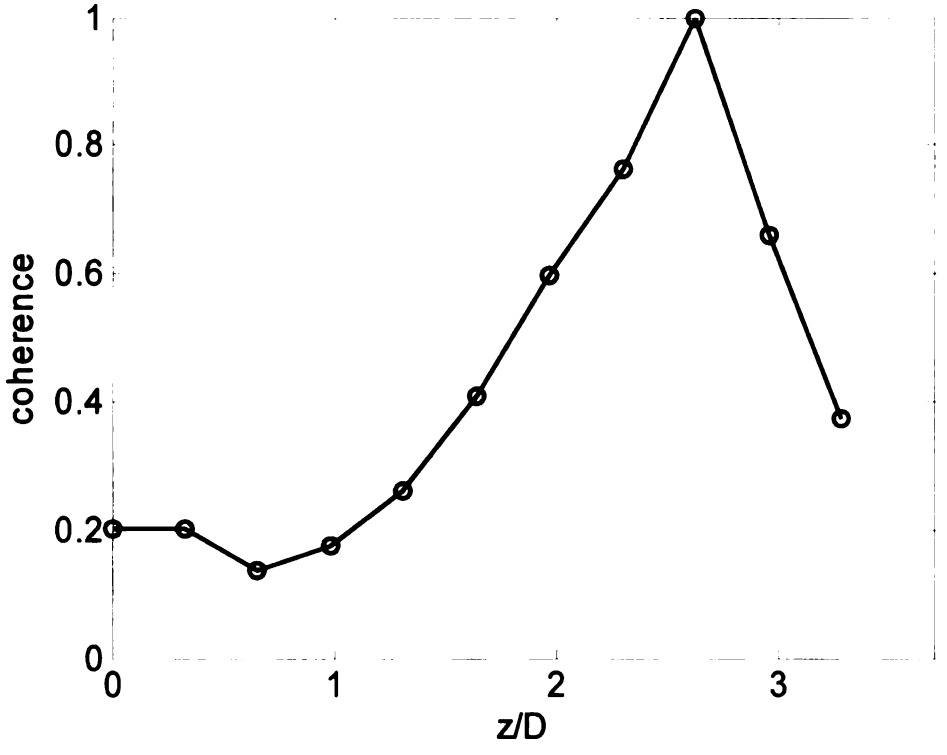

Figure 3.19 Coherence between the pressure fluctuations at different azimuthal locations with those at $z/D = 2.62$ for $W/D = 7.4$

3.2.2 Axisymmetric Cavity

The variation of the wall-pressure unsteadiness along the azimuthal direction for the axisymmetric cavity (*NW*) is investigated using the Panasonic azimuthal microphone array which covers the whole perimeter of the cavity. Figure 3.20 displays the distribution of the rms pressure along the azimuthal direction. The horizontal axis of the plot shows the azimuthal angle ϕ, as defined in Figure 2.6, between the measurement

location and the top plane where the streamwise microphone array is embedded. The rms pressure is seen to exhibit some variation along the azimuthal direction with a deviation of 7% (based on the standard deviation) from the mean value. There are two possible reasons for the observed variation: 1) the existence of three-dimensional features inside the cavity (as found, for example in the visualization study of Maull and East[5], or the instability analysis of Bres and Colonius[4]; 2) noting that the highest rms values are found around ϕ =180° (on the bottom side of the model), it is possible that there is some influence of the support of the model, which is located 0.61 m(more then 500 cavity depths) downstream of the separation point.

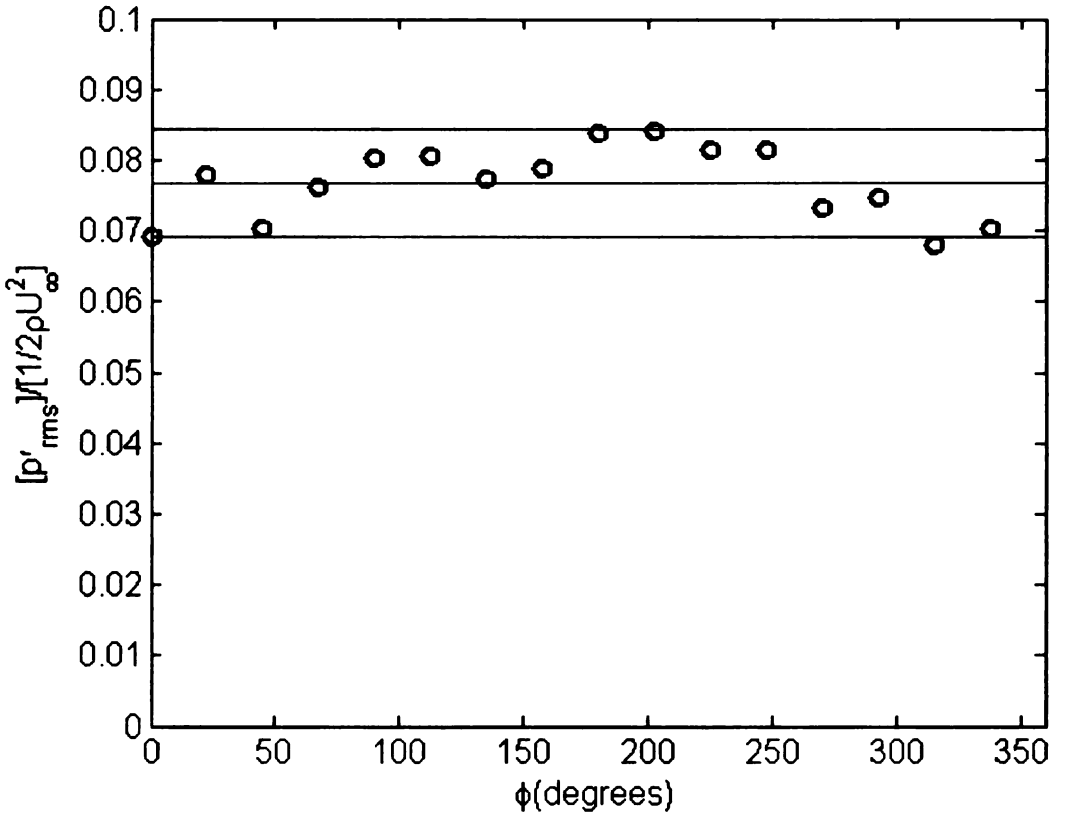

Figure 3.20 Azimuthal distribution of the rms pressure for the axisymmetric cavity with *L/D* = 3.3. Red line shows the average rms pressure and black lines represent 10% deviation from the mean value

Regardless of the cause of the azimuthal variation in the strength of the pressure fluctuations, the spectral shapes remain invariant. This can be seen from frequency spectra depicted in Figure 3.21 for different azimuthal locations (represented by lines with different colors). All spectra exhibit similar features with the strongest pressure fluctuations taking place at the low-frequency end of the spectrum. Most significant is the absence of any harmonic peak in the spectra for the axisymmetric cavity at *all* azimuthal locations. This reinforces the statements in the previous section that the harmonic oscillation observed in the finite-width cavity is related to the existence of the side walls. It is, however, significant to note that a local, broad peak is found in all spectra in the axisymmetric case (pointed to by an arrow in Figure 3.21) at the *same* frequency ($fL/U_\infty \approx 0.21$) as the self-sustained oscillation.

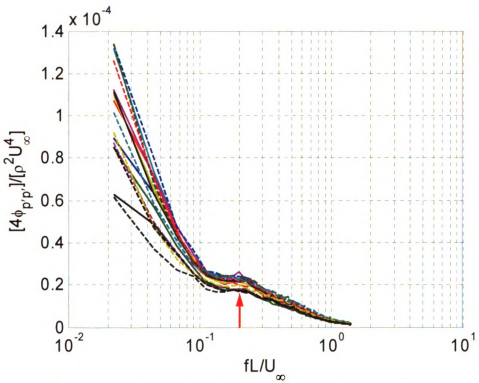

Figure 3.21 Frequency spectra at different azimuthal locations in the axisymmetric cavity. Black solid line shows spectrum at $\phi = 0°$; Remaining lines depict the spectra at angle increments of 22.5°

3.3 Summary

In conclusion, strong harmonic pressure oscillations are detected in cavities having side walls. These oscillations are generally located at a distance of the order of the cavity depth from the side walls. However, when the cavity becomes sufficiently narrower, such as the case for the narrowest cavity examined here (W/D =2.5), the oscillations on opposite sides of the centerline "merge" on the symmetry plane. The frequency of the harmonic oscillation is much lower than the lowest Rossiter mode, and close to the frequency of the wake mode found by Rowley *et al*[2]. No prominent oscillation exists in the axisymmetric cavity without side walls. This shows that the existence of a side-wall is essential for the establishment of the strong harmonic oscillation found here.

Interestingly, a local, non-prominent peak is found in the wall-pressure frequency spectra for the axisymmetric cavity at the *same* frequency as the self-sustained oscillation in finite-width cavities. At *high Re*, the cessation of strong oscillation in the axisymmetric cavity is accompanied by increased unsteadiness at very low frequencies. The characteristics of the pressure signature in the symmetry plane of the wide cavity are the same as for the axisymmetric cavity, i.e. exhibiting strong attenuation of the self-sustained oscillation accompanied by increased unsteadiness at very low frequencies at high Reynolds number.

Because of the three-dimensional nature of the harmonic oscillation found here and its relation to the cavity side wall, this type of cavity unsteadiness could not be identified in existing numerical simulations of cavity flows, which are based on infinitely wide geometry. Moreover, because the oscillation is confined close to the cavity side

walls, experimental studies focusing only on the symmetry plane and employing cavities with large width could not observe this oscillation either. However, since in practice all cavities are finite in width, the oscillation could be pronounced producing high level of noise and vibration of the geometry containing the cavity. In the following chapter, the mechanism leading to the establishment of this new mode of oscillation will be investigated using simultaneous velocity and wall-pressure measurements.

3.4 References

[1] Hudy, L.M., "Simultaneous Wall-Pressure and Velocity Measurements in the Flow Field Downstream of an Axisymmetric Backward-Facing Step," Ph.D. thesis, pp 64-67 (2005)

[2] Rowley, C.W., Colonius, T. and Basu, A.J., "On Self-sustained Oscillations in Two-dimensional Compressible Flow over Rectanguler Cavities", *Journal of Fluid Mechanics* **455**, pp. 315-346 (2002)

[3] Morris, S.C., and Foss, J.F., "Turbulent Boundary Layer to Single-stream Shear Layer: the Transition Region," Journal of Fluid Mechanics, Vol. 494, Nov. 2003, pp. 187-221.

[4] Bres, G.A., and Colonius, T., "Three-dimensional Instability in Compressible Flow over Open Cavities," *Journal of Fluid Mechanics* **599**, pp. 309-339, (2008)

[5] Maull, D.J., and East, L.F., "Three-dimensional Flow in Cavities," *Journal of Fluid Mechanics* **16**, pp. 620-632 (1963)

4. SIMULTANEOUS VELOCITY AND PRESSURE MEASURMENTS

To explore the mechanism of the oscillation in the non-axisymmetic cavity and how this mechanism is affected by the side walls, two-component velocity data are acquired using LDA simultaneously with the unsteady wall-pressure signals. This is done for the cavity with L/D = 3.3 and W/D = 7.4 over x-y planes at the azimuthal symmetry plane ($\Delta\phi$ = 0°, see Figure 2.19 for the definition of $\Delta\phi$) and five other planes ($\Delta\phi$ = -24°, -28°, -32°, -36° and -40°) in the vicinity of the azimuthal location where the harmonic oscillation at $fL/U_\infty \approx 0.21$ is strongest ($\Delta\phi$ = -32° or z/D = -2.62). All measurements are performed for a free-stream velocity of 15 m/s. In this chapter, the velocity-field characteristics will be discussed first, followed by stochastic estimation of the flow field to extract the coherent structures generating the surface-pressure fluctuation.

4.1 Velocity Results and Discussion

4.1.1 Mean-Velocity Field

The mean velocity fields in the x-y planes at $\Delta\phi$ = 0° and $\Delta\phi$ = -32° are compared in Figure 4.1, which displays the mean-velocity vector field for (a) $\Delta\phi$ = 0° and (b) $\Delta\phi$ = -32°. The reference vector at x/D = 0.24 and y/D = 1.89 represents the free-stream velocity and is provided to define the plotting scale of the vector field. The uncertainty of the mean velocity is less than 0.3% of the free stream velocity. Figure 4.2 shows the corresponding streamlines. It can be seen from Figure 4.1 and Figure 4.2 that the mean

flow field in the central plane of the cavity is substantially different from that in the plane close to the cavity side wall where the surface-pressure oscillation is strong.

Figure 4.1 indicates that at $\Delta\phi = 0°$, the main re-circulating flow in the cavity produces back flow that occupies most of the bottom part of the cavity and can reach all the way to the upstream cavity lip. However, at $\Delta\phi = -32°$, the back flow is constrained in the downstream half of the cavity and close to the bottom. The streamlines in Figure 4.2 show that the main recirculation at $\Delta\phi = 0°$ covers the whole cavity length with its center at $x/D \approx 2.6$ and $y/D \approx 0.7$. At $\Delta\phi = -32°$, the flow is dominated by a recirculation flow that is confined in the downstream half of the cavity with the recirculation center at $x/D \approx 2.4$ and $y/D \approx 0.4$. Upstream of the recirculation bubble, the flow is directed towards the downstream direction.

The features of the mean flow field in the central plane, i.e. the presence of a recirculation covering the whole cavity length, is consistent with what is found in open cavity flow (e.g. see Grace *et al* [1], Ozsoy *et al* [2], Ukeiley and Murray[3] and Ashcroft and Zhang[4]). No similar mean flow structure as that shown in Figures 4.1 (b) and 4.2 (b), that is, the confined, low-centered recirculation flow in the downstream half of the cavity, could be found in any of the literature, which generally show measurements only in the central plane of the cavity. It is suspected that this constrained recirculation is somehow related to the presence of side wall.

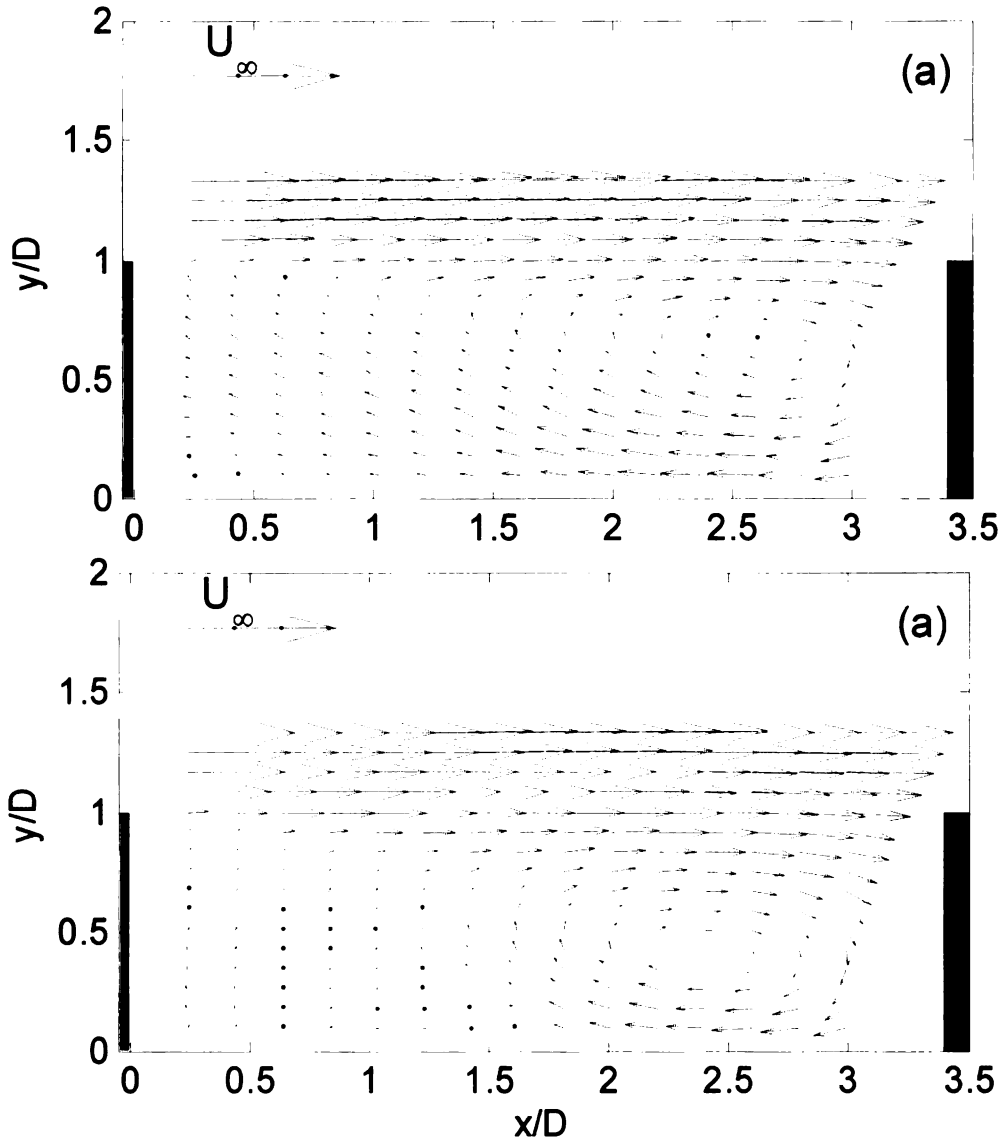

Figure 4.1 Mean-velocity vector field in the x - y planes at (a) $\Delta\phi = 0°$ and (b) $\Delta\phi = -32°$. The isolated vector near the top-left corner of the plots represents the free-stream velocity

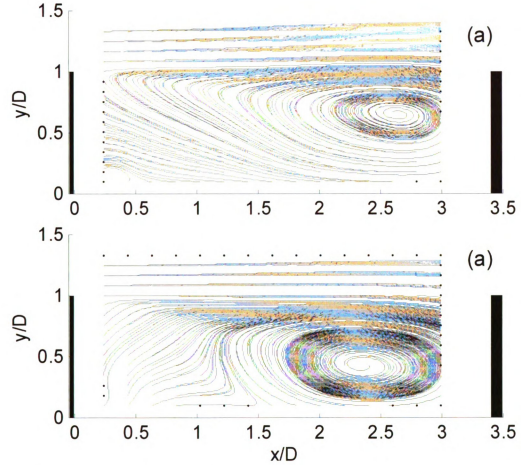

Figure 4.2 Mean streamlines in the x - y planes at (a) $\Delta\phi$ = 0° and (b) $\Delta\phi$ = -32°

4.1.2 Fluctuating-Velocity Field

Figure 4.3 shows flooded color-contour maps of the rms streamwise velocity u'_{rms}/U_∞ at (a) $\Delta\phi$ = 0° and (b) $\Delta\phi$ = -32°; and Figure 4.4 displays similar contour plots for the rms wall-normal velocity v'_{rms}/U_∞. The magnitude of the rms is represented by the color bar provided beneath the plots. The figures indicate that the level of the streamwise-velocity and wall-normal-velocity fluctuation at the cavity opening is higher in the central plane than in the plane at $\Delta\phi$ = -32°. More specifically, the maximum u'_{rms}/U_∞ in the central plane is larger than that at $\Delta\phi$ = -32° by 21% (note that the uncertainty of the rms velocity is less than 1% of the maximum u'_{rms} value in the central

plane). The shape of the contours also exhibits some differences between the two cases. Noteworthy is the observation that if one characterizes the width of the separating shear layer and its lateral spread using the rms of streamwise velocity, u'_{rms}/U_∞, it is seen that (for example, by following the yellow contour in Figure 4.3) the shear layer in the central plane spreads downwards reaching to half the cavity depth at approximately $x/D \approx 2.0$. In contrast, at $\Delta\phi = -32°$, the yellow contour stays confined near the cavity opening for most of the length of the cavity before it starts spreading near the downstream cavity wall. As will be seen in section 4.2.2, the substantial spreading of the shear layer in the downstream half of the cavity at $\Delta\phi = 0°$ is the result of the penetration of the shear layer vortices into the cavity, and their subsequent growth to a scale comparable to the cavity depth. Similar behavior is absent in the plane where the harmonic oscillation are strongest.

For the rms wall-normal velocity, in the central plane, the region with high rms gradually grows from the upstream lip to the downstream edge (Figure 4.4). At $\Delta\phi = -32°$, there is a somewhat sudden lateral expansion of the region with high rms at $x/D \approx 1.5$ after the initial gradual growth. Noting that this is the location of upstream boundary of the confined recirculation (Figure 4.2 (b)), it is believed that this sudden expansion in the contours is related to flow structures in the confined recirculation flow at $\Delta\phi = -32°$. This suggests that the behavior of the v'_{rms} contours is affected by both the shear layer spread and the unsteady recirculation flow.

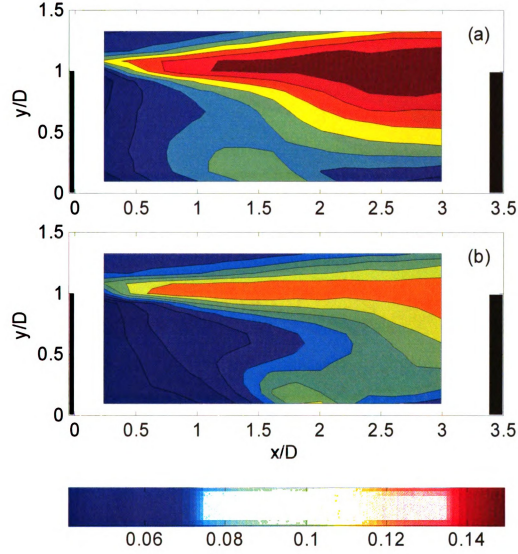

Figure 4.3 Flooded color-contour map of the rms streamwise velocity u'_{rms}/U_∞ in the x - y planes at (a) $\Delta\phi = 0°$ and (b) $\Delta\phi = -32°$. The color bar at the bottom gives the rms values normalized by the free-stream velocity

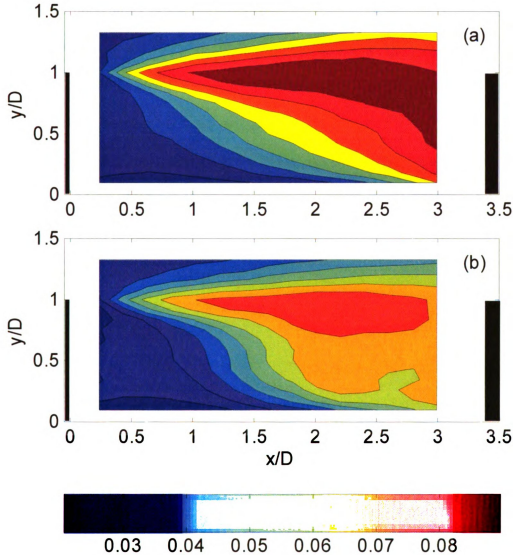

Figure 4.4 Flooded color-contour map of the rms wall-normal velocity v'_{rms}/U_∞ in the x - y planes at (a) $\Delta\phi = 0°$ and (b) $\Delta\phi = -32°$. The color bar at the bottom gives the rms values normalized by the free-stream velocity

4.1.3 Reynolds Shear Stress

Figure 4.5 displays the color contours of the Reynolds-shear-stress $\overline{u'v'}/U_\infty^2$ in the x-y planes at (a) $\Delta\phi = 0°$ and (b) $\Delta\phi = -32°$. The figure shows that $\overline{u'v'}/U_\infty^2$ has its maximum value at the cavity opening for both cases. However, the magnitude of the peak $\overline{u'v'}/U_\infty^2$ at the cavity opening in the central plane is 29% higher than that at $\Delta\phi = -32°$

(note that the uncertainty of the Reynolds shear stress is less than 2% of the peak value in the central plane). In addition, the large spread of the shear layer into the cavity in the downstream half of the cavity at $\Delta\phi = 0°$ discussed above is also reflected in the spread of the Reynolds- shear-stress contours in Figure 4.5 (a). At $\Delta\phi = 32°$, most of the contours in Figure 4.5 (b) remain confined to the cavity opening; again suggesting that in this plane the shear layer does not penetrate into the cavity for most of the cavity length. The "local" penetration of the contours deep into the cavity at $x/D \approx 2.5$ is likely associated with the activity of the recirculation flow structure as will be seen in section 4.2.3.

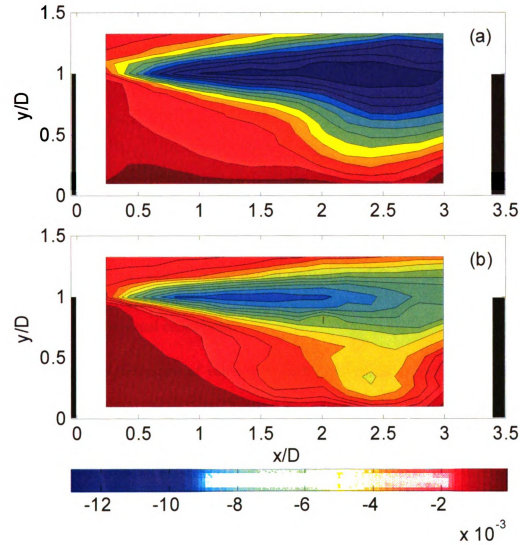

Figure 4.5 Flooded color-contour map of the Reynolds-shear-stress $\overline{u'v'}/U_\infty^2$ in the x - y planes at (a) $\Delta\phi = 0°$ and (b) $\Delta\phi = -32°$. The color bar shows the Reynolds shear stress normalized by the square of the freestream velocity

4.1.4 Mean Vorticity Field

Vorticity ($\bar{\omega}$), the curl of the velocity vector field ($\bar{V}$), is used to characterize the rotation rate of a fluid particle:

$$\bar{\omega} = \nabla \times \bar{V} \qquad \textbf{4.1}$$

Since only two components of the velocity vector are measured in x-y planes, only the out-of-plane vorticity (ω_z) will be discussed. The out-of-plane vorticity is calculated using

$$\omega_z = \frac{\partial v}{\partial x} - \frac{\partial u}{\partial y}, \qquad \textbf{4.2}$$

in which $\frac{\partial v}{\partial x}$ is the partial derivative of the wall-normal velocity with respect to the streamwise coordinate, and $\frac{\partial u}{\partial y}$ is the partial derivative of the streamwise velocity with respect to the wall-normal coordinate.

The spatial derivative of velocity at each point of the measurement grid, except those at the boundary, is calculated using the central finite-difference approximation (expressed below in equations 4.3 and 4.4) employing the neighborhood points shown in Figure 4.6.

$$\left.\frac{\partial v}{\partial x}\right|_{i,j} = \frac{v_{i+1,j} - v_{i-1,j}}{2\Delta x}, \qquad \textbf{4.3}$$

$$\left.\frac{\partial u}{\partial x}\right|_{i,j} = \frac{u_{i,j+1} - u_{i,j-1}}{2\Delta y}, \qquad \textbf{4.4}$$

in which Δx and Δy is the grid spacing in the streamwise and wall-normal direction respectively, and i and j are integer indices indicating the grid node number in the x and y directions respectively. $\frac{\partial v}{\partial x}$ on the upstream and $\frac{\partial u}{\partial y}$ on the bottom boundary of the measurement grid are calculated using the forward difference given by equation 4.5, and their counterparts on the downstream and the top boundary of the measurement grid are

computed employing the backward difference (equation 4.6). Three-point Gaussian smoothing is applied to the mean velocity field before the finite difference is calculated.

$$\left.\frac{\partial v}{\partial x}\right|_{i,j} = \frac{v_{i+1,j} - v_{i,j}}{\Delta x} \quad \& \quad \left.\frac{\partial u}{\partial y}\right|_{i,j} = \frac{u_{i,j+1} - u_{i,j}}{2\Delta y} \qquad \textbf{4.5}$$

$$\left.\frac{\partial v}{\partial x}\right|_{i,j} = \frac{v_{i,j} - v_{i-1,j}}{\Delta x} \quad \& \quad \left.\frac{\partial u}{\partial y}\right|_{i,j} = \frac{u_{i,j} - u_{i,j-1}}{2\Delta y} \qquad \textbf{4.6}$$

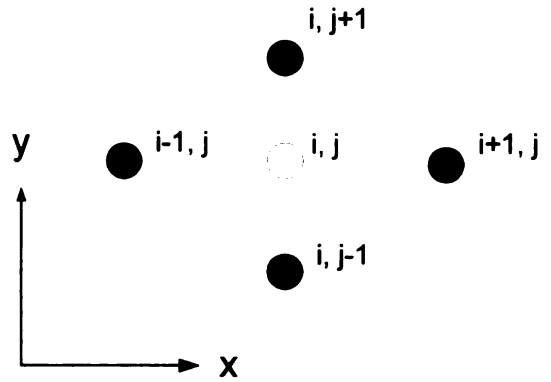

Figure 4.6 Illustration of the layout of neighborhood points used in calculation of velocity derivatives at point (*i, j*)

Figure 4.7 displays the mean normalized out-of-plane vorticity $\overline{\omega}_z D/U_\infty$ in the *x-y* planes at (a) $\Delta\phi$ = 0° and (b) $\Delta\phi$ = -32°. The uncertainty of the mean out-of-plane vorticity is better than 0.4% of the peak value in the central plane. The distribution of vorticity in these two planes looks similar, exhibiting high vorticity concentration close to the separation point. The magnitude of vorticity decreases from the upstream to the downstream lip as the vorticity is diffused laterally into and out of the cavity. As will become clear in section 4.2.2, at $\Delta\phi$ = 0°, the spread of vorticity into the cavity is associated with the growth of the shear layer vortices and their gradual movement into the cavity as they travel downstream. In contrast, at $\Delta\phi$ = -32°, the shear-layer vorticity is

"pulled" into the cavity near the downstream wall of the cavity. This vorticity is then directed downwards along the downstream wall, then upstream along the bottom wall. This results in higher mean vorticity magnitude at $x/D \approx 2.5 \sim 3.0$ and $y/D \approx 0.1 \sim 0.3$ at $\Delta\phi$ = -32° (bottom right corner of the plot in Figure 4.7 (b)) than that at $\Delta\phi$ = 0°. This again indicates that the features of the flow close to the downstream corner at $\Delta\phi$ = -32° are different from that in the central plane of the cavity.

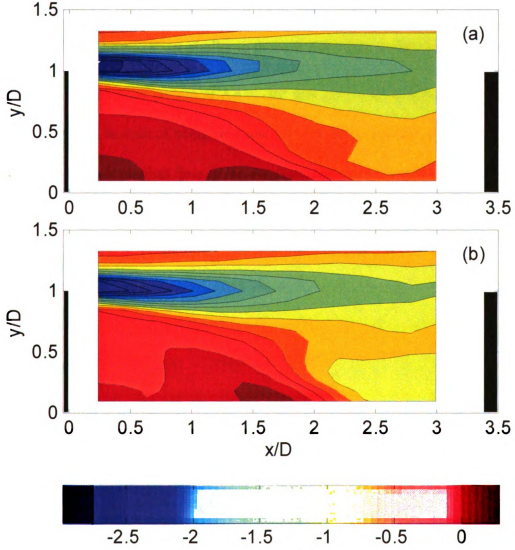

Figure 4.7 Flooded color-contour map of the mean vorticity $\overline{\omega}_z D / U_\infty$ in the *x*-*y* planes at (a) $\Delta\phi$ = 0° and (b) $\Delta\phi$ = -32°. The color bar at the bottom indicates the magnitude of vorticity normalized using the cavity depth and free-stream velocity

4.1.5 Three-Dimensional Flow Field Close to Cavity Side Wall

It is shown from the above results that the mean flow and normal/shear Reynolds stresses in the x-y plane at $\Delta\phi$ = -32°, where the harmonic pressure oscillation is largest, exhibit pronounced differences from that in the central plane of the cavity. To further investigate how the side wall affects the mean flow locally, the mean-velocity field in x-y planes near the side wall at $\Delta\phi$ = -45° will be examined. Figure 4.8 shows the streamlines in the x-y planes at (a) $\Delta\phi$ = -32°, (b) $\Delta\phi$ = -36° and (c) $\Delta\phi$ = -40°. The streamlines pattern at $\Delta\phi$ = -24° and $\Delta\phi$ = -28° are similar to those at $\Delta\phi$ = -32°, so they are not shown here.

The streamlines pattern at $\Delta\phi$ = -36° and $\Delta\phi$ = -40° is evidently different from that at $\Delta\phi$ = -32°. Instead of being confined in the downstream half of the cavity as that at $\Delta\phi$ = -32°, the recirculation flow in the x-y planes at $\Delta\phi$ = -36° and $\Delta\phi$ = -40° covers the whole length of the cavity, similar to the one in the central plane of the cavity. It is worth noting that the center of the recirculation shifts downstream and away from the cavity bottom as the side wall is approached: from $\Delta\phi$ = -32° to $\Delta\phi$ = -40°. Specifically, the center of the recirculation is at $x/D \approx 2.4$ and $y/D \approx 0.4$ for $\Delta\phi$ = -32°, at $x/D \approx 2.8$ and $y/D \approx 0.5$ for $\Delta\phi$ = -36° and at $x/D \approx 3.0$ and $y/D \approx 0.75$ for $\Delta\phi$ = -40°.

In addition to sharing cavity-scale recirculation pattern, it is interesting to note that the strength of the pressure fluctuations at $fL/U_\infty \approx 0.21$ on the downstream wall of the cavity at $\Delta\phi$ = -36° and $\Delta\phi$ = -40° is also similar to that at $\Delta\phi$ = 0°. This can be seen from the frequency spectra plot in Figure 4.9. The figure demonstrates the weakness of the pressure fluctuations at $fL/U_\infty \approx 0.21$ relative to the broadband disturbances at $\Delta\phi$ = -36°, $\Delta\phi$ = -40° and $\Delta\phi$ = 0° compared to that at $\Delta\phi$ = -32°, even though a small peak at

$fL/U_\infty \approx 0.21$ remains visible in the spectra for the former three azimuthal locations. Together, the mean flow and unsteady pressure characteristics indicate that the strong pressure oscillation at $fL/U_\infty \approx 0.21$ at azimuthal location of $\Delta\phi = -32°$ is related to flow structures and/or a mechanism that is causing the confined recirculation in the downstream half of the cavity.

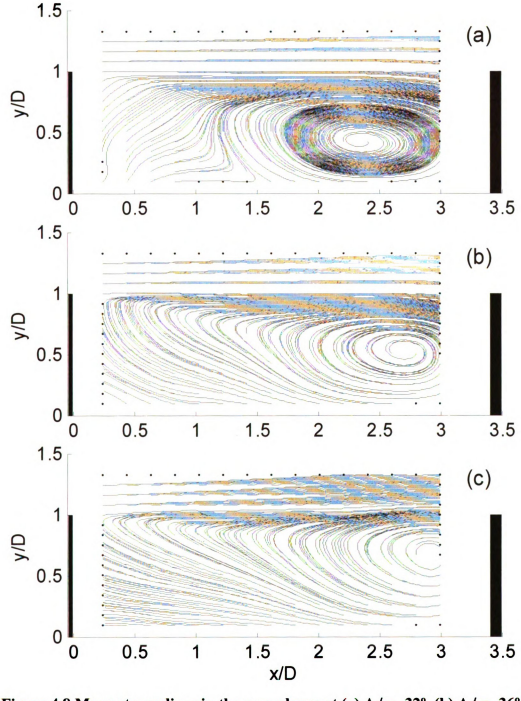

Figure 4.8 Mean streamlines in the x - y planes at (a) $\Delta\phi = -32°$, (b) $\Delta\phi = -36°$ and (c) $\Delta\phi = -40°$

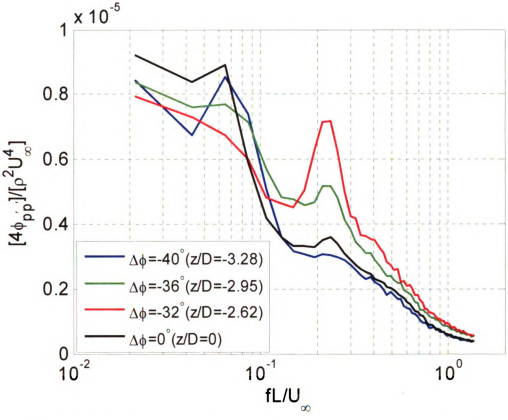

Figure 4.9 Frequency spectra at selected azimuthal locations for the cavity with *W/D* = 7.4. Lines with different colors represent different azimuthal locations

To further understand the three-dimensional flow field close to the cavity side wall, the third mean-velocity component normal to the x-y plane (i.e. in the azimuthal direction), $\bar{u}_\phi$ is calculated within the cavity ($0 < y/D < 1$) in five x-y planes at $\Delta\phi$ = -40°, $\Delta\phi$ = -36°, $\Delta\phi$ = -32°, $\Delta\phi$ = -28° and $\Delta\phi$ = -24°. This is accomplished by solving the continuity equation for the mean flow with known streamwise and wall-normal velocity and the no-slip boundary condition at the cavity side wall ($\Delta\phi$ = -45°). The continuity equation is given by:

$$\frac{1}{r}\frac{\partial}{\partial r}(r\bar{u}_r)+\frac{1}{r}\frac{\partial}{\partial \phi}(\bar{u}_\phi)+\frac{\partial}{\partial x}(\bar{u}_x)=0, \qquad \textbf{4.7}$$

where r, ϕ and x are cylindrical coordinates and $\bar{u}_r$, $\bar{u}_\phi$ and $\bar{u}_x$ are the corresponding mean-velocity components. Figure 4.10 illustrates the cylindrical coordinate system, in which x points in the streamwise direction along the axis of the model and is perpendicular to the plane of the figure, and r is the radial coordinate measured from the center of the model. Note that r and y, as defined in Figure 1.1, are related by $r = y + r_o$, where r_o is the model radius (50.8 mm). Thus, $\bar{u}_x$ is the streamwise velocity $\bar{u}$ and $\bar{u}_r$ is the wall-normal velocity $\bar{v}$.

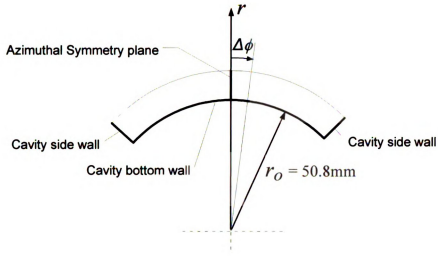

Figure 4.10 Illustration of the cylindrical coordinate system with origin at the center of the axsiymmetric model

Employing backward-difference approximation for $\frac{\partial \overline{u}_\phi}{\partial \phi}$ and central difference for $\frac{\partial \overline{u}_x}{\partial x}$ and $\frac{\partial (r\overline{u}_r)}{\partial r}$, equation 4.7 can be written as

$$\frac{\overline{u}_\phi\big|_{i,j,k} - \overline{u}_\phi\big|_{i,j-1,k}}{\delta\phi} = -[r]_{i,j,k}\left[\frac{\overline{u}_{i,j,k+1} - \overline{u}_{i,j,k-1}}{2\Delta x} + \frac{(r\overline{u}_r)_{i+1,j,k} - (r\overline{u}_r)_{i-1,j,k}}{2\Delta r}\right], \quad \textbf{4.8}$$

in which Δr, $\delta\phi$ and Δx are the grid spacing in the radial, azimuthal and streamwise direction respectively, and i, j and k are integer indices indicating the grid node number in the same directions respectively. On the upstream and the bottom boundary of the measurement grid in an x-y plane, the finite-difference approximation of $\frac{\partial \overline{u}_x}{\partial x}$ and $\frac{\partial (r\overline{u}_r)}{\partial r}$ in equation 4.8 employs forward difference; and their counterparts on the downstream and the top boundary of the measurement grid are computed employing the backward difference . Thus, $\overline{u}_\phi$ in five x-y planes at $\Delta\phi$ = -40°, $\Delta\phi$ = -36°, $\Delta\phi$ = -32°,

$\Delta\phi$ = -28° and $\Delta\phi$ = -24° within the cavity ($0 < y/D < 1$) is calculated by solving equation 4.8 with known streamwise ($\bar{u}_x$) and wall-normal ($\bar{u}_r$) velocity and the no-slip boundary condition ($\bar{u}_r|_{\Delta\phi=-45°} = \bar{u}_\phi|_{\Delta\phi=-45°} = \bar{u}_x|_{\Delta\phi=-45°} = 0$) at the cavity side wall ($\Delta\phi$ = -45°),

Figure 4.11 shows profiles of the mean azimuthal velocity $\bar{u}_\phi / U_\infty$ along the wall-normal direction y at different azimuthal and streamwise locations. Near the downstream cavity wall, at x/D = 3.0 and 2.8, shown in Figure 4.11 (a) and (b) respectively, the azimuthal velocity is negative everywhere, which means the mean flow is directed towards the side wall. Farther upstream, at x/D = 2.4, the mean azimuthal velocity changes to positive in the top part of the cavity, which indicates the mean flow moves away from the side wall. At x/D = 2.2 the region of positive azimuthal velocity along the y direction increases and the magnitude of azimuthal velocity also increases. At x/D = 2.0, the azimuthal velocity reaches its maximum positive value at y/D = 0.92 (the upper boundary of the calculation) and the region with positive $\bar{u}_\phi$ is also the largest found within the measurement domain. The peak $\bar{u}_\phi$ magnitude is about the same as the peak $\bar{u}_r$, or $\bar{v}$, magnitude (about 10% of the free-stream velocity). At x/D = 1.8 the extent of the region with positive $\bar{u}_\phi$ (i.e with net flow towards the center of the cavity) starts to decrease, accompanied with a reduction in the magnitude of the azimuthal velocity. Overall, the data in Figure 4.11 show that there is a net mean flow towards the center of the cavity in the top half of the cavity in the approximate range $1.8 < x/D < 2.5$: a point that will have significance when discussing the oscillation mechanism in section 4.2.

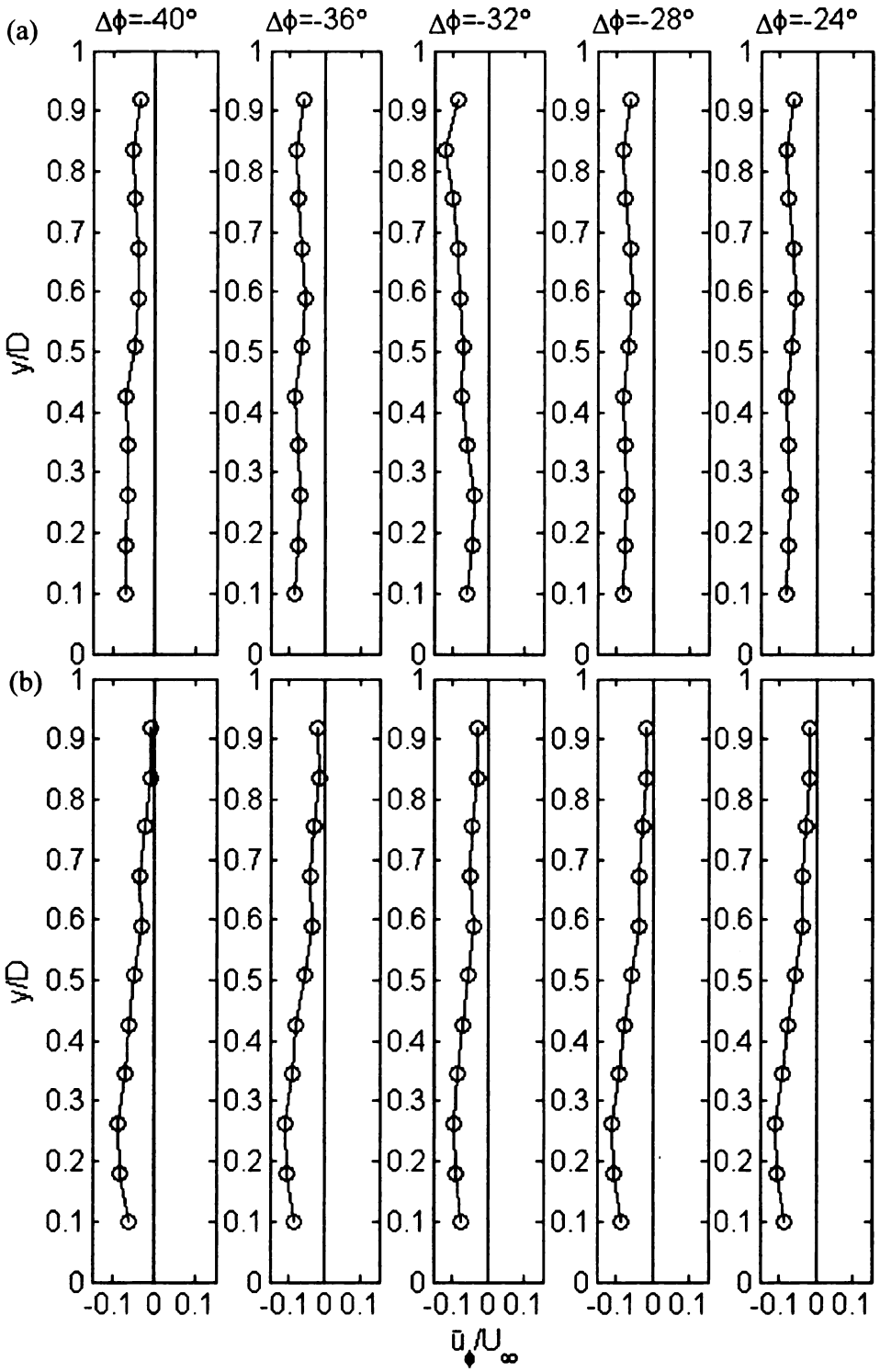

Figure 4.11 Wall-normal profiles of the mean azimuthal velocity $\bar{u}_\phi / U_\infty$ at different azimuthal locations and (a) x/D = 3.0, (b) x/D = 2.8, (c) x/D = 2.4, (d) x/D = 2.2, (e) x/D = 2.0 and (f) x/D = 1.8

Figure 4.11 continued:

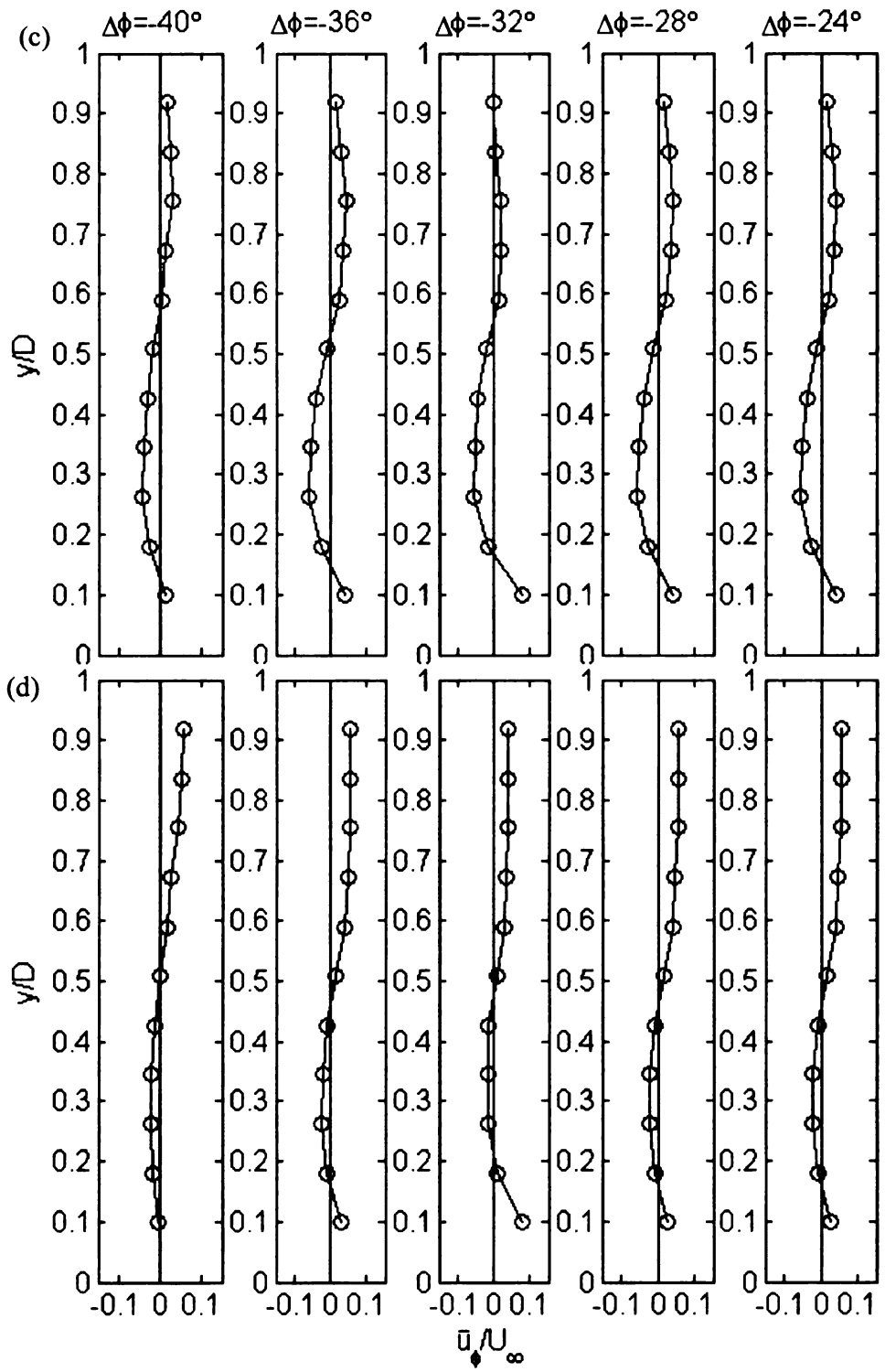

Figure 4.11 continued:

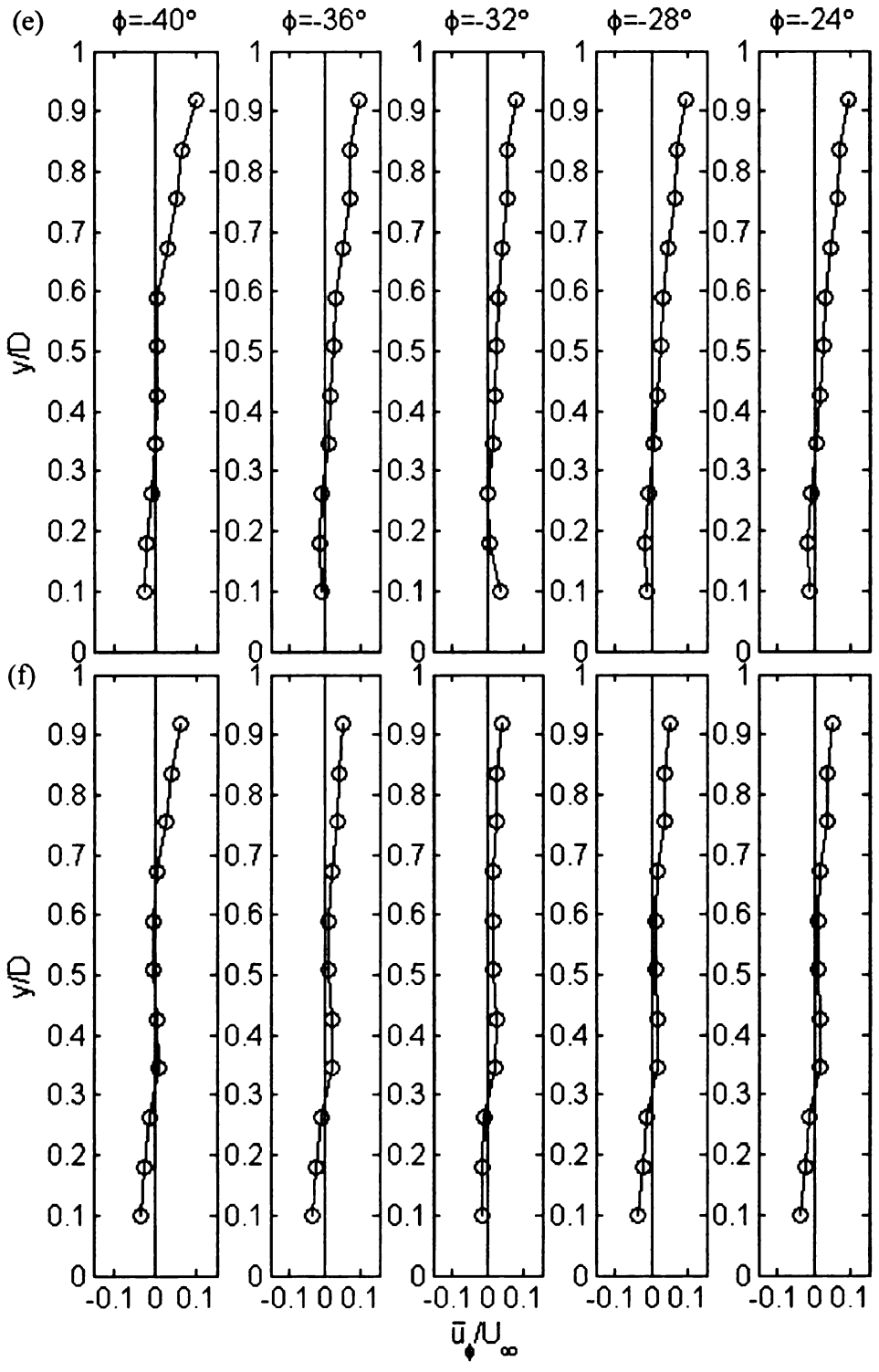

To provide a more complete view of the cross-flow found above, the mean streamlines in y-ϕ planes at different streamwise locations are shown in Figure 4.12 and Figure 4.13. At x/D = 3.0, downstream of the recirculation core in all measured x-y planes (the most downstream recirculation center is at x/D = 3.0 at $\Delta\phi$ = -40°, as shown in Figure 4.8), the flow is directed towards the side wall from above and from the center part of the cavity. At x/D = 2.8, upstream of the circulation center in the x-y plane at $\Delta\phi$ = -40°, the flow remains directed towards the side wall but it now appears to "spill over" the top side corner of the cavity. Between $x/D \approx$ 2.6 - 2.4, in the vicinity of the main recirculation center in the x-y plane at $\Delta\phi \approx$ -36° - -24°, the flow is directed upwards after interaction with the side wall and a circulatory flow pattern forms in the y-ϕ planes. At x/D = 2.2 and 2, upstream of the recirculation center in all x-y planes, the flow has strong directivity towards the center of the cavity in the upper half of the cavity. Overall, the results in Figures 4.12 and 4.13, highlight the highly complex three-dimensional flow character inside the cavity.

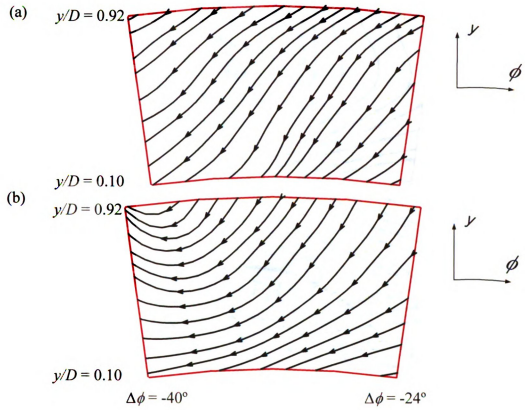

Figure 4.12 Mean streamlines in the y-ϕ planes at (a) $x/D = 3.0$ and (b) $x/D = 2.8$. The streamwise direction is into the paper

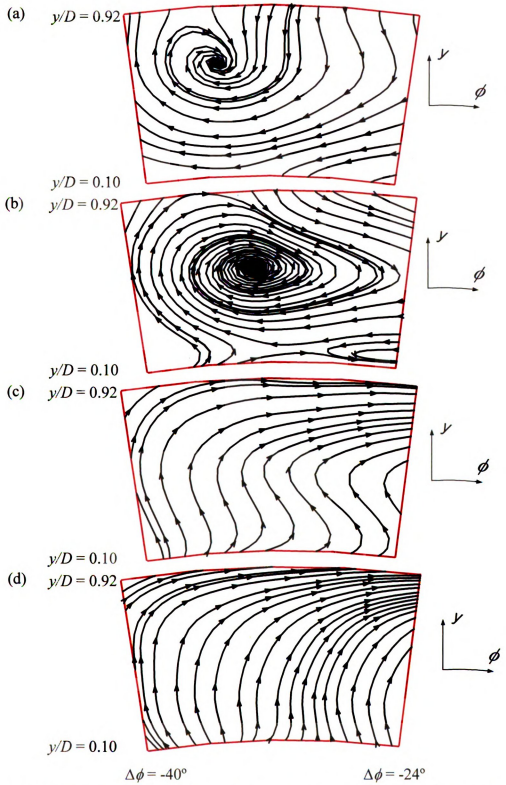

Figure 4.13 Mean streamlines in the y-ϕ planes at (a) x/D = 2.6, (b) x/D = 2.4, (c) x/D = 2.2 and (d) x/D = 2.0. The streamwise direction is into the paper

Additional insight into the three-dimensional character of the mean flow can be gained through inspection of Figures 4.14 and 4.15, which display selected three-dimensional streamlines inside the cavity within the region between $\Delta\phi$ = -40° to $\Delta\phi$ = -24°. Figure 4.14 demonstrates the streamlines originating from $x/D \approx 2.6$ at $\Delta\phi$ = -40°. The streamlines indicate that the mean flow field originating close to the side wall swirls around the main recirculation flow as it is driven towards the middle potion of the cavity. The cross-flow towards the cavity center can be highlighted further by considering the streamlines near the center of the recirculation flow (displayed in Figure 4.15).

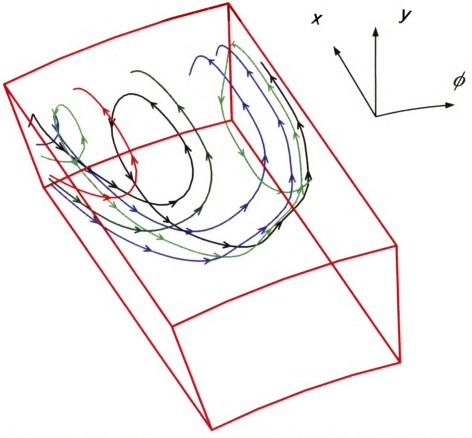

Figure 4.14 Mean three-dimensinal streamlines originating near the cavity's side wall: from $x/D \approx 2.6$ at $\Delta\phi$ = -40°

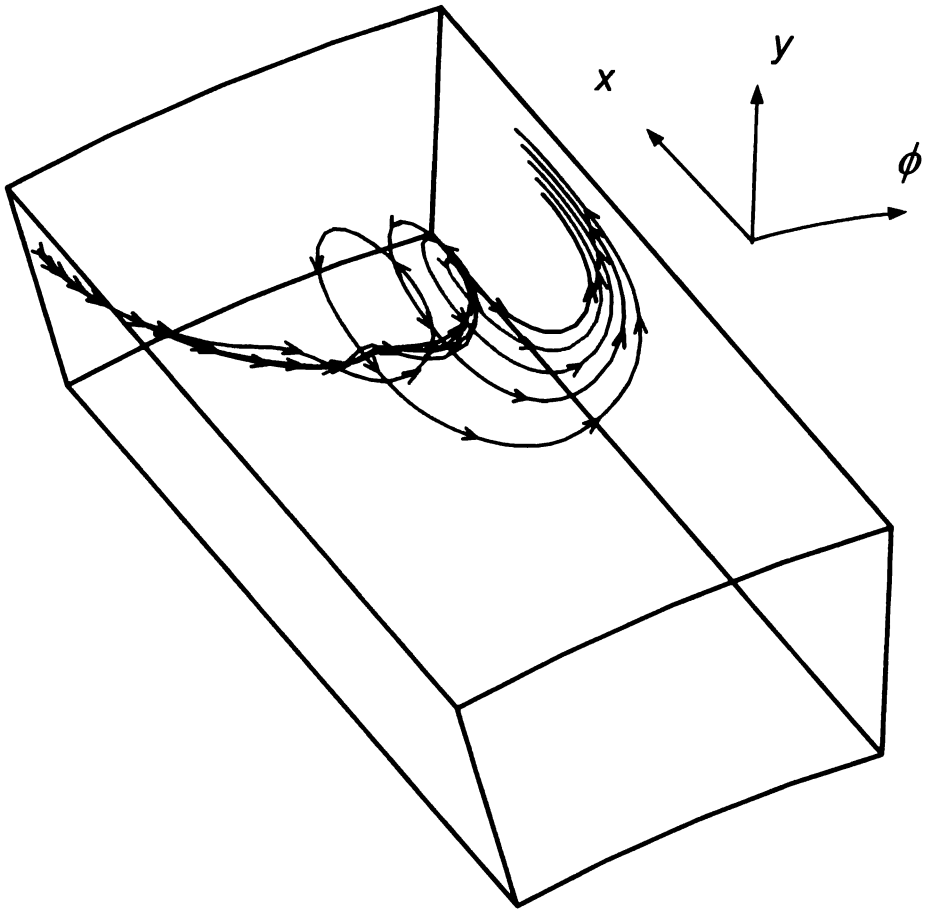

Figure 4.15 Mean three-dimensional streamlines originating near the cavity's side wall and the center of recirculation: from $x/D \approx 2.9$ and $y/D \approx 0.75$ at $\Delta\phi = -40°$

It is useful to compare the complex three-dimensional flow found here inside the cavity to the flow inside a lid-driven cavity (in which the shear layer is replaced by a solid wall moving in the streamwise direction). The comparison is motivated by two factors: 1) no numerical or experimental studies could be found of shear-driven cavity flows, in which the cavity width is finite and details regarding the 3D flow inside the cavity are provided; 2) it is believed that the flow features *inside* a finite-width cavity, whether it is driven by a moving wall or a shear layer, should bear some similarity. Of particular relevance to the present findings is the comparison with the detailed numerical study of a finite-width rectangular, lid-driven cavity at relatively low Reynolds number

by Chiang *et al.*[5]. These authors found particles to circuit around the primary recirculation flow inside the cavity towards the side wall, and then (similar to the present flow) spiral to the symmetry plane along the core of the primary recirculation. Chiang *et al.* found the cross-flow towards the center to be driven by a spanwise pressure gradient. Although caused by a different mechanism, the cross-flow found here is also believed to be driven by a spanwise pressure gradient. How this pressure gradient is established, and the significance of the resulting cross flow to the observed harmonic oscillations near the side wall will be discussed in the following section.

4.2 Stochastic Estimation of the Coherent Structures Generating Wall-Pressure Fluctuations

Stochastic Estimation (SE) as an approach to extract coherent structures in turbulent flows was first proposed by Adrian[6]. It is a conditional-averaging technique that uses unconditional statistics (two-point correlations) to estimate a stochastic flow variable at a particular point in space or time based on the information of a known variable at the same or other point. Adrian[7] and Guezennec[8] showed the capability of SE in estimating the turbulent velocity field based on velocity measurements at different locations. Naguib *et al*[9] was the first study to estimate the flow sources related to surface pressure events in a turbulent boundary layer. They estimated the flow field using both linear stochastic estimation (LSE) and quadratic stochastic estimation (QSE), and found it was necessary to include the quadratic term in the estimation. This was related to the generation of the wall pressure by the nonlinear sources of the conditional velocity field. Murray and Ukeiley[10] applied stochastic estimation to predict the temporal evolution of the velocity field in a 2D open cavity using surface-pressure information. They compared the estimation with direct numerical simulation and showed that adding more pressure "measurement" locations in LSE only improves the estimation in regions close to where the pressure was acquired. They found that the linear estimation was able to predict most of the time-resolved flow evolution, but the quadratic term was necessary in capturing the turbulent energy and finer details of the vorticity field. Hudy[11] successfully predicted the evolution of the flow structures generating the surface-pressure signature on the same axisymmetric model employed here (but for a backward-facing-step geometry) using

LSE estimation based on the wall-pressure array measurements beneath the separating/reattaching flow.

Since the wall-pressure signature inside the cavity is dominated by unsteadiness near the cavity's downstream wall (see Figures 3.1, 3.2 and 3.3 for the axisymmetric case), in this section the evolution of the flow structures in the cavity is done based on the surface-pressure signal on the downstream wall. In particular, the velocity fluctuation at a certain location and time, $u'(x_0+\Delta x, y_0+\Delta y, z_0+\Delta z, t+\Delta t)$ is estimated using the wall-pressure fluctuation (also known as "condition", or "event") $p'(x_0, y_0, z_0, t)$. Within the SE framework, the estimated velocity fluctuation, $\tilde{u}'$, is expressed in a Taylor series expansion in terms of the pressure condition:

$$\tilde{u}'(x_0+\Delta x, y_0+\Delta y, z_0+\Delta z, t+\Delta t) = A(\Delta x,\Delta y,\Delta z,\Delta t; x_0; y_0; z_0)p'(x_0, y_0, z_0, t) + B(\Delta x,\Delta y,\Delta z,\Delta t; x_0; y_0; z_0)p'^2(x_0, y_0, z_0, t) + O(p'^3) \quad \textbf{4.9}$$

where x_0, y_0 and z_0 are the streamwise, wall-normal and spanwise (or azimuthal) location of the reference pressure, and t is the instance when the pressure event occurs. Δx, Δy, Δz and Δt are the streamwise, wall-normal, spanwise distance and time offset between the estimated velocity and reference pressure. A is the linear estimation coefficient and B is the quadratic estimation coefficient. The estimation coefficients are determined by minimizing the expectation, E, of the squared error between the estimated and measured velocity:

$$\mathrm{E}(e^2) = < \{\tilde{u}'(x_0+\Delta x, y_0+\Delta y, z_0+\Delta z, t+\Delta t) - u'(x_0+\Delta x, y_0+\Delta y, z_0+\Delta z, t+\Delta t)\}^2 > \quad \textbf{4.10}$$

The minimization problem leads to: $\frac{\partial \mathrm{E}(e^2)}{\partial A} = 0$ and $\frac{\partial \mathrm{E}(e^2)}{\partial B} = 0.$

In LSE,

$$A = \frac{< u'(x_0 + \Delta x, y_0 + \Delta y, z_0 + \Delta z, t + \Delta t) p'(x_0, y_0, z_0, t) >}{< p'(x_0, y_0, z_0, t) p'(x_0, y_0, z_0, t) >} = \frac{r_{u'p'}}{p'^2_{rms}},$$

and $B = 0,$ **4.11**

where $r_{u'p'}$ is the correlation between the velocity and pressure. Equations 4.9 and 4.11 yield single-point LSE of the streamwise velocity. Similar equations with u' replaced with v' give LSE of the wall-normal velocity. In most cases, it is desired to estimate the instantaneous flow field from concurrent pressure information, and hence the estimation coefficient is only a function of space (Δx , Δy and Δz) while the time offset Δt = 0. As a result, the temporal evolution of the velocity field is estimated based on the evolution of the pressure event. The method works well at locations where there is good velocity-pressure correlation at time offset of zero. To ensure that such correlation is maintained with all points within the flow, multiple pressure events measured at distributed points on the wall are typically used; this leads to the so-called, multi-point LSE (e.g. see Hudy[11]).

Although in the present study, multi-point LSE could be used based on information from the streamwise and spanwise microphone arrays, no good correlation could be found at a time offset of zero between any of the microphone's signals and the velocity signature of the shear layer in the upstream half of the cavity. Hence, the approach didn't capture the shear-layer evolution well.

Generally speaking, the pressure signal measured at a particular location correlates well with the velocity field within its vicinity at zero time offset. If this signal

is produced by a coherent structure, such as the shear-layer vortices, the pressure signal is also well correlated with the velocity at remote spatial locations along which this structure evolves; although in this case, the correlation would be found at positive or negative time offsets. To take advantage of this temporal relationship in LSE, equations 4.9 and 4.11 are employed here in the following sense: a pressure event with a given magnitude is specified at location x_0, y_0 and z_0, which is taken on the downstream wall of the cavity. The temporal evolution of the velocity field is then captured by considering the estimated velocity field at different time offsets Δt before, at the same time, and after the event has occurred. Note that in this estimation, which can be considered as single-point *multi-time-offset* estimation, the event is fixed but the estimation coefficient (which expresses the pressure-velocity correlation at different time offsets) changes with time relative to the occurrence of the event.

More generally, the estimation used here can be viewed as a special case of single-point, *multi-time* estimation, in which, the velocity at a given point in the flow is estimated from past, current, and future values of the pressure measured at a point on the wall (see Durgesh[12]). The approach leads to a linear algebraic set of equations of order equal to the number of temporal pressure points used in the estimation. The equation set is solved to obtain the estimation coefficients. In this thesis, the simpler approach described above is used since it is found to capture the shear-layer evolution satisfactorily. Finally, it is noted that quadratic estimation was also conducted in this work but found not to add information about the propagation/evolution of the shear layer structures but only regarding the re-circulating flow inside the cavity.

4.2.1 Velocity-Pressure Correlation

As seen above, linear stochastic estimation requires information about the velocity-pressure correlation in order to calculate the estimation coefficient (see equation 4.11). Example of such correlation is given in Figure 4.16 at different time offsets. The figure contains flooded color contour maps of the correlation between the fluctuating streamwise velocity in the x-y plane at $\Delta\phi$ = -32° and the wall-pressure fluctuations on the downstream wall of the cavity at x/D = 3.3 and y/D = 0.5 (indicated by the blue open circle). The correlation value is normalized by the freestream velocity U_∞ and dynamic pressure $1/2\rho U_\infty^2$, i.e. $R_{u'p'} = r_{u'p'}/(1/2\rho U_\infty^3)$, to emphasize the global importance of regions with high correlation. If normalized by local rms values, the correlation falls between -0.3 and 0.3. The reference surface-pressure signature are band-pass filtered between 50 Hz to 150 Hz (fL/U_∞ = 0.137- 0.410) in order to focus the analysis on disturbances generating the pressure oscillation at $fL/U_\infty \approx 0.21$. Figure 4.17 shows similar contours for the wall-normal velocity component: $R_{v'p'}$. Figure 4.18 and Figure 4.19 display correlation contours of $R_{u'p'}$ and $R_{v'p'}$ respectively in the x-y plane at $\Delta\phi$ = 0°. The region with high correlation indicates locations within the flow where the disturbances are correlated with the reference pressure signature. The evolution of the correlation with time offset in Figures 4.16 through 4.19 tracks the propagation of velocity disturbances that are related to the surface-pressure oscillation. It is interesting to note that the region with high correlation in the symmetry plane extends more upstream, close to the separation point, compared to that in the x-y plane at $\Delta\phi$ = -32°. The flow structure associated with these disturbances will become evident through the use of these

correlation results to arrive at linear stochastic estimation of the flow field based on the unsteady pressure on the end wall.

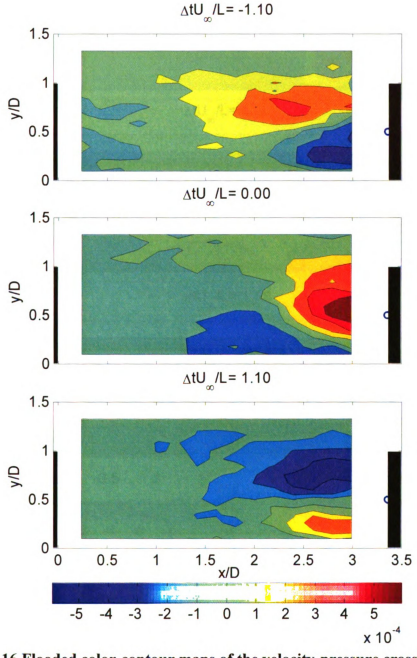

Figure 4.16 Flooded color-contour maps of the velocity-pressure cross-correlation ($R_{u'p'}$) at $\Delta\phi$ = -32°. Pressure is measured at x/D = 3.3 and y/D = 0.5 (shown by the blue circle on the end wall of the cavity). Correlation results are shown at zero time delay (middle plot) as well as at time delays corresponding to ± 1/4 the oscillation period at $fL/U_\infty \approx 0.21$. The color bar at the bottom of the plot gives $R_{u'p'}$ values

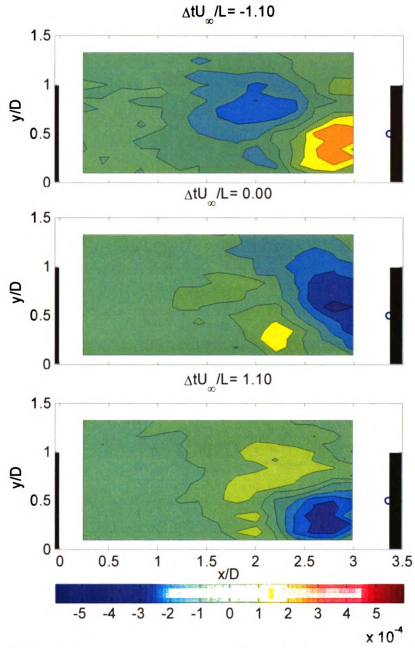

Figure 4.17 Flooded color-contour maps of the velocity-pressure cross-correlation ($R_{v'p'}$) at $\Delta\phi = -32°$. Pressure is measured at $x/D = 3.3$ and $y/D = 0.5$ (shown by the blue circle on the end wall of the cavity). Correlation results are shown at zero time delay (middle plot) as well as at time delays corresponding to ± 1/4 the oscillation period at $fL/U_\infty \approx 0.21$. The color bar at the bottom of the plot gives $R_{v'p'}$ values

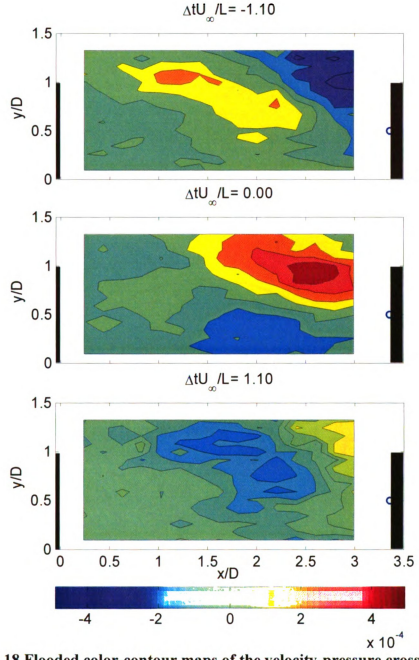

Figure 4.18 Flooded color-contour maps of the velocity-pressure cross-correlation ($R_{u'p'}$) at $\Delta\phi = 0°$. Pressure is measured at $x/D = 3.3$ and $y/D = 0.5$ (shown by the blue circle on the end wall of the cavity). Correlation results are shown at zero time delay (middle plot) as well as at time delays corresponding to ± 1/4 the oscillation period at $fL/U_\infty \approx 0.21$. The color bar at the bottom of the plot gives $R_{u'p'}$ values

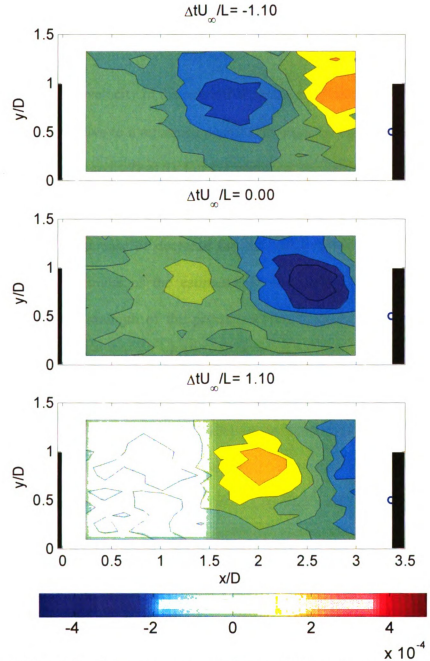

Figure 4.19 Flooded color-contour maps of the velocity-pressure cross-correlation ($R_{v'p'}$) at $\Delta\phi = 0°$. Pressure is measured at $x/D = 3.3$ and $y/D = 0.5$ (shown by the blue circle on the end wall of the cavity). Correlation results are shown at zero time delay (middle plot) as well as at time delays corresponding to ± 1/4 the oscillation period at $fL/U_\infty \approx 0.21$. The color bar at the bottom of the plot gives $R_{v'p'}$ values

4.2.2 Evolution of the Coherent Structures in the Azimuthal-Symmetry Plane of the Cavity

The fluctuating velocity in the azimuthal symmetry plane ($\Delta\phi = 0°$) is estimated at different time lags relative to a reference positive pressure on the downstream wall in the same plane (at x/D=3.3 and y/D=0.5). For convenience, the reference pressure is taken as $p' = p_{rms}$. Because of the linearity of the estimation, stronger or weaker pressure magnitude will only increase or decrease the estimated velocity magnitude but not its direction; thus, the features of the estimated flow structures are independent of the specific choice of the strength of the pressure event. Figure 4.20 (1) - (12) show the evolution of the vorticity contours of the estimated flow field (without the addition of the mean flow) and the streamlines of the total velocity (with the addition of the mean flow; details of the superposition of the estimated and mean velocity field is explained in the following paragraph) at different time offsets preceding and following the occurrence of the positive pressure condition (for $\Delta t = 0$: shown in Figure 4.20 (7)) with a time interval of $\Delta t U_\infty/L = 0.375$ covering one period of the oscillation at $fL/U_\infty \approx 0.21$. The blue circle on the cavity's downstream wall marks the location of the reference wall pressure. Note that showing the vorticity contours based on the estimated *fluctuating* velocity in Figure 4.20 is done to emphasize the unsteady flow structure. Also, three-point Gaussian smoothing is applied to the estimated velocity field before the vorticity is calculated.

Figure 4.20 depicts a small concentration of vorticity apparently originating from the shear layer, near the upstream lip (pointed to by an arrow in Figure 4.20 (1) at $\Delta t U_\infty/L$ = -2.20). This vorticity concentration seems to correspond to a vortex which grows as it propagates downstream and into the cavity (see Figure 4.20 (2) through (7) from $\Delta t U_\infty/L$

= -1.83 to 0). Subsequently, the vortex is shed out of the cavity and decays (see Figure 4.20 (7) through (12) from $\Delta t U_\infty / L$ = 0 to 1.83). The process of vortex growing while penetrating into the cavity and shedding resembles that for the cavity wake mode (see Najm and Ghoniem[13] and Rowley *et al.*[14]). In fact, as discussed previously in section 3.1, the frequency of the weak peak in the wall-pressure spectra at $\Delta\phi$ = 0° shown in Figure 4.9 is 0.06 if normalized by the cavity depth, which is the same as the frequency of the wake mode found by Rowley *et al.*[14]. A significant point is that when the vortex structure penetrates into the cavity, it overlaps the *x-y* domain over which mean cross-flow towards the cavity center is found in the analysis of the mean three-dimensional flow. The extent of this domain, as found from the results of section 4.1.5, is outlined in Figure 4.20 using a broken-line rectangle. Outside the highlighted domain, the vortex is practically outside of the cavity. These observations suggest that the cross-flow towards the center of the cavity may in fact be related to the penetration of the shear-layer's vortex structure into the cavity and its subsequent growth/strengthening. It is important to note that such penetration is a feature of the wake mode, and it does not take place in the shear-layer (Rossiter) type cavity unsteadiness.

Figure 4.21 displays the contours of vorticity, $\omega_z D / U_\infty$ and streamlines, calculated from the *total* velocity in the *x-y* plane of $\Delta\phi$ = 0° at different time offsets relative to a positive pressure condition on the downstream wall at *x/D* = 3.3 and *y/D* = 0.5. The plot is obtained by multiplying the estimated velocity field by a factor then superposing the outcome on the mean velocity field. The multiplication by a factor is done to strengthen the estimated flow structures relative to the mean velocity. This is necessary since the conditional averaging associated with stochastic estimation inevitably

weakens the strength of the estimated structures. Hence, when superposing the estimated and mean fields, the latter could dominate the outcome. A factor of 15 is chosen so that the peak vorticity of the vortex structure during its evolution is of similar magnitude to the peak mean vorticity at separation. This accounts for the fact that the vortex structure forms from the roll-up of the shear layer, while ignoring the effects of viscous diffusion and vorticity stretching/tilting. It is important to note, however, that the features of the unsteady structures is not affected by the multiplication factor but only the strength of them relative to the mean flow. The purpose of superposing the estimated and mean fields is to help visualize the unsteady structures in relation to the separating shear layer.

The region with large negative vorticity value in Figure 4.21 highlights the location of the shear layer. The figure illustrates that the shear layer dips into the cavity during the time period of $\Delta t U_\infty/L$ = -2.20 ~ 0 (from Figure 4.21 (1) to (7)) when vortex structures grow and propagate (shown in Figure 4.20 (1) through (7))), and it moves out of the cavity during the period of $\Delta t U_\infty/L$ = 0 ~ 1.83 (see Figure 4.21 (7) through (12)) when vortex structures are shed out of the cavity and decay.

Figure 4.22 shows the fluctuating wall-pressure on the cavity bottom (blue line in Figure 4.22) and on the downstream wall (red circle in Figure 4.22) beneath flooded color-contour maps of the streamlines and estimated vorticity at two instances: when the pressure on the downstream wall is peak positive and peak negative. The fluctuating wall-pressure is estimated using the same method as that for the velocity. The figure shows that the pressure on the downstream wall reaches a positive peak when the vortex structure inside the cavity grows to a size compatible to the cavity depth, and penetrates into the cavity, directing the high-speed flow from above towards the downstream wall;

the pressure reaches a negative peak when the vortex structure is shed out of the cavity. This is associated with pumping of fluid out of the cavity's downstream corner, as shown by the streamlines.

In summary, the stochastic estimation results suggest that the wall-pressure fluctuations in the symmetry plane are generated by the growth and shedding of vortex structures accompanied by the flapping of the shear layer into and out of the cavity. The coherent structures represent a cavity wake mode even though the pressure oscillation is not pronounced in the symmetry plane. However, it is believed that the wake mode vortex structures are responsible for "pumping" fluid from the side-wall vicinity towards the cavity center, ultimately leading to the strong harmonic oscillations found near the wall (as will be discussed below).

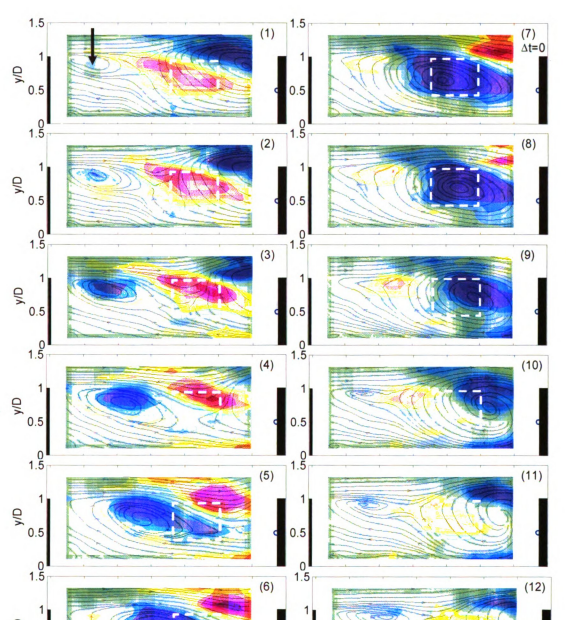

Figure 4.20 Streamlines and estimated fluctuating vorticity $\widetilde{\omega}'_z D/U_\infty$ contours at $\Delta\phi = 0°$ for different time offsets (covering one period of the oscillation at $fL/U_\infty \approx 0.21$ with a time interval of $\Delta t U_\infty/L = 0.365$) preceding and following the occurrence of a positive pressure ($p' = p_{rms}$ at $\Delta t = 0$ in (7)) at $x/D = 3.3$ and $y/D = 0.5$. The color map on the bottom gives $\widetilde{\omega}'_z D/U_\infty$ values

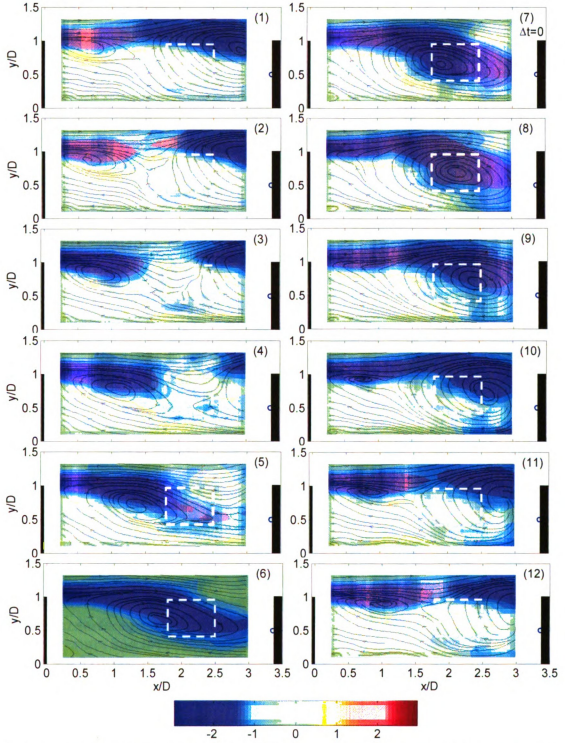

Figure 4.21 Streamlines and vorticity $\omega_z D/U_\infty$ contours at $\Delta\phi = 0°$ for different time offsets (covering one period of the oscillation at $fL/U_\infty \approx 0.21$ with a time interval of $\Delta t U_\infty/L = 0.365$) preceding and following the occurrence of a positive pressure ($p' = p_{rms}$ at $\Delta t = 0$ in (7)) at $x/D = 3.3$ and $y/D = 0.5$. The color map on the bottom gives $\omega_z D/U_\infty$ values

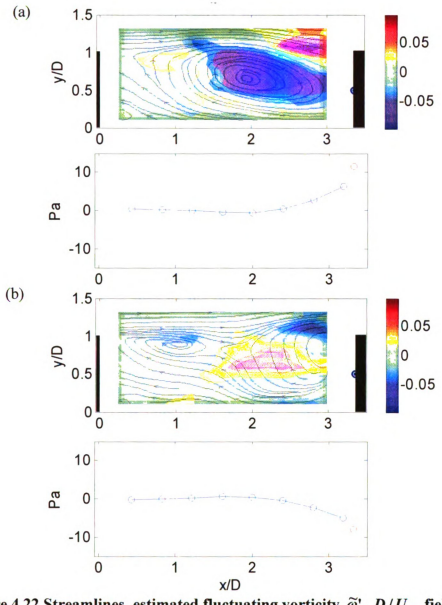

Figure 4.22 Streamlines, estimated fluctuating vorticity $\tilde{\omega}'_z D/U_\infty$ field and concurrent surface pressure in the *x-y* plane of $\Delta\phi = 0^o$ corresponding to: (a) peak positive pressure and (b) peak negative pressure on the cavity end wall at $x/D = 3.3$ and $y/D = 0.5$ (pressure value shown with red circle). Blue line shows the pressure distribution on the cavity bottom, and color bar gives $\tilde{\omega}'_z D/U_\infty$ values

4.2.3 Evolution of the Coherent Structures Close to the Cavity Side Wall

Figure 4.23 shows the streamlines and estimated fluctuating vorticity ($\tilde{\omega}'_z D/U_\infty$) field in the x-y plane at $\Delta\phi$ = -32° for different time offsets (extending over one period of the oscillation cycle at $fL/U_\infty \approx 0.21$) relative to a positive pressure ($p' = p_{rms}$) on the downstream wall at x/D = 3.3 and y/D = 0.5. Recall that the wall-pressure signature in this plane is dominated by the pronounced harmonic oscillation at $fL/U_\infty \approx 0.21$ (shown in Figure 3.21 and Figure 4.9). No obvious vortex growing and shedding as found at $\Delta\phi$ = 0° is observed in Figure 4.23. Instead, the flow seems to be dominated by the "splitting" and pulling of negative vorticity from the shear layer (i.e. at the top of the cavity) into the cavity near the downstream lip: see the top-right corner of the measurement domain in Figure 4.23 (1) through (3) for time offsets $\Delta tU_\infty/L$ = -2.20 ~ -1.46. Subsequently, this vorticity is intensified and grows inside the cavity, leading to the establishment of a recirculation flow in the downstream half of the cavity. As this happens, the vorticity progressively moves towards the cavity bottom, then upstream before it weakens again and disappears from the field of view. The strengthening and growth of the negative vorticity pulled into the cavity near the lower downstream corner of the cavity induces movement of high-speed fluid from above the cavity towards the corner. This can be seen best by focusing on the time offset at which the peak positive pressure on the downstream wall takes place, seen in Figure 4.24 (a). Particularly interesting is that the concentration of negative vorticity in this case is substantially lower and farther downstream than that leading to the peak positive pressure at $\Delta\phi$ = 0° (Figure 4.22 (a)). Thus, in the former case, the penetration of the high-speed fluid into the cavity is deeper, causing a stronger peak positive pressure. On the other hand, the peak negative pressure on the downstream wall

is seen to be associated with the movement of fluid away from the wall, as seen from the streamlines pattern in the vicinity of the pressure-measurement location in Figure 4.24 (b).

Finally, for completeness, the total vorticity field at $\Delta\phi$ = -32° can be seen in Figure 4.25. No strong vertical displacement of the shear-layer in/out of the cavity is seen here. Recall that such flapping motion was found to be associated with the formation of the wake mode at $\Delta\phi$ = 0°.

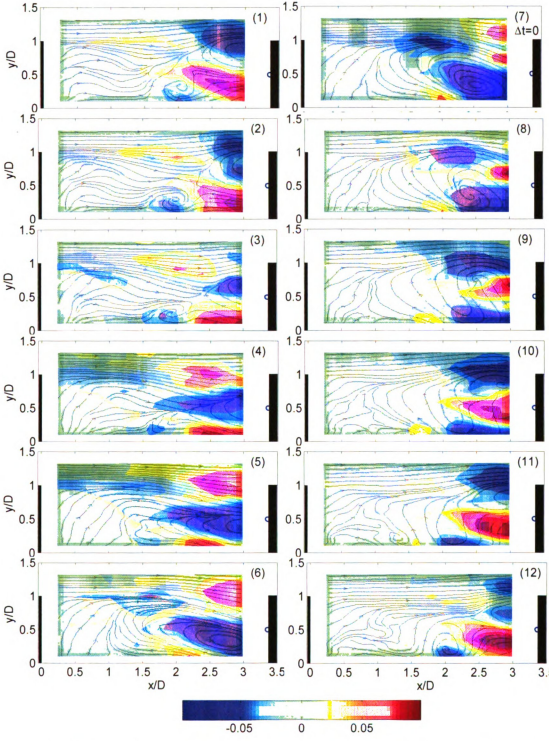

Figure 4.23 Streamlines and estimated fluctuating vorticity $\tilde{\omega}'_z D/U_\infty$ contours at $\Delta\phi = -32°$ for different time offsets (covering one period of the oscillation at $fL/U_\infty \approx 0.21$ with a time interval of $\Delta t U_\infty/L = 0.365$) preceding and following the occurrence of a positive pressure ($p' = p_{rms}$ at $\Delta t = 0$ in (7)) at $x/D = 3.3$ and $y/D = 0.5$. The color map on the bottom gives $\tilde{\omega}'_z D/U_\infty$ values

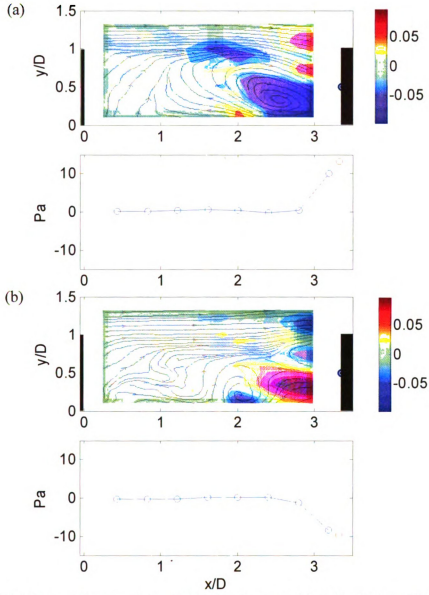

Figure 4.24 Streamlines, estimated fluctuating vorticity $\tilde{\omega}'_z D/U_\infty$ field and concurrent surface pressure in the *x*-*y* plane of $\Delta\phi$ = -32° corresponding to: (a) peak positive pressure and (b) peak negative pressure on the cavity end wall at *x*/*D* = 3.3 and *y*/*D* = 0.5 (pressure value shown with red circle). Blue line shows the pressure distribution on the cavity bottom, and color bar gives $\tilde{\omega}'_z D/U_\infty$ values

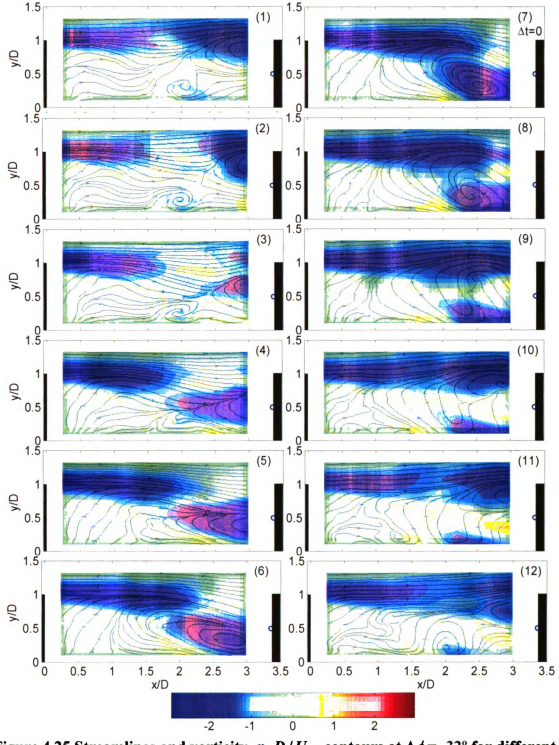

Figure 4.25 Streamlines and vorticity $\omega_z D/U_\infty$ contours at $\Delta\phi = -32^o$ for different time offsets (covering one period of the oscillation at $fL/U_\infty \approx 0.21$ with a time interval of $\Delta tU_\infty/L = 0.365$) preceding and following the occurrence of a positive pressure ($p' = p_{rms}$ at $\Delta t = 0$ in (7)) at $x/D = 3.3$ and $y/D = 0.5$. The color map on the bottom gives $\omega_z D/U_\infty$ values

Figure 4.26 displays the streamlines and estimated vorticity $\tilde{\omega}'_z D/U_\infty$ field in x-y plane at $\Delta\phi$ = -36° for different time offsets (over one period of the oscillation at $fL/U_\infty \approx 0.21$) relative to a positive pressure ($p' = p_{rms}$) at x/D = 3.3, y/D = 0.5 and $\Delta\phi$ = -32°. The observed flow structures combine the features of the structures found at $\Delta\phi$ = 0° and -32°. Similar to what happens in the central plane, vortex structures from the shear layer grow and propagate downstream in the x-y plane at $\Delta\phi$ = -36°. In addition, negative vorticity that is trapped near the downstream wall and pulled into the downstream half of the cavity (as at $\Delta\phi$ = -32°) is found. The downstream convecting vortex structures do not penetrate much into the cavity or grow to a size comparable to the cavity depth as in the central plane before they interact with the trapped vorticity from the downstream corner (see Figure 4.26 (6) to (8) at $\Delta tU_\infty/L$ = -0.37 to 0.37).

Figure 4.27 shows the evolution of the vorticity field in the x-y plane at $\Delta\phi$ = -36°. It suggests that there may be some lateral displacement of the shear layer into the cavity between $\Delta tU_\infty/L$ = -1.83 to -0.37 (seen Figure Figure 4.27 (2) to (6)). The displacement is not as pronounced as in the central plane.

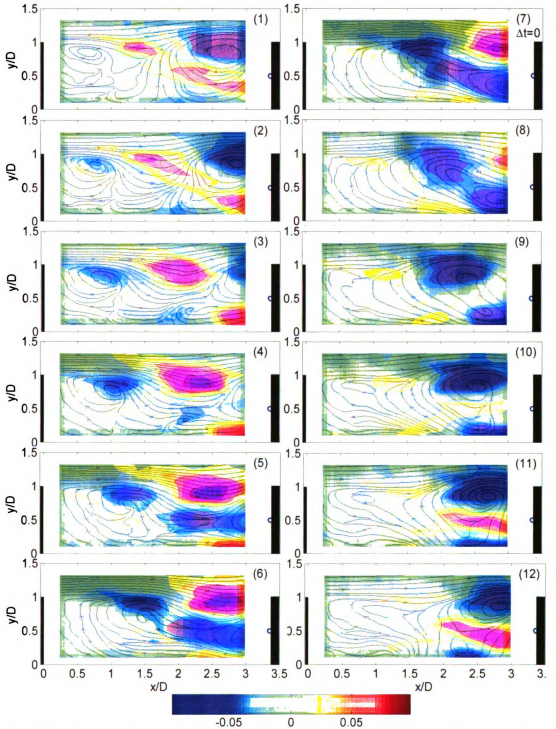

Figure 4.26 Streamlines and estimated fluctuating vorticity $\tilde{\omega}'_z D/U_\infty$ contours at $\Delta\phi = -36^o$ for different time offsets (covering one period of the oscillation at $fL/U_\infty \approx 0.21$ with a time interval of $\Delta t U_\infty/L = 0.365$) preceding and following the occurrence of a positive pressure ($p' = p_{rms}$ at $\Delta t = 0$ in (7)) at $x/D = 3.3$ and $y/D = 0.5$. The color map on the bottom gives $\tilde{\omega}'_z D/U_\infty$ values

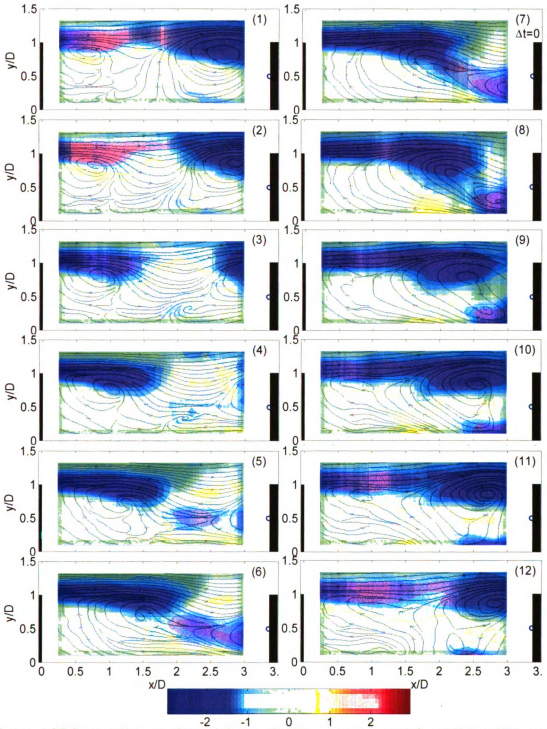

Figure 4.27 Streamlines and vorticity $\omega_z D/U_\infty$ contours at $\Delta\phi$ = -36° for different time offsets (covering one period of the oscillation at $fL/U_\infty \approx 0.21$ with a time interval of $\Delta tU_\infty/L = 0.365$) preceding and following the occurrence of a positive pressure ($p' = p_{rms}$ at $\Delta t = 0$ in (7)) at $x/D = 3.3$ and $y/D = 0.5$. The color map on the bottom gives $\omega_z D/U_\infty$ values

4.3 The Oscillation Mechanism: a Hypothesis

The results presented so far clearly show that strong, harmonic pressure oscillation are established close to the side wall (about one cavity depth away from the side wall) at the downstream end of the cavity. Although this oscillation is absent from the symmetry plane of the cavity (for sufficiently wide cavities), evidence leads to the hypothesis that the flow structures in the symmetry plane (which are similar to those found in the axi-symmetric cavity, where no strong harmonic oscillations are found at all) might be responsible (i.e. provide the driving mechanism) for the establishment of the oscillation near the side wall. This evidence consists of two components:

1. The frequency of the pressure oscillation caused by the harmonic oscillation is the same as that of the structure found in the symmetry plane and axi-symmetric cavities (see Figure 3.21 and 4.9).

2. At the frequency of the harmonic oscillation, coherence of about 20% is maintained between the pressure fluctuations in the symmetry plane and the harmonic oscillation near the side wall (see Figure 3.19). Although the coherence value is low, it is not zero and shows that correlated structure exists at the harmonic oscillation frequency in the symmetry and near-side-wall planes. The low coherence value should not undermine the significance of this correlation as this low value is likely the result of the weak pressure signature of the structure in the symmetry plane relative to the signature of the broadband turbulence.

The flow structure in the symmetry plane is found to be wake-like, consisting of vortex structures that form from the roll-up of the separating shear layer, and penetrate

into the cavity down to approximately half the cavity depth. Over the *x-y* domain inside the cavity into which these vortex structures penetrate, a cross-flow towards the symmetry plane is found near the side wall. This is believed to be the "communication mechanism" between the symmetry and oscillation planes. In particular, it is well known that the core of vortex structures corresponds to a low pressure zone. For example, Bradshaw and Koh[15] manipulated Poisson's equation, which governs the pressure field in incompressible flow, to show that negative pressures are generated wherever vorticity exists. Thus, it is hypothesized here that when the wake mode vortex structures penetrate into the cavity they create low-pressure regions in the central zone of the cavity. This leads to the establishment of a spanwise pressure gradient that drives the flow from near the side wall towards the symmetry plane.

The cross flow, which will occur at the same frequency as the shedding frequency of the central-plane vortex structures, is believed to cause two effects in the zone of strong pressure oscillation. First, it pumps fluid away from the side/end-wall zone, creating strong suction locally (corresponding to plot (1) in Figure 4.23). Second, to replace the fluid that is pumped from the side wall, vortical fluid is pulled from the shear layer into the cavity near the end wall (as seen from the LSE results in Figure 4.23 in plots (1) through (7)) towards the cavity downstream corner. The deep penetration of this vorticity and its subsequent intensification induces the flow of high-speed fluid from above the cavity towards the cavity downstream corner creating large positive pressure (plot (7) in Figure 4.23). Because of the "down pulling" of vorticity, the induced flow towards the cavity corner penetrates deeper than in the symmetry plane, causing larger pressure swings than found in the latter.

In summary, the above implies that the pressure fluctuations generated by the flow structure in the axi-symmetric cavity, which are not too strong and are comparable with those produced by background turbulence, can be intensified in the presence of cavity side walls. The intensification mechanism appears to be related to the establishment of complex, unsteady, three-dimensional flow resulting from the interaction of the flow structure near the cavity center with the flow near the side wall. The hypothesized mechanism linking the two flow zones requires further validation through SE, or whole-field measurements of the flow in y-ϕ planes that span half the cavity width and extend over the downstream half of the cavity. This is left for a future follow-up study.

4.4 References

[1] Grace, S.M., Dewar, G.W. and Wroblewski, D.E., "Experimental Investigation of the Flow Characteristics within a Shallow Wall Cavity for both Laminar and Turbulent Upstream Boundary Layers," *Experiments in Fluids,* **36**, 2004, pp. 791-804.

[2] Ozsoy, E., Rambaud, P. and Riethmuller, M.L., "Vortex Characteristics in Laminar Cavity Flow at Very Low Mach Number," *Experiments in Fluid*, **38**, 2005, pp. 133-145.

[3] Ukeiley, L. and Murray, N., "Velocity and Surface Pressure Measurements in an Open Cavity," *Experiments in Fluids*, **38**, 2005, pp. 656-671.

[4] Ashcroft, G. and Zhang, X., "Vortical Structures over Rectangular Cavities at Low Speed," *Physics of Fluids*, **17** (015104), 2005, pp. 1-8.

[5] Chiang, T.P., Hwang, R.R. and Sheu, W.H., "Finite Volume Analysis of Spiral Motion in a Rectangular Lid-Driven Cavity," *International Journal for Numerical Methods in Fluids*, **23**, 1996, pp. 325-346.

[6] Adrian, R.J., "On the Role of Conditional Averages in Turbulence Theory," *Proceedings of the Fourth Biennial Symposium on Turbulence in Liquids*, Rolla, Mo., September, 1975. (A77-40426 18-34) Princeton, N.J., Science Presss, 1977, pp. 323-332.

[7] Adrian, R.J., "Conditional Eddys in Isotropic Turbulence," *Physics of Fluids*, **22**, 1979, pp. 2065-2070.

[8] Guezennec, Y.G., "Stochastic Estimationof Coherent Structures in Turbulent Boundary Layer," *Physics of Fluids A*, **1**, 1989, pp. 1054-1060.

[9] Naguib, A.M., Wark, C.E., and Juchenhofel, O., "Stochastic Estimation and Flow Sources Associated with Surface Pressure Events in a Turbulent Boundary Layer," *Physics of Fluids*, **13**(9), 2001, pp. 22611-2626.

[10] Murray, N. and Ukeiley, L., "Estimationof the flowfield from surface pressure measurements in an open cavity," *AIAA Journal,* **41** (5), pp. 969-972 (2003)

[11] Hudy, L.M., "Simultaneous Wall-Pressure and Velocity Measurements in the Flow Field Downstream of an Axisymmetric Backward-Facing Step," Ph.D. thesis, pp 13 -16 (2005)

[12] Durgesh, V., "Experimental Study of Near Wake Dynamics Associated with Bluff Body Based Drag Reduction," Ph.D. thesis, (2008)

[13] Najm, H.N. and Ghoniem, A.F., "Numerical simulation of the convective instability in a dump combustor," *AIAA Journal,* **29** (6), pp. 911 - 919 (1991)

[14] Rowley, C.W., Colonius, T. and Basu, A.J., "On Self-sustained Oscillations in Two-dimensional Compressible Flow over Rectanguler Cavities", *Journal of Fluid Mechanics* **455**, pp. 315 - 346 (2002)

[15] Bradshaw, P. and Kog, Y.M., "A note on Poisson's Equation for Pressure in a Turbulent Flow," *Physics of Fluids*, **24** (4), pp. 777, (1981)

5. CONCLUSIONS AND RECOMMENDATIONS

Examined in the current study is the effect of cavity width and side walls on the self-sustained oscillations in a low-Mach-number cavity flow with a turbulent boundary layer at separation. An axisymmetric cavity geometry which is free from any side-wall influence but could be partially filled to form finite-width cavities is employed. Unsteady surface pressure is measured on the cavity bottom along the streamwise direction and on the downstream wall along the azimuthal direction to explore the three-dimensional features of cavity oscillation. Two-component velocity is measured using an LDA system, simultaneously with the surface pressure in x-y (i.e. streamwise-wall normal) planes at different azimuthal locations to understand the mechanism driving the oscillation.

Unlike the axisymmetric geometry, strong harmonic pressure oscillations are detected in cavities having side walls. The oscillations are generally located at a distance of approximately one cavity depth away from the side walls. However, when the cavity becomes sufficiently narrow, the two locations where the oscillation is found (near each of the two side walls) "merge" in the symmetry plane. This is the case for the narrowest cavity examined (W/D = 2.5). No prominent oscillation is observed in the symmetry plane in the widest finite-width cavity investigated (W/D = 7.4). In this case the flow structure in the symmetry plane is found to share the same features as in the axisymmetric cavity. The distinction between "narrow" and "wide" cavities (i.e. corresponding to whether strong harmonic oscillations are observed in the symmetry plane or not) is found to take place at a cavity width that scales with the cavity length: $W/L \approx 1$

Mean-velocity results for the wide cavity show that there is a net mean flow from the region near the side walls towards the center of the cavity in the approximate range $1.8 < x/D < 2.5$. Stochastic estimation of the velocity field suggests that the flow structure in the symmetry plane is wake-like. Vortex structures form as a result of the roll-up of the separating shear layer, and penetrate into the cavity down to approximately half the cavity depth. Interestingly, the mean cross-flow from the side-wall region towards the symmetry plane is found to occur over the same x-y domain inside the cavity into which the vortex structures penetrate. It is *hypothesized* that when the vortex structures penetrate into the cavity they create low-pressure regions in the central zone of the cavity. This leads to the establishment of a spanwise pressure gradient that drives the flow from near the side wall towards the symmetry plane. This cross flow is ultimately linked to the intensification of pressure oscillation near the side walls. In other words, although the flow structure in the axisymmetic cavity (and symmetry plane of wide finite-width cavities) does not have a prominent pressure signature, it can interact with the side walls in finite-width cavities, leading to the establishment of strong harmonic pressure oscillation near the side wall.

The hypothesized oscillation mechanism is based on a complex, unsteady, three-dimensional flow field that results from the interaction of the structures near the cavity center with the flow near the side walls. Rigorous validation of this mechanism linking the two flow zones is recommended for a future follow-up study. This could be done through whole-field measurements of the flow in y-ϕ planes that span half the cavity width and extend over the downstream half of the cavity. To "enhance the visibility" of the oscillation mechanism (relative to background broadband turbulence), these

measurements could be done while forcing the wake mode near the middle of the cavity. This will cause the wake mode to be strong and more organized than under natural conditions, and hence all measurements can be phase-locked to the forcing signal and data sampled in all azimuthal planes can be correlated across the cavity.

Another way to check the proposed mechanism is to change the boundary-layer condition at separation so that a shear-layer (with or without Rossiter oscillation) rather than a wake mode exist in the axisymmetric cavity (and hence, also in the symmetry plane of wide finite-width cavity). Since the vortex structures remain above the cavity opening in this case, no cross-flow should be established at the passage frequency of the vortex structures of the shear layer (based on the above hypothesis). Consequently, the intensification of oscillations near the side wall would not happen in cavities with shear-layer mode.

Finally, this work addresses the mechanism driving the harmonic wall-pressure oscillation at $fL/U_\infty \approx 0.21$ near the side wall in cavities with finite width (because this oscillation occurs at the same frequency as that of the weak peak found in the axisymmetric cavity). Understanding of the nature of disturbances found at the low-frequency end near the side walls is left for future studies.

6. APPENDEX

6.1 Wiring for Azimuthal Microphone Array

Figure 6.1 shows a picture of the wiring for the Knowles azimuthal microphone array. Each microphone has three 25.4 mm-long leads for power, ground and output signals. Leads carrying power and ground signals were soldered to copper tape (forming power and ground bus respectively) on the back side of the Detachable Sensor Ring (see Figure 2.3). 32-AWG wires connected the power bus (red wire) and ground bus (black wire) to the power and read-out circuits. 1.5 volts voltage is required to operate the microphones. Yellow leads connected with 32-AWG wires carry the output signal. 32-AWG wires are directed out of the model through the gap between the cylindrical shell and the model's surface.

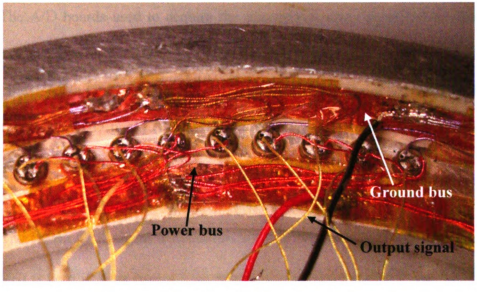

Figure 6.1 Wiring for Knowles azimuthal microphone array

Figure 6.2 shows a picture of the wiring for the Panisonic azimuthal microphone array. Red wire connected to the out put terminal and black wire connected to the ground

terminal of each microphone are directed out of the model through the gap between the cylindrical shell and the model's surface.

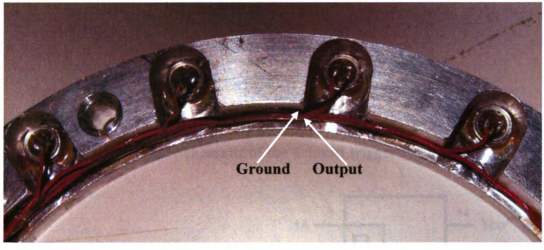

Figure 6.2 Wiring for Panasonic azimuthal microphone array

6.2 Schmitt Trigger Circuit

The A/D boards used to acquire the microphone-array signals share the same 1 MHz clock signal with the LDA system. A Schmitt trigger (CD74HCT132E) is used to regulate the 1 MHz CLK signal from the BSA to a TTL compatible signal before it is sent to the master A/D board (AT-MIO-16E-10). Figure 6.3 shows a schematic of the Schmitt trigger circuit. The pin-out and function diagram of the Schmitt trigger IC are displayed in Figure 6.4. 5 V DC power supply is required to drive the Schmitt trigger circuit. The 1MHz CLK signal is fed to the Schmitt trigger as the input (V_I). The output signal (V_O) is zero if V_I is over a high-voltage threshold around 2 V and V_O switch to V_{CC} if V_I is below a low voltage threshold around 1 V. Thus the output signal of the Schmitt trigger circuit used as the clock signal of the A/D boards is a square wave having the same frequency as the clock signal of the LDA system.

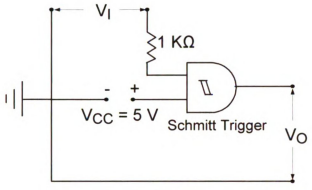

Figure 6.3 Schematic of the Schmitt trigger circuit

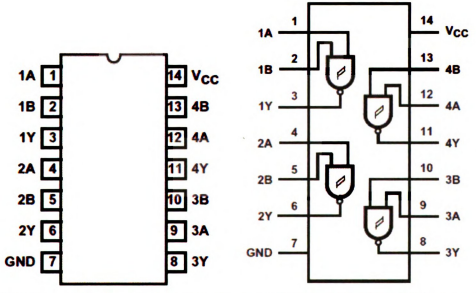

Figure 6.4 Pin-out (left) and function diagram (right) of the Schmitt trigger (model CD74HCT132E)

6.3 LDA system alignment

The following is a description of the procedure used to align the LDA system. First, align the transmitter with the argon-ion laser by adjusting the support-feet thumb screws on the side of the transmitter until the energy of the beams coming out of each manipulator is maximized. For this step, the optical fibers leading to the probe head should be disconnected from the manipulator and the beam shutter should be open. This

will cause the beams coming out of the manipulator to be directed vertically up into the open air. The strength of the beams can be gauged visually from their projection on the ceiling of the lab. The transmitter should be aligned to attain two conditions: (1) the overall beam intensity is maximized; (2) the intensity of the shifted and un-shifted beams for a given wavelength is balanced.

Second, connect the optical fibers of the probe head to the manipulators. Direct the beams coming out from the probe at a photo detector that accommodates light intensity of 100 mW or higher (or run the laser at low power during alignment). For each of the four beams (two green and two blue), close the shutter on the other three beams and turn the adjustment thumb screws on the manipulator (two for focusing, one for displacement and one for angle of the fiber optic end) to maximize the power of the beam (i.e. the output of the photo detector). After the above adjustment, the power of the two beams with the same color coming out of the probe should be equal. If for a beam pair of a given wavelength, the un-shifted beam is stronger than the shifted beam, or vice versa, the equality of beam intensity can be achieved by weakening the stronger beam.

Third, to precisely place the beams intersection point at the receiving lens focal point, mount the end of receiver fiber in the output aperture of the spare color (violet here) in the manipulator. Close the shutters of the manipulator for the green and blue beams and open the one for the violet beam. This will cause the violet beam to emerge from the center of the probe head and is directed towards the measurement plane. Place a microscope objective in the focal point of the violet beam. To identify this point, adjust the position of the objective until the projection of the violet beam on a screen placed on the opposite side of the objective is minimum. Open the shutter of the manipulator for

each of the green and blue beams; one at a time. Adjust the 'BEAM ADJ' screws on the side of the probe head to move the projection (from the microscope objective) of each beam to coincide with that of the violet beam. This guarantees the intersection of the beams to coincide with the focus of the receiver fiber. The beam spacing (lateral distance between beam pair of a given wavelength) can be varied by adjusting the 'BEAM SEP' screw on the side of the probe. Finally, close the beam shutter in the violet beam manipulator. Disconnect the end of the receiving fiber from the manipulator and connect it to the appropriate adaptor attached to the photomultiplier tubes.

6.4 Azimuthal Traversing of the LDA Probe Volume

Wall pressure measurements are performed to ensure that the characteristics of the pressure fluctuations in a given azimuthal plane depend *only* on the offset angle relative to the cavity symmetry plane ($\Delta\phi$) *regardless* of the azimuthal location of the symmetry plane relative to the top of the model (ϕ_c): see Figure 2.19 for definition of $\Delta\phi$ and ϕ_c.

Figure 6.5 displays frequency spectra of the unsteady wall pressure acting on the cavity's downstream wall at y/D = 0.5 in the symmetry plane ($\Delta\phi$ = 0°) of the cavity with L/D = 3.3 and W/D = 7.4, at Re = 12200. Lines with different colors represent different azimuthal locations of the symmetry plane, ϕ_c, obtained by rotating the cavity relative to the top plane of the model. The legend shows the azimuthal angle of the symmetry plane, ϕ_c, relative to the top plane of the model. Note that positive angle values correspond to the symmetry plane being on the right of the top plane of the model when viewing the model from the upstream direction. Also, the magnitude of the spectra is normalized by

the energy of the fluctuations, i.e. the square of the rms pressure, to compare the spectrum shape for the different cases.

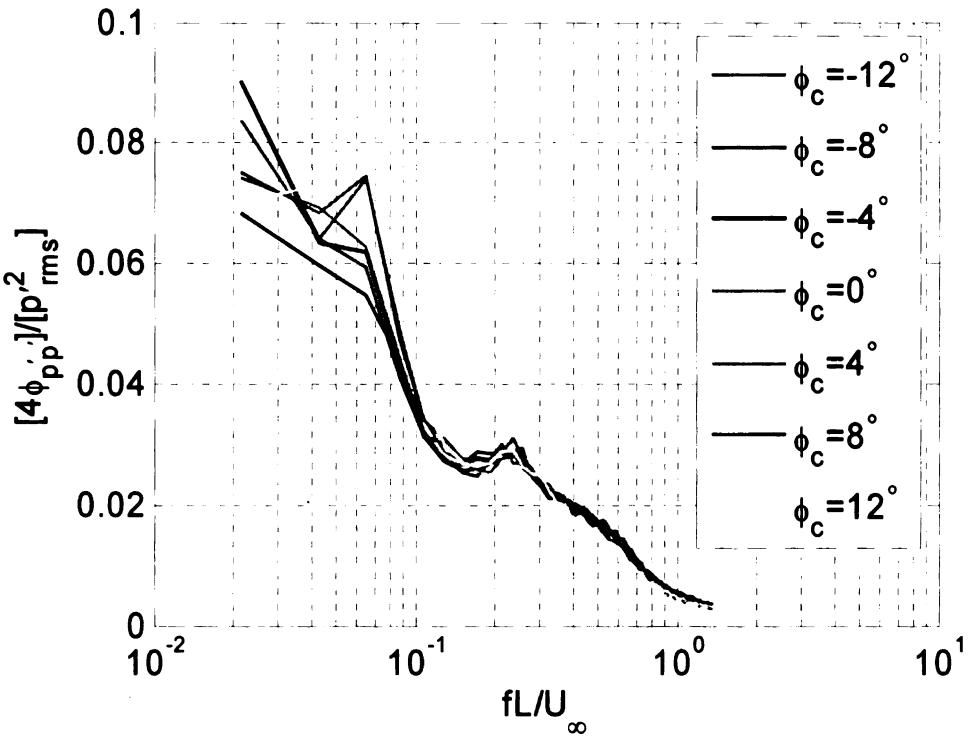

Figure 6.5 Frequency spectrum of the pressure acting on the cavity's downstream wall in the symmetry plane (at $\Delta\phi = 0°$) for $L/D = 3.3$, $W/D = 7.4$ and $Re = 12200$. Different colors correspond to different azimuthal locations of the symmetry plane

Figure 6.5 shows that the spectra for different cases collapse except those fluctuations at very low frequency. The spectral characteristics of the pressure fluctuations (particularly within the frequency band of interest, which surrounds the frequency $fL/U_\infty \approx 0.21$) remain the same for different azimuthal locations of the cavity. Results similar to those in Figure 6.5 but in the azimuthal plane where the strength of the harmonic oscillation reaches a peak value (z/D = -2.62 or $\Delta\phi$ = -32°) are displayed in Figure 6.6 for the cavity with W/D = 7.4. Lines with different colors represent the different azimuthal angles by which the cavity is rotated. The plot shows that prominent

harmonic oscillation is established within the azimuthal plane corresponding to $\Delta\phi$ = -32° regardless of the azimuthal location of the symmetry plane relative to the top of the model (ϕ_c). The above results confirm that the wall-pressure characteristics and its generating flow structure remain unaltered when the cavity is rotated to different azimuthal locations around the axisymmetric model.

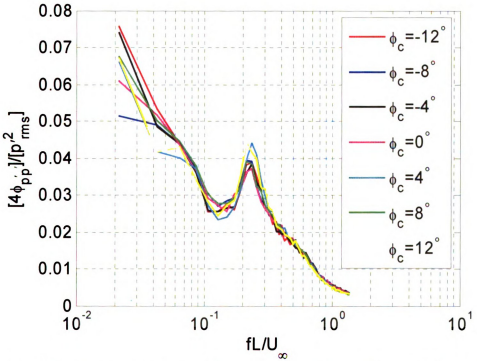

Figure 6.6 Frequency spectrum of the pressure acting on the cavity's downstream wall at $\Delta\phi$ = -32° for L/D = 3.3, W/D = 7.4 and Re = 12200. Different colors correspond to different azimuthal locations of the symmetry plane